

**Quantum measurement and real-time feedback
of a spin register in diamond
CONCEPT**

Quantum measurement and real-time feedback of a spin register in diamond CONCEPT

Proefschrift

ter verkrijging van de graad van doctor
aan de Technische Universiteit Delft,
op gezag van de Rector Magnificus Prof. ir. K.C.A.M. Luyben,
voorzitter van het College voor Promoties,
in het openbaar te verdedigen op om uur

door

Machiel BLOK

MSc
geboren te Amsterdam, Netherlands

Dit proefschrift is goedgekeurd door de promotor:

Prof. dr. ir. R. Hanson

Samenstelling promotiecommissie:

Rector Magnificus, voorzitter
Prof. dr. ir. R. Hanson, Technische Universiteit Delft, promotor



Copyright © 2015 by Machiel Blok

All rights reserved. No part of this book may be reproduced, stored in a retrieval system, or transmitted, in any form or by any means, without prior permission from the copyright owner.

ISBN

Casimir PhD Series Delft-Leiden 2013-36

Cover design: L.D. Swakman

Printed by Gildeprint Drukkerijen – www.gildeprint.nl

An electronic version of this thesis is available at www.library.tudelft.nl/dissertations

Contents

1	Introduction	1
1.1	Bibliography	2
2	Experimental control and theory of the NV center	3
2.1	The NV center in diamond	4
2.2	Single NV center device	6
2.3	Addressing the electron excited state	7
2.4	Ground state spin control	9
2.5	Electron spin coherence times	10
2.6	Coupling to individual nuclear spins	12
2.6.1	Host nitrogen spin	12
2.6.2	^{13}C spins	13
2.7	Bibliography	15
3	Manipulating a qubit through the backaction of adaptive measurements	17
3.1	Introduction	18
3.2	Variable-strength measurement	18
3.3	Generalized weak value	20
3.4	QND-measurement of the ancilla qubit	20
3.5	Control by adaptive measurements	23
3.6	Methods	27
3.6.1	Levels and Hamiltonian	27
3.6.2	Qubit initialization	29
3.6.3	Nucleus-independent electron spin rotations	30
3.6.4	Electron-independent nuclear spin rotation	30
3.6.5	Partial measurements with controlled strength: Theory	31
3.6.6	Characterization of the partial measurements	33
3.6.7	Weak value and conditioned average	35
3.6.8	Experimental quantum weak value for a spin qubit	37
3.6.9	Partial measurements as probabilistic rotations	38
3.6.10	Heralded sequential measurements: un-collapse and steering	38

3.7	State steering by real-time adaptive measurements	40
3.7.1	Ideal protocol	40
3.7.2	Error analysis	41
3.8	Bibliography	43
4	Optimized quantum sensing using real-time adaptive measurements	47
4.1	Introduction	48
4.2	D.C. Magnetometry	48
4.3	Adaptive frequency estimation protocol	51
4.4	Comparison between adaptive and non-adaptive protocols	54
4.5	Methods	56
4.5.1	Sample and experimental setup	56
4.5.2	Adaptive algorithm	57
4.6	Bibliography	58
5	Heralded entanglement and unconditional teleportation between remote qubits	61
5.1	Introduction	62
5.2	Heralded entanglement	62
5.2.1	Implementation	65
5.2.2	Demonstration of remote entanglement	67
5.3	Teleportation	69
5.4	Methods	75
5.5	Bibliography	76
6	Analysis of a quantum memory with optical interface in diamond	79
6.1	Introduction	80
6.2	Control and Characterization of nuclear spins in diamond	80
6.3	Modeling the dephasing of a carbon spin during entanglement generation	84
6.4	Methods	87
6.5	Bibliography	89
7	Storing a quantum state during optical excitation of a quantum network node	91
7.1	Introduction	92
7.2	Bibliography	94

CHAPTER 1

INTRODUCTION

M.S. Blok

1.1 Bibliography

CHAPTER 2

EXPERIMENTAL CONTROL AND THEORY OF THE NV CENTER

M.S. Blok

The Nitrogen-Vacancy (NV) center in diamond has recently emerged as an excellent system to demonstrate quantum control of single spins. In this chapter we discuss its physical properties and the experimental techniques that form the basis of the results presented in chapters 3-6. We first introduce the basic electronic structure and the detection of single NV centers in a confocal microscope setup (section 2.1). In section 2.2 we discuss the devices that enable optical initialization and single shot readout of the electron spin at low temperature (section 2.3). The coherent control and characterization of the coherence times of the electron spin are presented in section 2.4. Finally we show how the coupling of the central spin to nearby nuclear spins allows us to extend our quantum register to multiple qubits.

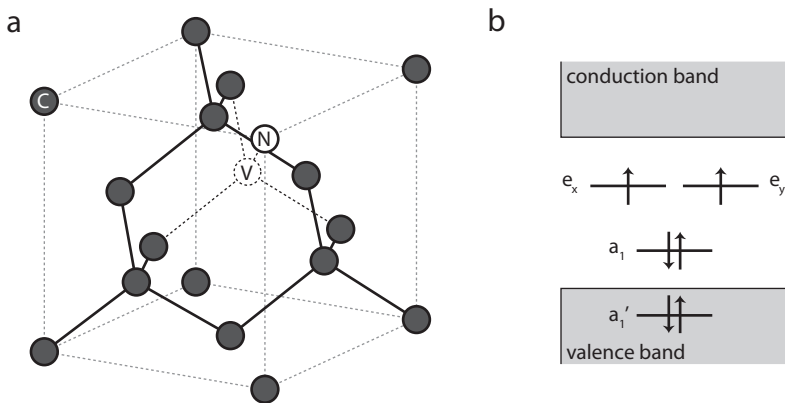


Figure 2.1 | Crystal and electronic structure of the NV center Figure from^{1(a)} The Nitrogen-Vacancy center defect is formed by a substitutional nitrogen atom (N) and a missing atom (vacancy, V) at an adjacent position in the diamond lattice (b) The electron occupation of the molecular orbitals in the electronic ground state, following Pauli's exclusion principle. The molecular orbitals are a linear combination of hybridised sp^3 -orbitals. They are found by using the C_{3v} -symmetry of the NV center, taking into account the Coulomb interaction of the diamond nuclei and the lattice electrons with the electrons in the orbitals.

2.1 The NV center in diamond

The nitrogen vacancy center is a defect in the diamond lattice consisting of a substitutional nitrogen atom and a vacancy at an adjacent lattice position (Fig. 2.1). In its neutral charge state (NV^0) it hosts 5 electrons: 2 donor electrons from the nitrogen and 3 from the dangling bonds of the adjacent carbon atoms. Its negative charge state NV^- is formed by capturing an electron from the environment. The experiments in this thesis are all performed on NV^- , which can be prepared experimentally as discussed in section 2.3.

In the electronic ground state, the 6 electrons occupy the molecular orbitals as shown in Fig. 2.1b. Excluding electron-electron interactions, the electronic ground-, ($^2a^2e$) and excited ($^1a^3e$) state are spin degenerate. This degeneracy is lifted by the Coulomb interaction between the electrons which leads to spin triplet ($S = 1$) ground-, and excited states (3A_2 and 3E respectively) as well as multiple intermediate spin singlet levels. The 3A_2 to 3E transition energy of 1.945 eV lies in the optical regime (637 nm), well within the bandgap of diamond (5.5eV). Since all experimental techniques in this thesis aim to control the NV center in the spin triplet manifold, we will not discuss the singlet levels in further detail. For a more detailed discussion of the electronic structure of the NV-center we refer to a recent review of Doherty *et al*².

We identify NV centers in bulk diamond at room-temperature in a home-build confocal

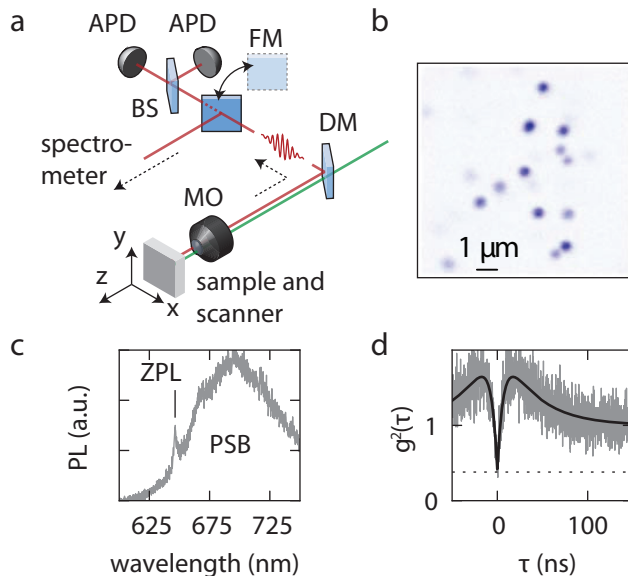


Figure 2.2 | Detection of single NV centers Figure from ¹(a) Confocal microscope setup. The NV centers are excited by focussing a green (532 nm) excitation laser onto the sample using a microscope objective (MO). The sample is mounted on a piezo-stage allowing three-dimensional scans. The emission is spectrally filtered using a dicroic mirror (DM) and via a mechanically switchable mirror (FM) sent either to a spectrometer or to a beamsplitter (BS) followed by two APDs in a HBT-configuration. (b) Confocal scan of a bulk diamond sample. The intensity is plotted as a function of the stage position in x and y . Blue is higher intensity. (c) Emission spectrum of a single NV center with the zero phonon line at 637 nm and the phonon sideband at higher wavelengths. (d) Second-order autocorrelation function, with τ the delay between detection events of different detectors. The solid-line is a fit using a three-level model, including dark counts. The slow decay is associated with the decay from the singlet levels.

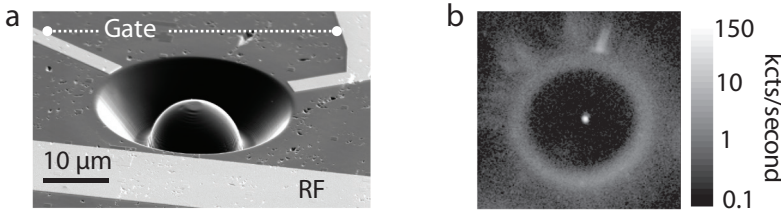


Figure 2.3 | Figure from¹ (a)

microscope setup (Fig. 2.2a). By scanning the sample and collecting the fluorescence signal with a single photodiode (APD) we find multiple diffraction limited spots, corresponding to NV centers (Fig. 2.2b). Here we off-resonantly excite the NV center to a phonon level above the 3E level, which quickly decays non-radiatively to 3E . The reflections of the excitation are separated from the fluorescence with a dicroic mirror. The emission spectrum from 3E is shown in Fig. 2.2c. It shows a distinct peak around 637 nm, corresponding to the direct decay from 3E to 3A_2 (zero phonon line, ZPL) and a broad sideband corresponding to the decay to a phonon level above 3A_2 (phonon side band, PSB). To verify that the signal originates from a single emitter, we measure the second-order autocorrelation function $g^2(\tau)$ in a Hanbury-Brown-Twiss configuration (Fig. 2.2d). The low probability of simultaneous photon detection ($g^2(\tau = 0) < 1/2$) confirms that the signal comes from a single emitter.

2.2 Single NV center device

To enhance the collection and excitation efficiency of the NV center, a solid-immersion lens (SIL) is milled in the diamond using a focused ion beam (FIB)^{1,3-5} (Fig. 2.3a). For an NV center in the middle of the SIL, the hemisphere ensures that the emission from the NV center reaches the diamond-air surface at normal incidence. This significantly reduces the loss due to total-internal reflection. For precise placement of the SIL, a pre-characterized NV center is located with respect to $1 \times 1 \mu\text{m}$ gold markers that are fabricated on the surface of the diamond using electron beam lithography. The hemisphere structure is then created using a gallium ion beam by milling concentric rings of varying diameter around the position of the NV center. After milling the SILs, the sample is cleaned for 30 minutes in a boiling mixture of equal parts of perchloric, sulfuric and nitric acid. This step removes the redeposited material during milling. A small conductive layer of gallium atoms that is implanted during the FIB process is removed by reactive-ion etching in an oxygen-plasma.

A 200 nm thick gold microwave strip line for spin manipulation (Fig 2.8 and 2.10) and DC gates to DC stark shift the ZPL (see chapter 5) are fabricated near the SIL using electron beam lithography. Finally a single-layer anti-reflection coating⁶ (aluminium oxide) is fabricated on top of the sample to further increase the collection efficiency and reduce the reflection during resonant excitation (see chapter 5).

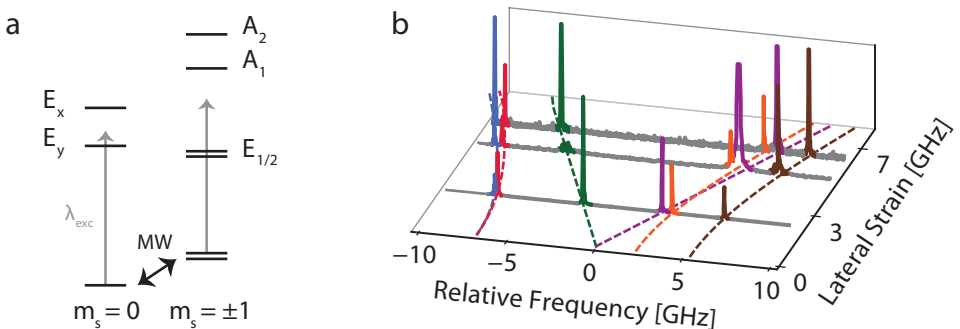


Figure 2.4 | Spectrum of the excited state (a) Energy level diagram of the fine structure of the excited state. There are two levels with spin $m_s = 0$ (E_x, E_y) and four $m_s = \pm 1$ levels (A_1, A_2, E_1 and E_2). At finite strain the degeneracies between E_x, E_y and E_1, E_2 are lifted. (b) The energy spectrum for three different NV centers is measured by varying the frequency of the excitation laser and detecting the fluorescence in the PSB. The observed transitions E_1 (blue), E_2 (red), E_y (green), E_x (purple), A_1 (orange) and A_2 (brown) are color coded and agree well with the theoretical prediction (colored dashed lines). For each scan the transition energies ΔE_x and ΔE_y are determined to calculate the lateral ($\frac{\Delta E_x - \Delta E_y}{2}$) and parallel ($\frac{\Delta E_y + \Delta E_x}{2}$) strain. The parallel strain is then subtracted for each scan. Laser frequency is with respect to 470.4 THz.

2.3 Addressing the electron excited state

The spin-orbit and spin-spin interactions introduce a fine splitting to the 3E excited state which can be observed at cryogenic temperatures. The six resulting transitions have a distinct spin character (Fig. 2.4a) and allow for spin-selective optical excitation of the electron. The transitions to the $m_s = 0$ states (E_x and E_y) can occur upon absorptio or emission of a linearly polarized photon, while the four $m_s = \pm 1$ transitions couple to circularly polarized light. The transition frequencies shift when an electric field or strain is applied. For an electric field along the N-V axis this results in an offset to the spectrum, not changing the energy level spacing. A perpendicular electric field affects the difference between the energy levels. As a result, the spectrum of the excited state slightly varies between NV centers due to local differences in strain and electric field. In Fig. 2.4b we show measurements of the spectra of three different NV centres, normalized to have the same parallel strain. The lateral strain is determined from the difference between the transition energies of E_x and E_y . The spectra show excellent agreement with the theoretical prediction (dashed lines). The strain typically differs a few tens of GHz between NV centers measured in this thesis.

To address the spin-selective optical transitions in an experiment, we first verify that the NV center is in the NV^- state and that the lasers are resonant with the desired transitions before each experimental run. During this charge-resonance (CR) check, we simultaneously

2. Experimental control and theory of the NV center

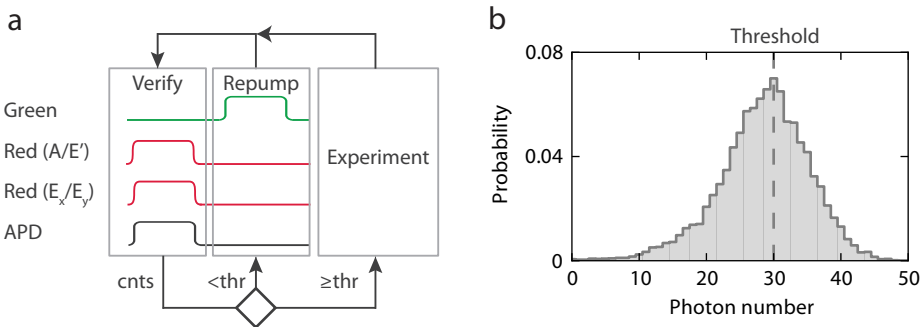


Figure 2.5 | Verifying the charge state and laser resonances (a) Schematic of the experimental sequence to verify the charge state of the NV center and the laser resonances. The process is controlled by an ADwin microprocessor which turns on the two red lasers and compares the number of photons detected by the avalanche photodiode (APD) to a predetermined threshold (verify stage). When the number of detected photons is below the threshold a green laser is applied to prepare the NV^- state (repump stage), otherwise the experimental sequence is initiated. (b) Photon number distribution during the verification stage, conditioned on the previous CR check being successful.

apply two red lasers and monitor the fluorescence (Fig. 2.5a). The lasers can only excite the electron spin for the NV center in NV^- and the number of detected photons is highest when one red lasers is resonant with a $m_s = 0$ transition and the other with a $m_s = \pm 1$ transition. We therefore compare the signal to a threshold and only continue with the experimental sequence when the threshold is passed (Fig. 2.5b). When the number of detected photons is below the threshold we apply a green (523 nm) laser, perform another CR check and repeat until success. The green laser can repump the center to NV^- by exciting trapped charges in the environment, but also induces spectral diffusion of the optical transitions since the local electric field is affected by the charge configuration in the environment. As an alternative to the green laser, a yellow laser ($\lambda \approx 575$ nm) can be used to resonantly excite the NV^0 zero phonon line⁷.

The electron spin is initialized by selectively exciting a single transition⁸: E_x or E_y to prepare $m_s = \pm 1$ or $A_1/A_2/E'$ to prepare $m_s = 0$. The slight spin mixing of the excited states provides an optical pumping mechanism to prepare the opposite spin state (2.6)a). The fluorescence observed during initialization (2.6)b) exponentially decreases with the probability that the spin has flipped to a dark state that can not be excited by the pumping laser. The signal is fitted to an exponential decay to extract a lower bound for the preparation fidelity. To ensure that a pure state is prepared (as opposed to a mixture of $m_s = \pm 1$) the electron spin is typically initialized in $m_s = 0$, for this state we find a lower bound of $(99.7 \pm 0.1)\%$.

The observed fluorescence upon selective excitation provides a means to detect the electron

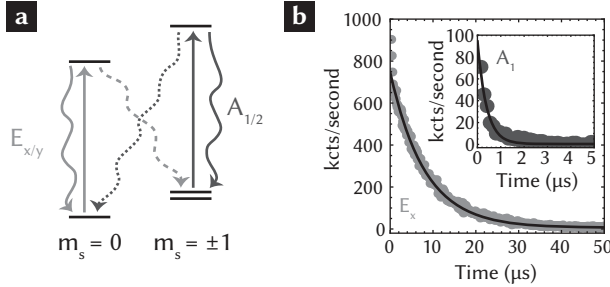


Figure 2.6 | Figure from ¹ Initialization by spin pumping (a) Energy levels used to initialize (and readout) the electron spin. We excite transitions with a well-defined spin character of either $m_s = 0$ (bright arrows) or $m_s = \pm 1$ (dark arrows), resulting in spin-conserving optical cycling (indicated by bended solid arrows). Dashed arrows indicate the spin non-conserving decay paths. (b) Observed fluorescence when exciting E_x (A_1) with the spin initially prepared in $m_s = \pm 1$ ($m_s = 0$). The signal is fitted to a single exponential with an offset to account for dark counts. From the fit we find a lower limit for the initialization fidelities: $(99.7 \pm 0.1)\%$ for $m_s = 0$ and $(99.2 \pm 0.1)\%$ for $m_s = \pm 1$.

spin state in a single shot⁸. To characterize the readout we plot the distribution of photons detected in the PSB collected during a $10\ \mu s$ laser pulse exciting E_x (fig 2.7a). The distributions are clearly separated depending on the initial spin state, allowing us to assign $m_s = 0$ to the cases where one or more photons are detected and $m_s = \pm 1$ otherwise. The combined readout and initialization fidelity for $m_s = \pm 1$ ($F_1 = .989 \pm .001$) is reduced by detector dark counts and off-resonant excitation, while for $m_s = 0$ ($F_1 = .956 \pm .003$) the error is governed by the instances where the spin is flipped before a photon is detected. This can be seen in fig 2.7b where the readout fidelities are plotted as a function of readout duration. The fidelity for $m_s = 0$ initially increases with readout time and then saturates indicating that the spin has flipped with high probability. The optimal mean readout fidelity ($F_{ro} = \frac{F_0+F_1}{2} = 0.973 \pm 0.002$) is reached after $10\mu s$.

2.4 Ground state spin control

In the orbital ground state, the $m_s = 0$ and $m_s = \pm 1$ states are separated by the zero-field splitting $D \approx 2.88$ GHz, while an external magnetic field lifts the degeneracy between $m_s = +1$ and -1 via the zeeman splitting. The Hamiltonian is given by

$$H_{GS,e} = DS_z^2 + \gamma_e \mathbf{B} \cdot \mathbf{S} \quad (2.1)$$

with $\mathbf{S} = [S_x, S_y, S_z]$, S_i the spin matrices for a spin-1 system and $\gamma_e = 2.8$ MHz/G the gyromagnetic ratio of the electron. We define our qubit in the $m_s = 0 : |0\rangle$ and

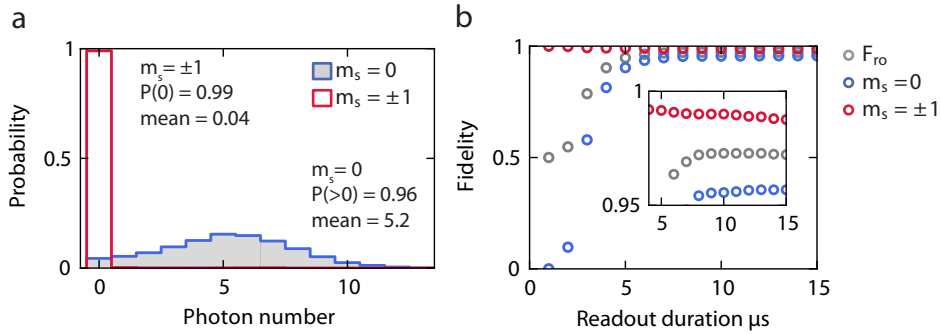


Figure 2.7 | Single shot readout (a) Histograms of the number of detected photons in the PSB for initial state $m_s = 0$ (blue) and $m_s = \pm 1$ (red) during a $10 \mu\text{s}$ readout on E_x . (b) Fidelities for reading out the electron spin state initially prepared in $m_s = 0$ (blue) and $m_s = \pm 1$ (red) as a function of readout duration. The mean readout fidelity is plotted in grey. The inset is a zoom of the region where the optimal mean readout fidelity is reached.

$m_s = -1 : |1\rangle$ states (alternatively the $m_s = +1$ state can be used to encode $|1\rangle$). The electron spin is manipulated with electron spin resonance techniques by sending an ac current through the stripline generating an oscillating magnetic field at the location of the NV center. At the resonance condition the frequency of the control field matches the energy difference between the $|0\rangle$ and $|1\rangle$ states resulting in coherent Rabi oscillations between those levels as shown in fig 2.8. Arbitrary qubit rotations are implemented by calibrating the amplitude (which sets the rabi frequency) and length of the microwave (MW) control pulses.

2.5 Electron spin coherence times

The NV center has a long-lived electron spin state. At low temperature T_1 -relaxation times (typical time of an eigenstate to be perturbed) were measured to be xxx s in ensembles. The phase coherence times depend strongly on the microscopic environment of the NV center. When the defect is located in bulk diamond (far away from any surface) the dominant dephasing mechanism is the spin-bath of the diamond lattice itself. The devices studied in this thesis are prepared from high-purity IIa CVD diamond, where the spin bath consists of ^{13}C isotopes (natural abundance of 1.1 %). These spins create a fluctuating magnetic field at the location of the NV center that can be described by a Gaussian probability distribution with variance b^2 . This fluctuating field changes the energy level splitting of the electron spin via the Zeeman splitting leading to dephasing on a timescale $T_2^* = \sqrt{2}/b$. This effect is measured in a Ramsey interferometry experiment where the accumulated phase during a free evolution τ of a superposition state is monitored (2.8b). The signal is fitted with a function

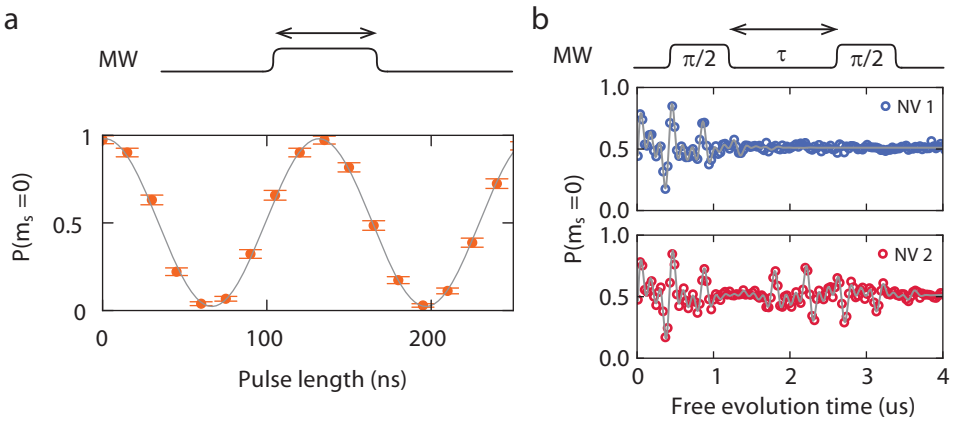


Figure 2.8 | (a) Coherent qubit rotations of the electron spin are performed by varying the length of a MW pulse. Solid line is a sinusoidal fit from which we determine the Rabi frequency (7.67 ± 0.02) MHz. (b) Ramsey measurements for two different NV centers where the wait time between two $\pi/2$ pulses is varied. From a fit to equation 2.2 we find $T_2^* = (0.96 \pm 0.03)$ and $(3.09 \pm 0.05)\mu\text{s}$ for the upper and lower panel respectively. The coupling to the nitrogen spin is $A_{||} = (2.20 \pm 0.01)$ and (2.195 ± 0.002) MHz. For the bottom panel two additional frequency components are included in the fit to account for the strongly coupled ^{13}C . We find a coupling strength of (384 ± 3) kHz. All datapoints are corrected to account for imperfect readout and initialization.

$$P = A \exp(-(\tau/T_2^*)^2) \sum_{k=-1}^1 \cos(2\pi(\delta f + kA_{||})\tau + \phi_k), \quad (2.2)$$

where δf is a detuning of the rotating frame of the microwave pulses with respect to the center frequency of the electron spin. The three frequencies arise from the coupling to the host nitrogen spin which carries a spin $I = 1$. For the NV center in the bottom panel two additional frequencies are included in the fit. They are associated with the coupling to a single ^{13}C spin (with spin $I = 1/2$), which is closer to the defect than the other spins in the bath. In this case the coupling strength of the individual ^{13}C spin to the electron spin is strong (384 ± 3 kHz) compared to the dephasing rate $1/T_2^*$ induced by the spin bath and can therefore be individually resolved. From the gaussian decay of the fit we find $T_2^* = (0.96 \pm 0.03)$ and $(3.09 \pm 0.05)\mu\text{s}$ for the two NV centers. The coherence times can be extended by using isotopically purified samples as shown in chapter 4 of this thesis.

Alternatively the electron spin can be made insensitive to the static component of the fluctuating spin bath by dynamical decoupling (DD) techniques^{9,10}. Here the spin is periodically inverted by equally spaced π pulses as shown in figure 2.9. For a spin echo ($N = 1$)

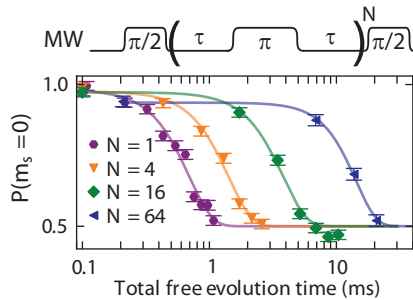


Figure 2.9 | Dynamical Decoupling of the electron spin (a)

the single π pulse inverts the direction of the accumulated phase which leads to perfect refocusing if the effective magnetic field is constant on a timescale of 2τ . By increasing the number of refocusing pulses we demonstrate a coherence time (T_{coh}) of (14.3 ± 0.3) ms for $N = 64$.

So far we presented the Ramsey and dynamical decoupling techniques as a means to characterize the coherence times of the electron spin qubit. Alternatively, one can use the observed decoherence to learn something about the microscopic environment of the NV center. Because the NV center is an atomic defect it can sense DC (Ramsey interferometry) and AC (dynamical decoupling) signals very high spatial resolution. In chapter 4 we present an experiment where real-time feedback techniques are implemented to improve the performance of such a single-spin sensor in Ramsey interferometry. As an example, the data in figure 2.8b demonstrates the detection of single nuclear spins near the NV center.

2.6 Coupling to individual nuclear spins

Nuclear spins in the vicinity of the NV center can be used to define qubits, extending the capabilities of the NV center to a multi-qubit spin register. In recent years full control of both the host nitrogen spin^{11–15} and nearby ¹³C spins^{16–21} has been demonstrated. Since the gyromagnetic ratio of nuclear spins is typically three orders of magnitude smaller compared to the electron spin, they are less sensitive to magnetic fluctuations and therefore exhibit extremely long coherence times²², making them very suitable quantum memories.

2.6.1 Host nitrogen spin

All NV centers have an intrinsic nuclear spin associated with the Nitrogen atom of the defect. Here we will discuss the most common isotope, used in all experiments in this thesis, namely ¹⁴N (99.3 % abundance) which carries a spin $I = 1$. The combined electron-nuclear spin system is described by the following Hamiltonian:

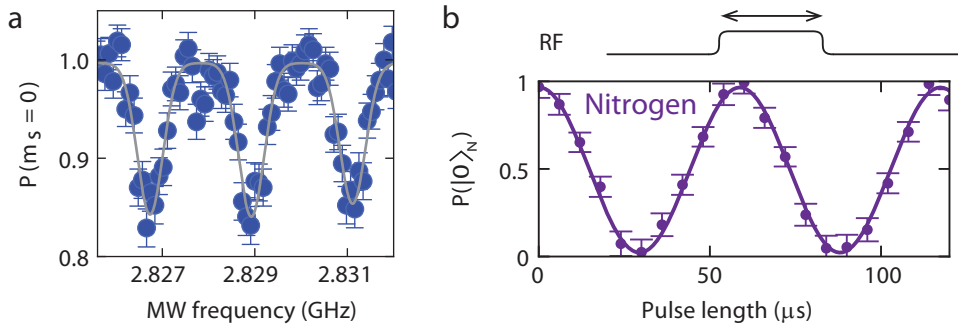


Figure 2.10 | (a)

$$H_{e,N} = H_{GS,e} - QI_{N_z}^2 + \gamma_N \mathbf{B} \cdot \mathbf{I}_N - A_{\parallel} S_z I_{N_z} - A_{\perp} (S_x I_{N_x} + S_y I_{N_y}), \quad (2.3)$$

with I_{N_i} the Nitrogen spin matrices, $\gamma_N = 0.3077$ kHz/G the gyromagnetic ratio of the Nitrogen spin, $Q = 4.98$ MHz the quadrupole splitting and the hyperfine parameters $A_{\parallel} = 2.19$ MHz and $A_{\perp} \approx 2.1$ MHz. The experiments reported in this thesis are performed at magnetic fields where the separation between electron spin levels is large compared to the energy scale of the flip-flop terms ($S_x I_{N_x}$ and $S_y I_{N_y}$). We therefore take the secular approximation which neglect these terms such that the Hamiltonian becomes

$$H_{e,N} = H_{GS,e} - QI_{N_z}^2 + \gamma_N \mathbf{B} \cdot \mathbf{I}_N - A_{\parallel} S_z I_{N_z}. \quad (2.4)$$

For a magnetic field aligned along the z-axis of the defect, the quantization axis of the nitrogen spin is aligned with the electron spin. The parallel component of the hyperfine interaction introduces a splitting of the electron spin transitions that can be observed in a pulsed ESR measurement (figure 2.10a). The three resonances correspond to the nuclear spin eigenstates labeled $m_I = +1, 0, -1$. To encode a qubit we define the logical states as $|0\rangle_N = m_i = -1$ and $|1\rangle_N = m_i = 0$ which can be manipulated with magnetic resonance techniques analogous to the electron spin manipulation (fig 2.10b). The timescale of the manipulation scales inversely with the gyromagnetic ratio, resulting in a rabi frequency of (17.07 ± 0.01) kHz. The nitrogen spin state is initialized and read out by mapping it to the electron spin and subsequently performing optical readout of the electron spin.

2.6.2 ^{13}C spins

In addition to the nitrogen nuclear spin, each NV center is surrounded by a unique configuration of ^{13}C -spins (with spin $I_C = 1/2$) that randomly occupy sites in the spin-free ^{12}C

2. Experimental control and theory of the NV center

diamond lattice. Again taking the secular approximation, the combined Hamiltonian for a single ^{13}C -spin coupling to the NV center is given by:

$$H_{e,N,C} = H_{e,N} + \gamma_C \mathbf{B} \cdot \mathbf{I}_C + A_{\parallel,C} S_z I_{Cz} + A_{\perp,C} S_z I_{Cx}, \quad (2.5)$$

with I_{C_i} the Pauli spin matrices for the Carbon spin, $\gamma_C = 1.0705 \text{ kHz/G}$ the gyromagnetic ratio of the Carbon spin and the hyperfine parameters $A_{\parallel,C}$ and $A_{\perp,C}$ that depend on the distance between the Carbon spin and the electron spin and on the angle with respect to the quantization axis of the NV center. Carbon spins with high coupling strength compared to the dephasing time of the electron spin ($A_C > 1/T_2^*$) can be spectrally resolved via the electron spin and allow for similar control techniques as used for the nitrogen spin^{16–20}. A signature of a strongly coupled carbon spin can be seen in figure 2.8b (bottom panel). Recently it was shown that dynamical decoupling techniques can overcome the limitation set by the electron spin decoherence to detect^{21,23,24} and control²⁵ weakly coupled Carbon spins. In chapter ?? and ADDREF!! we investigate the feasibility to use these weakly coupled carbon spins as quantum memories that are robust against optical excitation of the electron spin.

2.7 Bibliography

- [1] H. Bernien. *Control, measurement and entanglement of remote quantum spin registers in diamond*. PhD thesis, Delft, University of Technology (2014).
- [2] M. W. Doherty *et al.* The nitrogen-vacancy colour centre in diamond. *Physics Reports* **528**, 1 (2013).
- [3] J. P. Hadden *et al.* Strongly enhanced photon collection from diamond defect centers under microfabricated integrated solid immersion lenses. *Appl. Phys. Lett.* **97**, 241901 (2010).
- [4] L. Marseglia *et al.* Nanofabricated solid immersion lenses registered to single emitters in diamond. *Appl. Phys. Lett.* **98**, 133107 (2011).
- [5] M. Jamali *et al.* Microscopic diamond solid-immersion-lenses fabricated around single defect centers by focused ion beam milling. *Rev. Sci. Instrum.* **85**, 123703 (2014).
- [6] T. K. Yeung, D. L. Sage, L. M. Pham, P. L. Stanwix and R. L. Walsworth. Anti-reflection coating for nitrogen-vacancy optical measurements in diamond. *Appl. Phys. Lett.* **100**, 251111 (2012).
- [7] P. Siyushev *et al.* Optically controlled switching of the charge state of a single nitrogen-vacancy center in diamond at cryogenic temperatures. *Phys. Rev. Lett.* **110**, 167402 (2013).
- [8] L. Robledo *et al.* High-fidelity projective read-out of a solid-state spin quantum register. *Nature* **477**, 574 (2011).
- [9] G. d. Lange, Z. H. Wang, D. Ristè, V. V. Dobrovitski and R. Hanson. Universal dynamical decoupling of a single solid-state spin from a spin bath. *Science* **330**, 60 (2010).
- [10] C. A. Ryan, J. S. Hodges and D. G. Cory. Robust decoupling techniques to extend quantum coherence in diamond. *Phys. Rev. Lett.* **105**, 200402 (2010).
- [11] T. Gaebel *et al.* Room-temperature coherent coupling of single spins in diamond. *Nat Phys* **2**, 408 (2006).
- [12] R. Hanson, F. M. Mendoza, R. J. Epstein and D. D. Awschalom. Polarization and readout of coupled single spins in diamond. *Phys. Rev. Lett.* **97**, 087601 (2006).
- [13] P. Neumann *et al.* Single-shot readout of a single nuclear spin. *Science* **329**, 542 (2010).
- [14] G. D. Fuchs, G. Burkard, P. V. Klimov and D. D. Awschalom. A quantum memory intrinsic to single nitrogen-vacancy centres in diamond. *Nat Phys* **7**, 789 (2011).
- [15] T. van der Sar *et al.* Decoherence-protected quantum gates for a hybrid solid-state spin register. *Nature* **484**, 82 (2012).

2. Experimental control and theory of the NV center

- [16] F. Jelezko *et al.* Observation of coherent oscillation of a single nuclear spin and realization of a two-qubit conditional quantum gate. *Phys. Rev. Lett.* **93**, 130501 (2004).
- [17] M. V. G. Dutt *et al.* Quantum register based on individual electronic and nuclear spin qubits in diamond. *Science* **316**, 1312 (2007).
- [18] P. Neumann *et al.* Multipartite entanglement among single spins in diamond. *Science* **320**, 1326 (2008).
- [19] L. Jiang *et al.* Repetitive readout of a single electronic spin via quantum logic with nuclear spin ancillae. *Science* **326**, 267 (2009).
- [20] B. Smeltzer, J. McIntyre and L. Childress. Robust control of individual nuclear spins in diamond. *Phys. Rev. A* **80**, 050302 (2009).
- [21] T. H. Taminiau *et al.* Detection and control of individual nuclear spins using a weakly coupled electron spin. *Phys. Rev. Lett.* **109**, 137602 (2012).
- [22] P. C. Maurer *et al.* Room-temperature quantum bit memory exceeding one second. *Science* **336**, 1283 (2012).
- [23] S. Kolkowitz, Q. P. Unterreithmeier, S. D. Bennett and M. D. Lukin. Sensing distant nuclear spins with a single electron spin. *Phys. Rev. Lett.* **109**, 137601 (2012).
- [24] N. Zhao *et al.* Sensing single remote nuclear spins. *Nat Nano* **7**, 657 (2012).
- [25] T. H. Taminiau, J. Cramer, T. v. d. Sar, V. V. Dobrovitski and R. Hanson. Universal control and error correction in multi-qubit spin registers in diamond. *Nat Nano* **9**, 171 (2014).

CHAPTER 3

MANIPULATING A QUBIT THROUGH THE BACKACTION OF SEQUENTIAL PARTIAL MEASUREMENTS AND REAL-TIME FEEDBACK

M.S. Blok*, C. Bonato*, M.L. Markham, D.J. Twitchen, V.V. Dobrovitski and R. Hanson

Quantum measurements not only extract information from a system but also alter its state. Although the outcome of the measurement is probabilistic, the backaction imparted on the measured system is accurately described by quantum theory^{1–3}. Therefore, quantum measurements can be exploited for manipulating quantum systems without the need for control fields^{4,5}. We demonstrate measurement-only state manipulation on a nuclear spin qubit in diamond by adaptive partial measurements. We implement the partial measurement via tunable correlation with an electron ancilla qubit and subsequent ancilla readout^{6,7}. We vary the measurement strength to observe controlled wavefunction collapse and find post-selected quantum weak values^{6–10}. By combining a novel quantum non-demolition readout on the ancilla with real-time adaption of the measurement strength we realize steering of the nuclear spin to a target state by measurements alone. Besides being of fundamental interest, adaptive measurements can improve metrology applications^{11,12} and are key to measurement-based quantum computing^{13,14}.

This chapter has been published in *Nature Physics* **10**, 189–193 (2014).

* these authors contributed equally to this work

3.1 Introduction

Measurements play a unique role in quantum mechanics and in quantum information processing. The backaction of a measurement can be used for state initialization^{15,16}, generation of entanglement between non-interacting systems^{17–20}, and for qubit error detection²¹. These measurement-based applications require either post-selection or real-time feedback, as the outcome of a measurement is inherently probabilistic. Recent experiments achieved quantum feedback control on a single quantum system^{20,22–24} by performing coherent control operations conditioned on a measurement outcome.

Here, we realize real-time adaptive measurements and exploit these in a proof-of-principle demonstration of measurement-only quantum feedback. Our protocol makes use of partial measurements that balance the information gain and the measurement backaction by varying the measurement strength. We accurately control the measurement strength and the corresponding backaction in a two-qubit system by tuning the amount of (quantum) correlation between the system qubit and an ancilla qubit, followed by projective readout of the ancilla^{6,7}. In general, the backaction of sequential partial measurements leads to a random walk^{1–3} but by incorporating feedback, multiple measurements can direct the trajectory of a qubit towards a desired state^{4,5}. Real-time adaptive measurements are a key ingredient for quantum protocols such as one-way quantum computing^{13,14} and Heisenberg-limited phase estimation^{11,12}.

We implement the adaptive partial measurements in a nitrogen vacancy (NV) center in synthetic diamond. We define the system qubit by the nuclear spin of the NV host nitrogen ($|\downarrow\rangle$: $m_I=0$, $|\uparrow\rangle$: $m_I=-1$), and the ancilla qubit by the NV electron spin ($|0\rangle$: $m_S=0$, $|1\rangle$: $m_S=-1$) (Fig. 3.1a). The ancilla is initialized and read out in a single shot with high fidelity using spin-selective optical transitions¹⁵. We perform single-qubit operations on the ancilla by applying microwave frequency pulses to an on-chip stripline.

3.2 Variable-strength measurement

We realize the variable-strength measurement by correlating the system qubit with the ancilla through a controlled-phase-type gate (Fig. 3.1b) that exploits the hyperfine interaction, which (neglecting small off-diagonal terms) has the form $\hat{H}_{hf} = A \hat{S}_z \hat{I}_z$ (with $A = 2\pi \times 2.184 \pm 0.002$ MHz and \hat{S}_z , \hat{I}_z the three-level Pauli z-operators for the electron, nuclear spin respectively). During free evolution, the ancilla qubit precession is conditional on the state of the system qubit. We choose the rotating frame such that the ancilla rotates clockwise (anti-clockwise) around the z-axis if the system qubit is in $|\uparrow\rangle$ ($|\downarrow\rangle$) and vary the interaction time τ . For $\tau = 0$, there is no correlation between the ancilla and the system, whereas for $\tau = \frac{\pi}{A}$, corresponding to the rotation angle $\theta = 90^\circ$, the two are maximally correlated. A subsequent rotation and projective readout of the ancilla then implements a measurement of the system qubit, with a measurement strength that can be accurately tuned by controlling the interaction time τ . A mathematical derivation can be found in the methods.

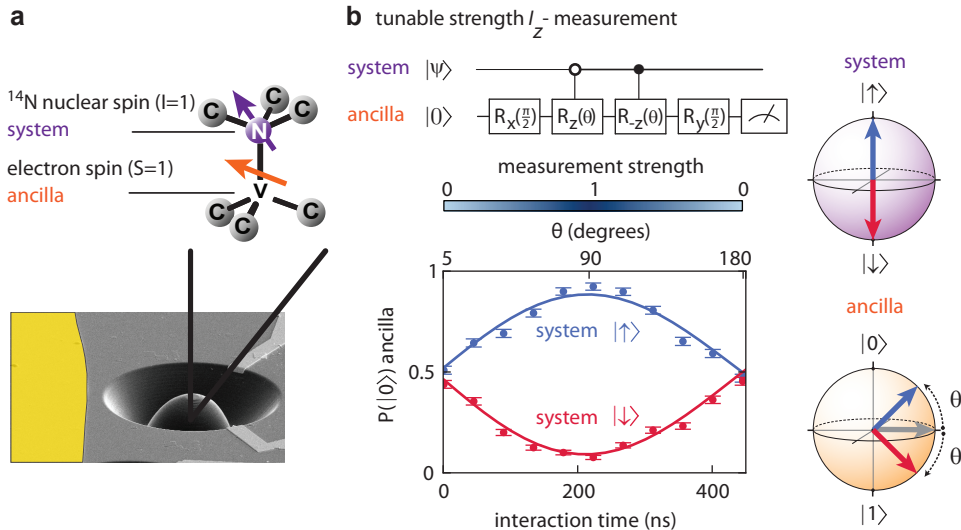


Figure 3.1 | Partial measurement of a spin qubit in diamond. (a) The NV center is a natural two-qubit system where the system qubit is defined by the ¹⁴N nuclear spin and the ancilla qubit is defined by the electron spin. A solid-immersion-lens is deterministically fabricated on top of the selected NV center to increase the photon collection efficiency. Control fields for single qubit rotations are generated by applying a current to the gold stripline (yellow). (b) A tunable strength measurement is implemented by a Ramsey-type gate on the ancilla. We plot the probability to measure the state $|0\rangle$ for the ancilla, as a function of interaction time τ , for two system input states $|\downarrow\rangle$ (red) and $|\uparrow\rangle$ (blue). The Bloch-spheres show the state of the system (purple) and ancilla (orange) after the entangling-gate for the different input states (red and blue vectors). The colour bar represents the measurement strength, proportional to $\sin \theta$, where $\theta = \frac{A\tau}{2}$. Blue corresponds to a projective measurement and white to no measurement. Solid lines are a fit to the function $y_0 + e^{-(\frac{\tau}{T_2^*})^2} \cos(A\tau + \delta)$. From the phase offset δ we find the weakest measurement we can perform, corresponding to $\theta = 5^\circ$. This is limited by free evolution of the ancilla during the pulses.(see Methods). Error bars depict 68 % confidence intervals. Sample size is 500 for each data point.

We investigate the measurement-induced backaction by preparing an initial state of the system ($|\uparrow\rangle$, $|x\rangle$ and $|y\rangle$) and performing a partial measurement with strength θ , followed by state tomography (Fig. 3.2a). First, we neglect the outcome of the partial measurement, which is mathematically equivalent to taking the trace over the state of the ancilla qubit. In this case the backaction is equivalent to pure dephasing as can be seen by a measured reduction of the length of the Bloch vector (Fig. 3.2b). Next, we condition the tomography on the ancilla measurement yielding state $|0\rangle$ (Fig. 3.2c). We observe that for a weak measurement ($\theta = 5^\circ$), the system is almost unaffected, whereas for increasing measurement strength it receives a stronger kick towards $|\uparrow\rangle$ (Fig. 3.2c). Crucially, we find that the length of the Bloch vector is preserved in this process, as expected for an initially pure state. This shows that the partial collapse is equivalent to a qubit rotation that is conditional on the measurement strength and outcome and on the initial state. By performing quantum process tomography, we find that both measurement processes agree well with the theoretical prediction (the process fidelities are 0.986 ± 0.004 and 0.94 ± 0.01 for the unconditional and conditional process, respectively; see Methods).

3.3 Generalized weak value

By combining a partial measurement with post-selection on the outcome of a subsequent projective measurement, we can measure the generalized weak value ${}_f\langle I_z \rangle$ (conditioned average of contextual values²⁵, see methods) of the nuclear spin in the z -basis. In the limit of zero measurement strength ($\theta = 0^\circ$), this quantity approximates the weak value⁸ $W = \frac{\langle \psi_f | \hat{I}_z | \psi_i \rangle}{\langle \psi_f | \psi_i \rangle}$, where $\psi_i(\psi_f)$ is the initial (final) state of the nucleus and from here we define \hat{I}_z as the Pauli z -operator reduced to a two-level system with eigenvalues $+1$ and -1 . By post-selecting only on the final states having small overlap with the initial state, ${}_f\langle I_z \rangle$ can be greatly amplified to values that lie outside the range of eigenvalues of the measured observable. As shown in Fig. 3.3, by sweeping the angle between the initial and final states we observe up to tenfold amplification (${}_f\langle I_z \rangle = 10 \pm 3$) compared to the maximum eigenvalue of I_z ($+1$). This amplification is the highest reported for a solid-state system to date⁷. As predicted²⁶, we observe that values of ${}_f\langle I_z \rangle$ lying outside of the range of eigenvalues of I_z can be found for any finite measurement strength.

3.4 QND-measurement of the ancilla qubit

Using the partial measurements for measurement-based feedback requires reading out the ancilla without perturbing the system qubit. In our experiment the system qubit can dephase during ancilla readout both through a spin-flip of the electron in the course of optical excitation (Fig. 3.4b) and as a result of the difference in the effective nuclear g-factor in the electronic ground- and optically excited state²⁷. Note that for the characterization of a single partial measurement (Fig. 3.2) we circumvent this dephasing by interchanging the

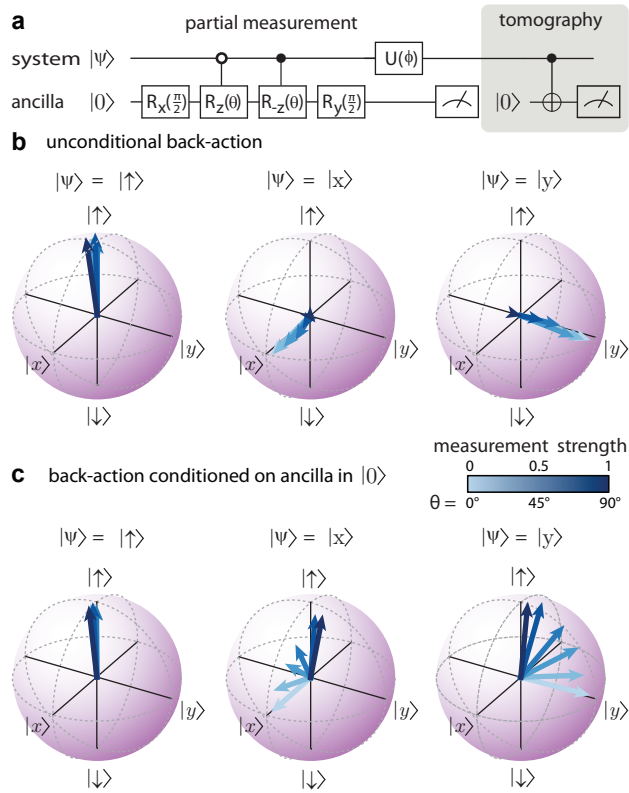


Figure 3.2 | Measurement backaction for variable-strength measurement. (a) We prepare an initial state of the system ($|\uparrow\rangle$, $|x\rangle$ and $|y\rangle$), perform a partial measurement with strength θ , and characterize the measurement backaction on the system by quantum state tomography. Quantum state tomography is implemented by an ancilla-assisted projective measurement, performed with the same protocol, setting $\tau = 229$ ns for $\theta = 90^\circ$. The nuclear spin basis rotation is performed with a $\frac{\pi}{2}$ radio-frequency pulse (along either x or y). The basis rotation pulse for the tomography is applied before the readout of the ancilla, to avoid the dephasing induced by the state-characterization measurement (see main text). The data is corrected for errors in the readout and initialization of the system qubit, both of which are obtained from independent measurements (see methods). (b,c) Measurement backaction for a partial measurement of increasing strength, independent of the measurement result for the ancilla qubit (b), or conditioned on the ancilla in $|0\rangle$ (c).

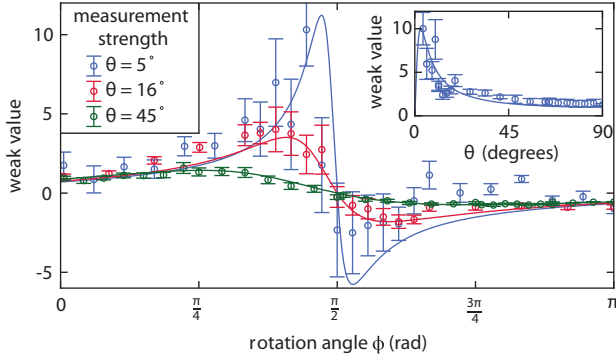


Figure 3.3 | Generalized quantum weak value. Measurement of a generalized weak value for the nuclear-spin qubit, performed by a partial measurement of strength θ , followed by a strong measurement and post-selection of the state $|↓\rangle$, as a function of the basis rotation angle ϕ of the strong measurement (Fig. 3.2a). Solid lines are simulations using independently determined parameters. The asymmetry in the curve can be explained by asymmetric nuclear spin flips arising during ancilla initialisation by optical excitation of the forbidden transition of E_y (see methods). Inset: the generalized weak values as a function of the strength θ of the partial measurement, setting the basis rotation angle of the strong measurement to the optimal value $\phi = \frac{\pi}{2} - \theta$. All error bars depict 68 % confidence intervals. The sample size varies per data point because each data point has different post-selection criterion.

measurement basis rotation and the ancilla readout; this interchange is not possible for real-time adaptive measurements.

To mitigate the nuclear dephasing during ancilla readout we reduce the ancilla spin-flip probability using a dynamical-stop readout technique. We partition the optical excitation time in short ($1\ \mu\text{s}$) intervals and we stop the excitation laser as soon as a photon is detected, or after a predetermined maximum readout time when no photon is detected (Fig. 3.4a). This reduces redundant excitations without compromising the readout fidelity. In Fig. 3.4b we show the correspondence between pre- and post-measurement states for the two eigenstates of the ancilla. For the state $|0\rangle$ the dynamical-stop readout increases the fidelity ($F = \langle \psi_i | \rho_m | \psi_i \rangle$, where ρ_m is the density matrix of the system after the ancilla readout) from 0.18 ± 0.02 to 0.86 ± 0.02 . The latter fidelity is solely limited by the cases where the spin flipped before a photon was detected: we find $F = 1.00 \pm 0.02$ for the cases in which a photon was detected. As expected, the fidelity is high ($F = 0.996 \pm 0.006$) for input state $|1\rangle$ as this state is unaffected by the excitation laser. The dynamical-stop technique thus implements a quantum non-demolition (QND) measurement of the ancilla electron spin with an average

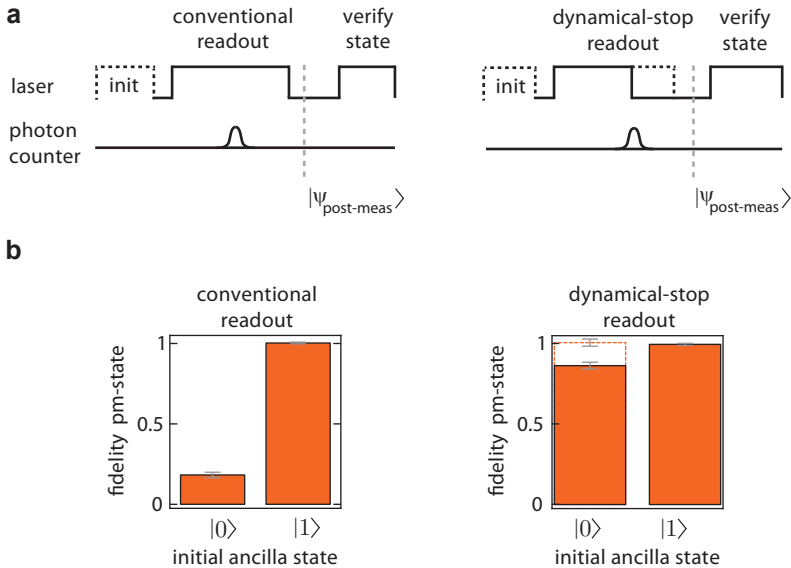


Figure 3.4 | Quantum non-demolition measurement of the ancilla qubit (a) The ancilla is initialized in $|0\rangle$ ($|1\rangle$) by optically pumping the A_2 (E_y) transition. The ancilla is then read out by exciting the E_y transition for $100 \mu\text{s}$ (conventional readout), or until a photon was detected (dynamical-stop readout). Finally, we verify the post-measurement state with a conventional readout. (b) Fidelity of the post-measurement state of the ancilla for conventional readout (left graph) and dynamical-stop readout (right graph). Results are corrected for the infidelity in the final readout. All error bars depict 68 % confidence intervals. Sample size per datapoint is 5000

fidelity of 0.93 ± 0.01 for the post-measurement state.

The dynamical-stop readout of the ancilla significantly reduces the dephasing of the nuclear spin qubit during measurement as shown in Fig. 3.5. Starting with the nuclear spin in state $|x\rangle = \frac{|0\rangle + |1\rangle}{\sqrt{2}}$, a conventional readout of the ancilla completely dephases the nuclear spin, leading to a state fidelity with respect to $|x\rangle$ of 0.5. In contrast, the fidelity of the dynamical-stop readout saturates to 0.615 ± 0.002 (probably limited by changes in the effective g-factor of the nuclear spin). The dynamical-stop readout thus leaves the system in a coherent post-measurement state that can be used in a real-time feedback protocol.

3.5 Control by adaptive measurements

Preserving coherence of the post-measurement state enables a proof-of-principle realization of measurement-only control, by implementing sequential measurements and tun-

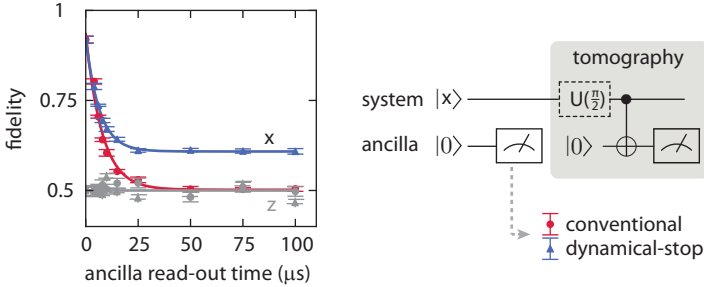


Figure 3.5 | System qubit coherence during ancilla readout. Coherence of the system qubit state after ancilla readout. For the dynamical-stop protocol we define the ancilla readout time as the predetermined maximum readout time. The graph shows the fidelity of the system with respect to $|x\rangle$ for conventional readout (red) and dynamical-stop readout (blue). The z -component of the system is unaffected as shown by the constant fidelity with respect to $|\uparrow\rangle$ (grey). All error bars depict 68 % confidence intervals. Sample size per datapoint is 2000

ing the strength of the second measurement in real time conditioned on the outcome of the first measurement (Fig. 3.6a). We choose as our target the creation of the state $|\psi\rangle = \cos(\frac{\pi}{4} + \frac{\theta_1}{2}) |\downarrow\rangle + \cos(\frac{\pi}{4} - \frac{\theta_1}{2}) |\uparrow\rangle$ from initial state $|x\rangle$ using only partial measurements of \hat{I}_z . The first measurement with strength θ_1 will prepare either the desired state, or the state $|\psi_{wrong}\rangle = \cos(\frac{\pi}{4} - \frac{\theta_1}{2}) |\downarrow\rangle + \cos(\frac{\pi}{4} + \frac{\theta_1}{2}) |\uparrow\rangle$, each with probability 0.5. We adapt the strength of the second measurement θ_2 according to the outcome of the first measurement: we set $\theta_2 = 0$ if the first measurement directly yielded the target state, but if the wrong outcome was obtained we set the measurement strength to

$$\theta_2 = \sin^{-1} \left[2 \frac{\sin \theta_1}{1 + \sin^2 \theta_1} \right], \quad (3.1)$$

such that the second measurement will probabilistically rotate the qubit to the target state (see methods). The total success probability of this two-step protocol is $p_{suc} = \frac{1}{2}(1 + \cos \theta_1)$ and a successful event is heralded by the outcome of the ancilla readout. In principle the protocol can be made fully deterministic⁴ by incorporating a reset in the form of a projective measurement along the x -axis.

To find the improvement achieved by the feedback, we first compare the success probability of our adaptive measurement protocol to the success probability for a single measurement (Fig. 3.6b right panel). The success probability clearly increases with the adaptive protocol and is proportional to the readout fidelity of the $|0\rangle$ state of the ancilla, which is maximum for readout times $> 25 \mu s$. The fidelity of the final state (Fig. 3.6b left panel) is limited by the remaining dephasing of the system during readout of the ancilla as shown in Fig. 3.5. This

constitutes the trade-off between success probability and state fidelity.

We show that the increase in success probability is enabled by feedback by comparing the final state fidelity with and without feedback (Fig. 3.6b left panel). In principle the success probability can be increased in the absence of feedback by accepting a certain number of false measurement outcomes at the cost of a reduced fidelity. We calculate the maximum fidelity that can be achieved in this way by performing only the first measurement and increasing the success probability to that of the adaptive protocol using post-selection (grey line in Fig. 3.6b, left panel). We find that the measured state fidelity in the adaptive protocol is above this bound (Fig. 3.6b, green area), which indicates that the adaptive measurement indeed successfully corrects the kickback from the first measurement, thus yielding a clear advantage over open-loop protocols.

We note that, in contrast to pioneering adaptive measurement experiments on photons that only used experimental runs in which a photon was detected at each measurement stage¹⁴, our protocol is fully deterministic in the sense that the partial measurement always yields an answer. In particular, the data in Fig. 3.6 includes all experimental runs and thus no post-selection is performed, as desired for future applications in metrology and quantum computing.

The performance of the protocol can be further improved by increasing the ancilla readout fidelity (either by improving the collection efficiency or reducing spin-flip probability) and by further reducing the dephasing of the system during readout. A particularly promising route is to use nuclear spins farther away from the NV center (for example carbon-13 spins) that have much smaller hyperfine couplings^{28–30} and are more robust against changes in the orbital state of the electron spin.

Our work is the first experimental exploration of a fundamental concept of control-free control^{4,5,31}. Furthermore, the use of adaptive measurements as presented here can increase the performance of spin-based magnetometers^{11,12}. Finally, our results can be combined with recently demonstrated methods for generating entanglement between separate nitrogen vacancy centre spins^{32,33}. Taken together, these techniques form the core capability required for one-way quantum computing, where quantum algorithms are executed by sequential adaptive measurements on a large entangled ‘cluster’ state^{13,14}.

3. Manipulating a qubit through the backaction of adaptive measurements

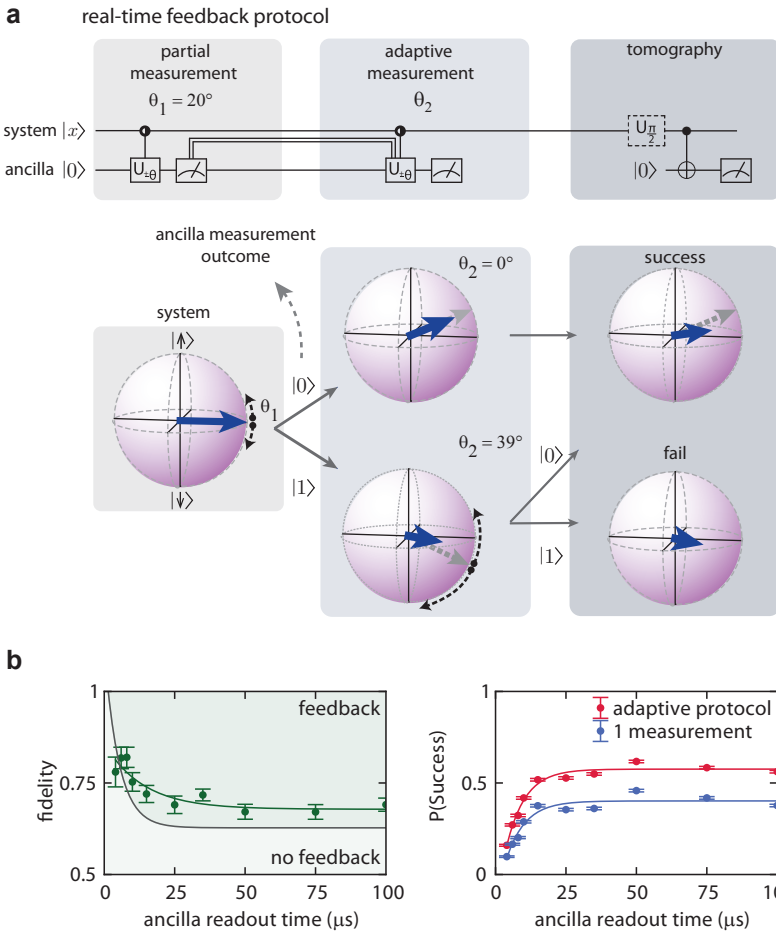


Figure 3.6 | Manipulation of a nuclear spin state by sequential partial adaptive measurements with real-time feedback. (a) Adaptive measurement protocol. The ancilla qubit is initialized in $|0\rangle$ and the system qubit is prepared in $|x\rangle$. The strength of the second measurement (θ_2) is adjusted according to the outcome of the first measurement. The system is analysed by state tomography at each intermediate step. The result of the tomography is plotted on the bloch spheres (blue vector) and compared with the ideal case (grey vector). (b) Fidelity of the output state with respect to the target state as a function of ancilla readout time (dynamical-stop readout) with feedback (only the cases where the protocol heralds success). The grey line is obtained by performing one measurement and adding negative results to artificially increase the success probability to that of the adaptive protocol (red line in right panel). In the right panel we show the probability that the protocol heralds success for one measurement and for the adaptive protocol.

3.6 Methods

We use a naturally-occurring nitrogen-vacancy center in high-purity type IIa CVD diamond, with a $<111>$ -crystal orientation obtained by cleaving and polishing a $<100>$ -substrate. Experiments are performed in a bath cryostat, at the temperature of 4.2 K, with an applied magnetic field of 17 G. Working at low-temperature, we can perform efficient electron spin initialization ($F = 0.983 \pm 0.006$) and single-shot readout (the fidelity is 0.853 ± 0.005 for $m_S = 0$ and 0.986 ± 0.002 for $m_S = -1$) by spin-resolved optical excitation¹⁵. Initialization of the nuclear spin is done by measurement¹⁵, with fidelity 0.95 ± 0.02 . Single-qubit operations can be performed with high accuracy using microwave (for the electron) and radio-frequency (for the nucleus) pulses applied to the gold stripline. Note that the single-qubit operations on the nucleus are only used for state preparation and tomography, but not in the feedback protocol. The dephasing time T_2^* is (7.8 ± 0.2) ms for the nuclear spin and (1.35 ± 0.03) μ s for the electron spin.

3.6.1 Levels and Hamiltonian

The NV center forms a natural two qubit system: the electron spin serves as the ancilla qubit, while the system qubit is implemented on the spin of the NV nitrogen atom. The relevant levels are plotted in Fig. 3.7: the full level scheme can be found in the Supporting Online Material of Pfaff *et al.*¹⁹.

The electron spin is given by the collective spin of the six unpaired electrons of the negatively-charged state of the center, which constitute a spin $S = 1$ system. The $m_s = 0$ state is separated from the $m_s = \pm 1$ states by the zero-field splitting ($D = 2.878 \pm 0.001$ GHz). The $m_s = -1$ and $m_s = +1$ states are split by 98 MHz by an external magnetic field ($B = 17.5G$). The ancilla qubit is defined by the $m_s = 0(|0\rangle)$ and $m_s = -1(|1\rangle)$ states. Electron spin rotations are performed by microwave pulses, with a Rabi frequency of 7.67 MHz. The probability to excite the $m_s = +1$ spin state when driving microwaves is negligible. The electron spin coherence time has been measured to be $T_2^* = (1.35 \pm 0.03)$ μ s by a Ramsey experiment.

The NV's nitrogen atom (^{14}N) carries $I = 1$ spin and the system qubit is defined by the $m_I = -1(|\uparrow\downarrow\rangle)$ and $m_I = 0(|\downarrow\downarrow\rangle)$ levels, separated in frequency by $\Omega_N = |Q| + g_N \mu_N B \sim 2\pi \times 5$ MHz, where Q is the nuclear quadrupole splitting $Q = -2\pi \times 4.98$ MHz. The hyperfine interaction between the electron and nuclear spin has the form $\hat{\mathcal{H}}_{hf} \sim A_z \hat{I}_z \hat{S}_z$ (neglecting small off-diagonal terms), which further splits the nuclear levels by an amount $A_z = -2\pi \times 2.184 \pm 0.002$ MHz when the electron is in the $m_s = -1$ manifold. Nuclear spin rotations are performed by radio-frequency pulses, with a Rabi frequency of 17 kHz. The nuclear spin coherence time has been measured by a Ramsey experiment to be $T_2^* = 7.8 \pm 0.3$ ms (Fig. 3.8).

The Hamiltonian of the system is $\hat{\mathcal{H}} = \hat{\mathcal{H}}_0 + \hat{\mathcal{H}}_{drive}$, with:

$$\hat{\mathcal{H}}_0 = -|Q| |0, \uparrow\downarrow\rangle \langle 0, \uparrow\downarrow| + \Delta |1, \downarrow\downarrow\rangle \langle 1, \downarrow\downarrow| + (\Delta - |Q + A_z|) |1, \uparrow\uparrow\rangle \langle 1, \uparrow\uparrow| \quad (3.2)$$

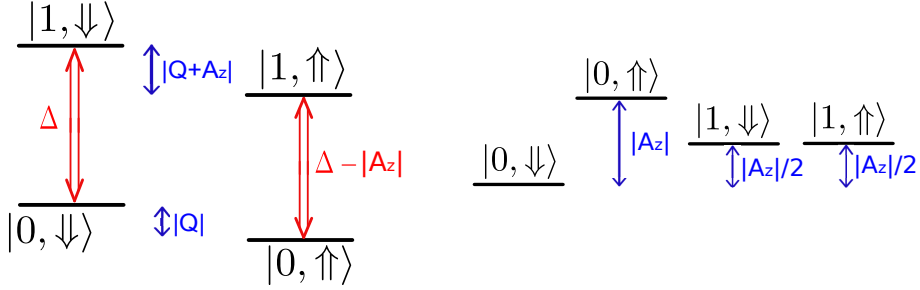


Figure 3.7 | On the left, scheme of the relevant energy levels for the electron and nuclear spin qubits. On the right, level energies in a doubly-rotating reference frame, rotating at frequency $\omega_e = \Delta - |A_z|/2$ for the electron spin, and $\omega_n = |Q + A_z|$ for the nuclear spin.

and:

$$\hat{\mathcal{H}}_{drive} = \Omega_{MW}(t) \hat{S}_x \otimes \hat{1}_N + \Omega_{RF}(t) |1\rangle \langle 1| \otimes \hat{I}_x + \text{h. c.} \quad (3.3)$$

where $\Delta = D - g_e \mu_e B = 2.8288 \pm 0.0002$ GHz and \hat{S}_i , \hat{I}_i are respectively the Pauli operators for the electron spin and the nuclear spin.

The Hamiltonian in Eq. 3.3 is time-dependent and state evolution has, in general, no analytical solution. In order to simplify the problem, we apply the rotating-wave approximation³⁴, using a doubly-rotating frame: one rotating at the driving frequency for the electron spin, and the other one at the driving frequency for the nuclear spin. We set the microwave frequency ($\omega_e = \Delta - |A_z|/2$) such that it is detuned by $|A_z|/2$ from both hyperfine transitions and the RF-field is on resonance with the nuclear spin transition in the $m_s = -1$ electron spin manifold ($\omega_N = |Q + A_z|$). Applying the unitary transformation $\hat{U} = e^{-i(\omega_N \hat{1}_e \times \hat{I}_z + \omega_e \hat{S}_z \times \hat{1}_N)t}$ and retaining the secular terms, the Hamiltonian, in the basis $\{|0, \downarrow\downarrow\rangle, |0, \uparrow\uparrow\rangle, |1, \downarrow\downarrow\rangle, |1, \uparrow\uparrow\rangle\}$, becomes:

$$\hat{\mathcal{H}}' = \begin{bmatrix} 0 & 0 & \Omega_{MW}^* & 0 \\ 0 & |A_z| & 0 & \Omega_{MW}^* \\ \Omega_{MW} & 0 & |A_z|/2 & \Omega_{RF}^* \\ 0 & \Omega_{MW} & \Omega_{RF} & |A_z|/2 \end{bmatrix} \quad (3.4)$$

The energy levels, in the rotating-wave approximation, are shown on the right side of Fig. 3.7. We define the positive quantity A to be $A = |A_z|$ in the rest of the Supplementary Information.

3.6.2 Qubit initialization

The electron spin is initialized in the $m_s = 0$ state by optical spin-pumping with a fidelity 0.983 ± 0.006^{15} . We use the forbidden transition of E_y which is detuned by Δ from the spin-preserving E_y -transition. This transition is well suited for a reset of the electron spin during the protocol, since flip-flops with the nuclear spin are suppressed due to selection rules.

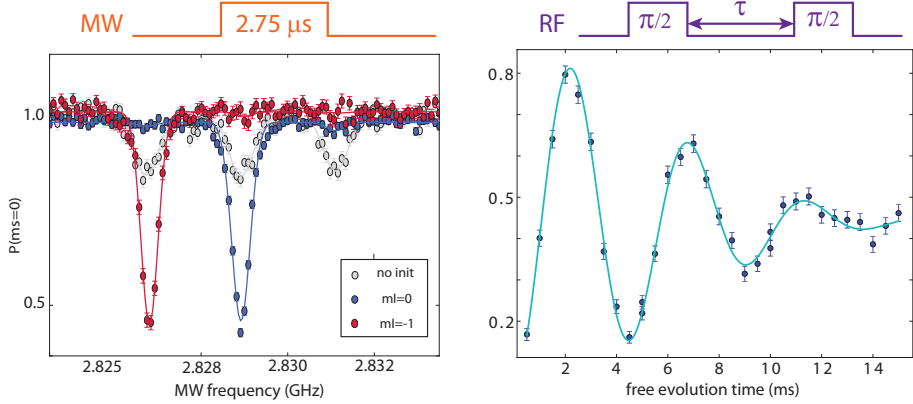


Figure 3.8 | On the left, nuclear spin initialization. The nuclear spin is initially unpolarized (gray): the ESR spectrum for the $m_s = -1 \leftrightarrow 0$ transition shows three hyperfine lines, corresponding to $m_I = -1, 0, +1$. By measurement-based initialization (MBI)¹⁹ we can initialize the spin in any of the nuclear spin states (blue/red). On the right, nuclear spin Ramsey. The nuclear spin is initialized by MBI after which the free evolution time τ between two $\pi/2$ -pulses is varied. The solid line is a fit to the function $y_0 + e^{-(\frac{\tau}{T_2^*})^2} \cos(\omega_{det}\tau + \phi)$ from which we find the dephasing time $T_2^* = 7.8 \pm 0.2 \text{ ms}$.

The nuclear spin is initialized by measurement¹⁹ as shown in Fig. 3.8. We prepare the electron spin state in $|m_s = \pm 1\rangle$ by spin-pumping on the E_y transition. We apply a selective microwave π -pulse ($f_{rabi} = 181.8 \text{ kHz}$) to the electron, on resonance with one of the three hyperfine lines. We then read-out the electron spin state, by exciting the E_y transition. In case of photon detection, the electron state is projected to $m_s = 0$, and the nuclear spin is projected on the state that was addressed by the microwave pulse. During the selective microwave pulse, the electron spin undergoes significant dephasing, reducing the success probability, but not the initialization fidelity of the nuclear spin. The measured initialization fidelity is 0.95 ± 0.02 , obtained from the fitting the height of the peaks in Fig. 3.8 and the success probability is around 0.07. The success probability is determined by $p = p_{m_s=-1} \cdot p_{m_I=-1} \cdot p_{e-flip} \cdot p_{phot}$, where the relevant parameters are:

- $p_{m_s=-1} \sim 0.5$ is the probability to spin pump the electron spin in $m_s = -1$ (in the

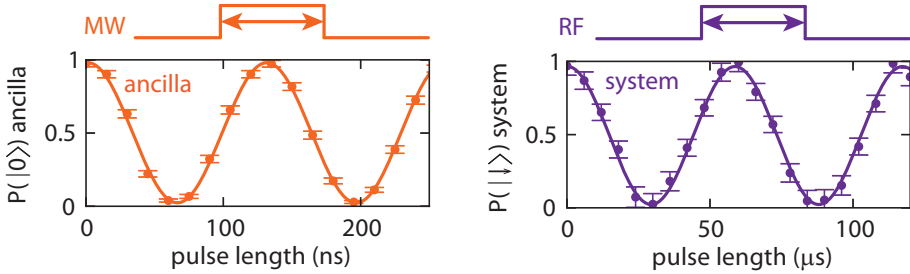


Figure 3.9 |Coherent single-qubit rotations of the electron spin ancilla qubit (orange) and the nuclear spin system qubit (purple) are performed by varying the length of a MW (RF) pulse. Solid lines are sinusoidal fits from which we determine the Rabi frequency 7.67 ± 0.02 MHz / 17.07 ± 0.01 kHz).

remaining cases it's in $m_s = +1$).

- $p_{m_I=-1} \sim 1/3$ is the population of the desired state $m_I = -1$ for an initially unpolarized nuclear spin.
- $p_{e-flip} \sim 0.6$ is the success probability of nuclear-dependent electron spin rotations.
- $p_{phot} \sim 0.6 - 0.8$ is the probability to detect a photon when reading-out the $m_s = 0$ state, limited by the collection of the optical system and the finite photon detection efficiency.

3.6.3 Nucleus-independent electron spin rotations

The maximum Rabi frequency we achieve in the setup is ~ 8 MHz (Fig. 3.9). Given the hyperfine splitting of 2.184 MHz, these pulses introduce off-resonant driving errors that limit the weakest measurement we could achieve to $\theta = 15$ degrees ($C = 0.27$, see equation 3.10). To overcome this problem, we use CORPSE pulses³⁵, a composite pulse sequence designed to compensate for off-resonance errors. The weakest measurement we achieve with the CORPSE pulses is $\theta_{min} = 5$ degrees, corresponding to $\tau = 12$ ns (obtained from a fit of the Ramsey fringes in Fig. 3.1b of the main text)

3.6.4 Electron-independent nuclear spin rotation

For quantum state tomography and for weak-value measurements, we need to be able to perform nuclear spin rotations, unconditional on the electron spin state. This is not trivial if the electron and nuclear spins are entangled. In particular, when the electron is in the $|m_s = -1\rangle$ state, the splitting between $|\downarrow\rangle$ and $|\uparrow\rangle$ is $\omega_N^{(-1)} = |Q + A_z| = 2\pi \times 7.164$ MHz, while when the electron in the $|m_s = 0\rangle$ state, $\omega_N^{(0)} = |Q| = 2\pi \times 4.98$ MHz. Given that the Rabi frequency of the nuclear spin is much smaller than the hyperfine interaction, the

simple use of a hard π -pulse, as done for the electron, does not work.

We implemented the unconditional nuclear spin rotation using the scheme depicted in Fig. 3.10a. First we apply an RF pulse (RF-1) at $\omega_N^{(-1)}$, to rotate the nuclear spin when the electron spin is in the $|m_s = -1\rangle$ manifold. We then apply a hard π -pulse to the electron and apply a second RF pulse (RF-2) at the same frequency $\omega_N^{(-1)}$.

As explained in Section 3.6.5 (Eq. 3.7), the partial measurement introduces a phase shift to the system qubit that depends on the measurement strength. The phase shift is proportional to the interaction time τ of the measurement. In order to characterize the phase shift, we used the following protocol:

- we set the pulse length of RF-1 and RF-2 corresponding to a $\pi/2$ pulse ($T_{RF-1/2} = 14.6\mu s$)
- we only apply the RF-1 pulse and sweep the phase of RF-1 for different values of τ . Fitting the resulting sinusoidal signal, we recover the phase offset $\varphi_0^{(RF-1)}(\tau)$
- we then set the amplitude of RF-2 to the value corresponding to a $\pi/2$ -pulse and without RF-1 apply a π -pulse on the electron followed by RF-2. We then sweep the phase of RF-2 for different values of τ and fit the sinusoid to reconstruct the phase offset $\varphi_0^{(RF-2)}(\tau)$

The values of the phase offsets as a function of τ for RF-1 and RF-2 ($\varphi_0^{(RF-1)}(\tau)$ and $\varphi_0^{(RF-2)}(\tau)$) are plotted in Fig. 3.10b. These values can be used to make sure that the resulting entangled nuclear-electron state has the correct phase when performing quantum state tomography (projections along x and y with a $\pi/2$ -pulse along the corresponding axis and projection along z).

Furthermore, care should be taken that in general, while applying the first RF pulse (which rotates the nuclear spin by an angle Φ conditioned on the electron being in $|m_s = -1\rangle$), the nuclear spin in the electron $m_s = 0$ manifold will undergo free-evolution, acquiring an additional phase shift proportional to the temporal length of the pulse (therefore to Φ). Therefore, we need to characterize this phase offset for all situations different from a $\pi/2$ -pulse. This was done by fixing τ and sweeping the phase of RF-2 for different value of the length of the RF-1 pulse (T_{RF-1}). After fitting the resulting sinusoidal oscillation, we retrieved the extra phase offset $\varphi_2(\Phi)$ to RF-2 such that it is applied in the correct rotating frame.

3.6.5 Partial measurements with controlled strength: Theory

The protocol starts by initializing the nucleus in $|\psi_N\rangle = \frac{1}{\sqrt{2}}(|\downarrow\downarrow\rangle + |\uparrow\uparrow\rangle)$ and the electron in $|\psi_e\rangle = |0\rangle$.

The tunable-entangling gate consists of three steps. First, a $\pi/2$ -pulse is applied around x to

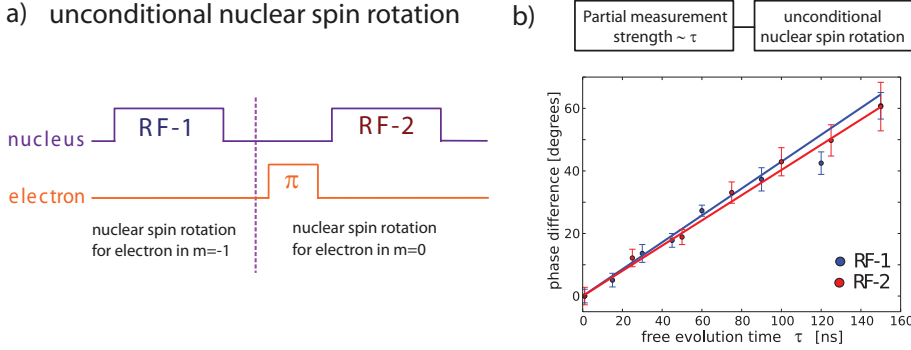


Figure 3.10 |On the left, pulse sequence for unconditional nuclear spin rotation. On the right, phase of the nuclear spin as a function of the free evolution time τ , for the two electron-spin manifolds ($m_S = -1$ and $m_S = 0$).

the electron spin, creating the equal superposition state:

$$|\psi\rangle = \frac{1}{2} (|0\rangle - i|1\rangle) (|\Downarrow\rangle + |\Uparrow\rangle) \quad (3.5)$$

Then the system undergoes free evolution of a variable time τ (according to the Hamiltonian in Eq. 3.4):

$$|\psi\rangle = \frac{1}{2} \left\{ e^{0i} |0, \Downarrow\rangle + e^{-iA\tau} |0, \Uparrow\rangle - ie^{-iA\tau/2} |1, \Downarrow\rangle - ie^{-iA\tau/2} |1, \Uparrow\rangle \right\} \quad (3.6)$$

A second electron $\pi/2$ -pulse, now around y , creates the state:

$$|\psi\rangle = \frac{1}{2} \left\{ |0\rangle \left[\beta_+(\tau) |\Downarrow\rangle + ie^{iA\tau/4} \beta_-(\tau) |\Uparrow\rangle \right] + e^{i\pi/2} |1\rangle \left[\beta_-(\tau) |\Downarrow\rangle + ie^{iA\tau/4} \beta_+(\tau) |\Uparrow\rangle \right] \right\} \quad (3.7)$$

where $\beta_{\pm} = \cos(\pi/4 \pm A\tau/4)$. We define θ as $\theta = A\tau/2$, and the measurement strength as $\sin \theta$.

For $\theta = 0$ ($\tau = 0$), the electron and nuclear spins are in a separable state:

$$|\psi(\tau = 0)\rangle = \frac{1}{2} (|0\rangle + i|1\rangle) (|\Downarrow\rangle + i|\Uparrow\rangle) \quad (3.8)$$

and a measurement of the electron spin gives no information about the state of the nuclear spin. On the other hand, for $\theta = 90$ degrees (corresponding to $\tau = \pi/A = 229$ ns), the electron and nuclear spins are in a maximally-entangled state:

$$|\psi(\tau = \pi/A)\rangle = \frac{1}{\sqrt{2}} [|0, \Uparrow\rangle - i|1, \Downarrow\rangle] \quad (3.9)$$

and a measurement of the electron spin results in a projective measurement of the nuclear spin. Performing the electron-spin read-out by resonantly exciting the E_y optical transition (therefore probing the population of the $|m_s = 0\rangle$ state) we project the nuclear spin on the $|m_I = -1\rangle$ ($|\uparrow\rangle$) state when a photon is detected and on the $|m_I = 0\rangle$ ($|\downarrow\rangle$) state when no photon is detected.

In the intermediate cases, $0 < \tau < \pi/A$, the concurrence of the state as a function of τ is given by:

$$C(\tau) = \sin \theta = \sin(A\tau/2) \quad (3.10)$$

if $|\psi_N\rangle$ is initialized in $|x\rangle$. The value of C corresponds to the strength of the measurement performed on the system qubit.

Note from Eq. 3.7 that a τ -dependent phase shift $\varphi = +A\tau/4$, unconditional on the electron spin, is imposed on the nuclear spin state after the measurement, as a result of the variable free evolution time. We compensate by adjusting the phase of the final RF pulse (see Section 3.6.4 for details).

The nuclear spin density matrix, unconditioned on the result of the electron spin measurement, can be derived by tracing over the electron spin, resulting in:

$$\rho_{uncond} = \frac{1}{2} \begin{bmatrix} 1 & \cos^2(A\tau/2) \\ \cos^2(A\tau/2) & 1 \end{bmatrix} \quad (3.11)$$

Increasing the measurement strength, the initial pure state becomes increasingly mixed, resulting in a completely mixed state for $\theta = 90$ degrees.

Conditioning on measuring the electron spin in the state $|0\rangle$, the nuclear spin state is:

$$\rho_0 = \frac{1}{2} \begin{bmatrix} 1 + \sin(A\tau/2) & \cos^2(A\tau/2) \\ \cos^2(A\tau/2) & 1 - \sin(A\tau/2) \end{bmatrix} \quad (3.12)$$

Now, the resulting state remains pure, but it is increasingly rotated towards $|\uparrow\rangle$ for increasing measurement strength.

3.6.6 Characterization of the partial measurements

The partial measurement was characterized by performing quantum state tomography, as explained in the main text. In Fig 3.11, we plot the elements of the density matrix of the nuclear spin after the partial measurement as a function of the measurement strength, for three different input states $\{| \uparrow \rangle, |x\rangle, |y\rangle\}$. On the upper row we do not take the measurement outcome of the electron into account, while on the lower row we show the data conditioned on the detection of a photon (ancilla projected to $|0\rangle$).

When we condition on a measurement result for the ancilla, the operation on the system qubit is a projection with increasing strength (completely projective along z for measurement strength 1). In the unconditioned case, we observe measurement-induced dephasing.

We characterized the collapse process by quantum process tomography³⁶. Results are plotted in Fig. 3.12. On the upper row, the process matrix for the unconditioned case

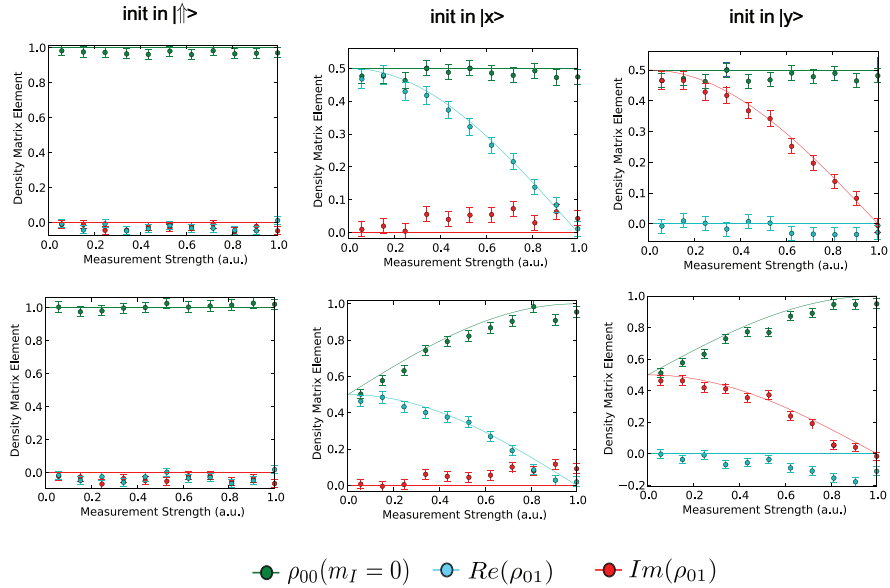


Figure 3.11 |Density matrix elements of the states after a partial measurement, as a function of the measurement strength, for three different input states. On the upper row, data not taking the electron spin readout into account. On the lower row, data conditioned on detection of a photon (electron spin projected to $m_s = 0$). Solid lines represent theoretical prediction from Eq. 3.11 and Eq. 3.12

shows a continuous transition from the identity process to a collapse process consisting of equal contributions of $\hat{1}$ and $\hat{\sigma}_z$: the absence of off-diagonal terms represents the increasing dephasing. The theoretical process matrix for the unconditioned case is:

$$\hat{\chi}_{uncond} = \frac{1}{2} \begin{bmatrix} 1 + \cos \theta & 0 & 0 & 0 \\ 0 & 0 & 0 & 0 \\ 0 & 0 & 0 & 0 \\ 0 & 0 & 0 & 1 - \cos \theta \end{bmatrix} \quad (3.13)$$

On the bottom row, we plot the process conditioned on the measurement result of the electron spin: this is a non-trace-preserving process, with state-dependent success probability³⁷. The theoretical process matrix as a function of θ is:

$$\hat{\chi}_{cond} = \frac{1}{2} \begin{bmatrix} 1 + \cos \theta & 0 & 0 & \sin \theta \\ 0 & 0 & 0 & 0 \\ 0 & 0 & 0 & 0 \\ \sin \theta & 0 & 0 & 1 - \cos \theta \end{bmatrix} \quad (3.14)$$

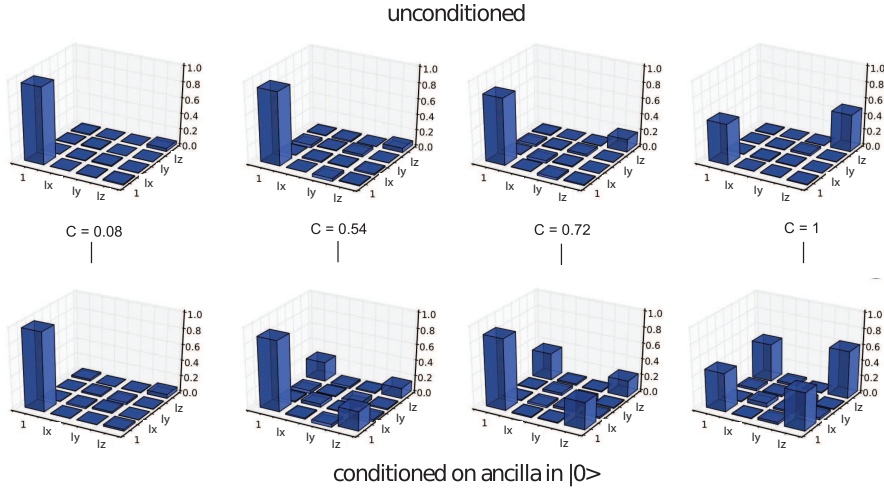


Figure 3.12 | Quantum process tomography for the tunable-strength measurement for different strength values (defined by the value of τ and the corresponding values for $\theta = A\tau/2$ and measurement strength $C = \sin \theta$). On the upper row, the real part of the process matrix for the unconditioned case. On the lower row, the process matrix conditioned on a measurement of the ancilla giving the result $|0\rangle$.

In this case, the process is coherent and the off-diagonal terms are, in general, non-zero. The fidelity between the ideal process matrix and our experimentally reconstructed one is plotted in Fig. 3.13.

3.6.7 Weak value and conditioned average

Given an observable \mathcal{I} , the weak value of the associated quantum operator \hat{I} , as introduced by Aharonov, Albert and Vaidman^{8,38}, is defined by

$$I_W = \frac{\langle \psi_f | \hat{I} | \psi_i \rangle}{\langle \psi_f | \psi_i \rangle} \quad (3.15)$$

This quantity does not depend on the context of the specific measurement, but only on the operator \hat{A} and on the initial and final states (respectively $|\psi_i\rangle$ and $|\psi_f\rangle$). For a qubit, with initial state $|\psi_i\rangle = |x\rangle$ and final state $|\psi_f\rangle = \cos \phi |0\rangle + \sin \phi |1\rangle$, we have $(S_z)_w = \cos 2\phi / (1 + \sin 2\phi)$.

Given an observable \mathcal{A} , one can measure it with a series of operators, which can be projectors $\{\hat{\Pi}_k, \hat{\Pi}_k^2 = \hat{\Pi}_k\}$ or, more generally, POVMs $\{\hat{E}_j = \hat{M}_j^\dagger \hat{M}_j\}$. The associated measurement outcomes are, respectively, the eigenvalues $\{a_k\}$ and the generalized eigenvalues (or contextual values) $\{\alpha_j\}$ ³⁹, such that the spectral decomposition of the operator \hat{I} can be written

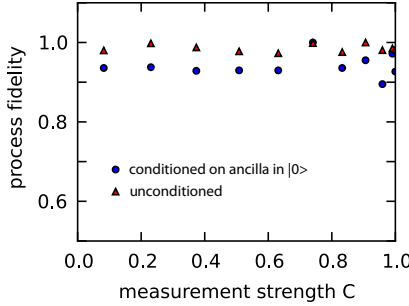


Figure 3.13 | Fidelity of the reconstructed quantum process matrices χ_{cond} and χ_{uncond} , as a function of the measurement strength ($C = \sin \theta$). The fidelity is calculated with the formula:

$$F(\chi_{exp}, \chi_{th}) = \text{Tr} \left\{ \sqrt{\sqrt{\chi_{exp}} \chi_{th} \sqrt{\chi_{exp}}} \right\}^2 {}^{37}.$$

as:

$$\hat{I} = \sum_j \alpha_j \hat{E}_j = \sum_k a_k \hat{\Pi}_k \quad (3.16)$$

Consider now a sequence of two measurements, \mathcal{M}_1 and \mathcal{M}_2 and suppose to condition the average of the result of \mathcal{M}_1 to a measurement result for \mathcal{M}_2 . The generalized weak value (or conditioned average) of the observable is defined as:

$${}_f \langle I \rangle = \sum_j \alpha_j^{(1)} P(j|f) \quad (3.17)$$

where $\{\alpha_j^{(1)}\}$ are the possible measurement outcomes of \mathcal{M}_1 (generalized eigenvalues) and $P(j|f) = p_{jf}/(\sum_j p_{jf})$ is the conditional probability to detect the outcome $\alpha_j^{(1)}$ in the first measurement, given the outcome $\alpha_f^{(2)}$ for the second measurement.

Unlike the weak value, the conditioned average encodes information not only about the observable \mathcal{A} , but also on the specific measurement context. However, it can be shown³⁹ that, under certain conditions (namely minimal state disturbance), the dependence on the measurement vanishes. For a pure initial state, a pure POVM and a projective final measurement, it reduces to the weak value of Eq. 3.15 .

In our case, for a measurement operator $\hat{E}_j = (1/2)(\hat{1} \pm \sin \theta \hat{I}_z)$, the generalized eigenvalues are $\pm 1/\sin \theta$ and the conditional average is:

$${}_f \langle I_z \rangle = \frac{1}{\sin \theta} \frac{p_{00} - p_{10}}{p_{00} + p_{10}} = \frac{\cos 2\phi}{1 + \cos \theta \sin 2\phi} \quad (3.18)$$

This quantity reduces to the quantum weak value for $\sin \theta = 0$ and does not diverge for finite measurement strength. Note that from this expression^{7,26}, it is possible to observe values

lying outside the range of the operator eigenvalues for any finite measurement strength.

3.6.8 Experimental quantum weak value for a spin qubit

A measurement of the conditional average $f \langle I_z \rangle$ is performed with the pulse sequence shown in Fig. 3.1a of the main text, starting from the initial state $|x\rangle = (1/\sqrt{2})(|\Downarrow\rangle + |\Uparrow\rangle)$. The scheme consists of a partial measurement (strength θ) followed by a projective measurement in a rotated basis (angle ϕ), post-selecting on the result of the projective measurement. In the first set of measurements (large panel in Fig. 3.2d of the main text) we fix the strength of the first measurement and sweep the basis rotation angle ϕ before the projective measurement. For the inset of Fig. 3.2d of the main text we sweep the measurement strength θ and choose ϕ to yield the maximum weak value.

We post-select on the measurement outcome $|0\rangle$ for the ancilla read-out (system in $|\Uparrow\rangle$), corresponding to the detection of a photon (electron spin in $m_s = 0$).

The conditional average can be calculated with the expression in Eq. 3.18 where p_{ij} is the probability of outcome i for the ancilla read-out of the partial measurement and measurement outcome j for the ancilla read-out of the projective measurement (assuming perfect readout). From Eq. 3.7, we calculate the dependence of p_{ij} on ϕ and θ :

$$\begin{aligned} p_{11} &= \frac{1}{2} [\beta_-(\theta) \cos \phi + \beta_+(\theta) \sin \phi]^2 \\ p_{10} &= \frac{1}{2} [\beta_-(\theta) \sin \phi - \beta_+(\theta) \cos \phi]^2 \\ p_{01} &= \frac{1}{2} [\beta_-(\theta) \sin \phi + \beta_+(\theta) \cos \phi]^2 \\ p_{00} &= \frac{1}{2} [\beta_-(\theta) \cos \phi - \beta_+(\theta) \sin \phi]^2 \end{aligned} \quad (3.19)$$

where $\beta_{\pm}(\theta) = \cos(\pi/4 \pm \theta/2)$.

Since our read-out is not perfect, it must be calibrated to take into account the finite detection efficiency and the dark counts. For the state $m_s = 0$ we are limited by our detection efficiency ($\sim .80$), while for the $m_s = -1$ read-out we suffer from dark counts. We define F_i as the fidelity of the $m_s = 0$ read-out and G_i as the read-out fidelity for $m_s = -1$, in the i -th measurement. Then, given the ideal probabilities p_{ij} , the measured fractions n_{ij} are:

$$\begin{bmatrix} n_{11} \\ n_{10} \\ n_{01} \\ n_{00} \end{bmatrix} = \begin{bmatrix} G_1 G_2 & G_1(1-F_2) & (1-F_1)G_2 & (1-F_1)(1-F_2) \\ G_1(1-G_2) & G_1 F_2 & (1-F_1)(1-G_2) & F_2(1-F_1) \\ (1-G_1)G_2 & (1-G_1)(1-F_2) & F_1 G_2 & F_1(1-F_2) \\ (1-G_1)(1-G_2) & (1-G_1)F_2 & F_1(1-G_2) & F_1 F_2 \end{bmatrix} \begin{bmatrix} p_{11} \\ p_{10} \\ p_{01} \\ p_{00} \end{bmatrix} \quad (3.20)$$

The theoretical curve in Fig. 3.2d of the main text is calculated without fit-parameters, using the read-out correction of Eq. 3.20 and assuming an asymmetric spin-flip rate $f = 0.02$

between the first and second read-out. This spin-flip probability arises during the reset of the ancilla by optically exciting the forbidden transition of E_y . The value f is determined from independent measurements.

3.6.9 Partial measurements as probabilistic rotations

Starting from the state $|\psi_{init}\rangle = \cos \theta_i |\Downarrow\rangle + \sin \theta_i |\Uparrow\rangle$, we perform a partial measurement with strength θ_m . With probability $\cos^2 \theta$, we obtain the state:

$$|\psi_0\rangle = \frac{1}{\mathcal{N}_0} [\cos(\pi/4 + \theta_m/2) \cos \theta_i |\Downarrow\rangle + \cos(\pi/4 - \theta_m/2) \sin \theta_i |\Uparrow\rangle] \quad (3.21)$$

where $1/\mathcal{N}_0$ is the normalization factor. The state, initially at an angle θ_i , is rotated to the angle:

$$\theta_0 = \arctan \left[\tan \theta_i \frac{\cos \theta_m}{1 - \sin \theta_m} \right] \quad (3.22)$$

On the other hand, with probability $p_{succ} = \sin^2 \theta$, the measurement leads to the state:

$$|\psi_1\rangle = \frac{1}{\mathcal{N}_1} [\cos(\pi/4 - \theta_m/2) \cos \theta_i |\Downarrow\rangle + \cos(\pi/4 + \theta_m/2) \sin \theta_i |\Uparrow\rangle] \quad (3.23)$$

Therefore, the initial state rotated to the angle:

$$\theta_1 = \arctan \left[\tan \theta_i \frac{1 - \sin \theta_m}{\cos \theta_m} \right] \quad (3.24)$$

In other words, as shown in³¹, a partial measurement is equivalent to a probabilistic state rotation, with a rotation angle which depends on the strength of the measurement and on the initial state (see Fig. 3.14).

3.6.10 Heralded sequential measurements: un-collapse and steering

In Fig. 3.15, we implement two heralded sequential partial measurements. We post-select on the case of photon detection, using short read-out times to minimize electron spin-flips, at the price of reduced success probabilities. We can do this with high fidelity, maintaining a good coherence of the state after two measurements. No spin-pumping between the two measurements is performed, in order to avoid electron spin-flips that would destroy nuclear-spin coherence.

We first perform a measurement with strength $\theta_1 = 20$ degrees, followed by a measurement with the same strength but projecting on the opposite electron state (equivalent to a measurement with strength $\theta_2 = -20$ degrees). This brings us back to the original quantum state, in a probabilistic un-collapse of the state. This technique has been used to probabilistically recover a state subject to amplitude-damping decoherence⁴⁰⁻⁴².

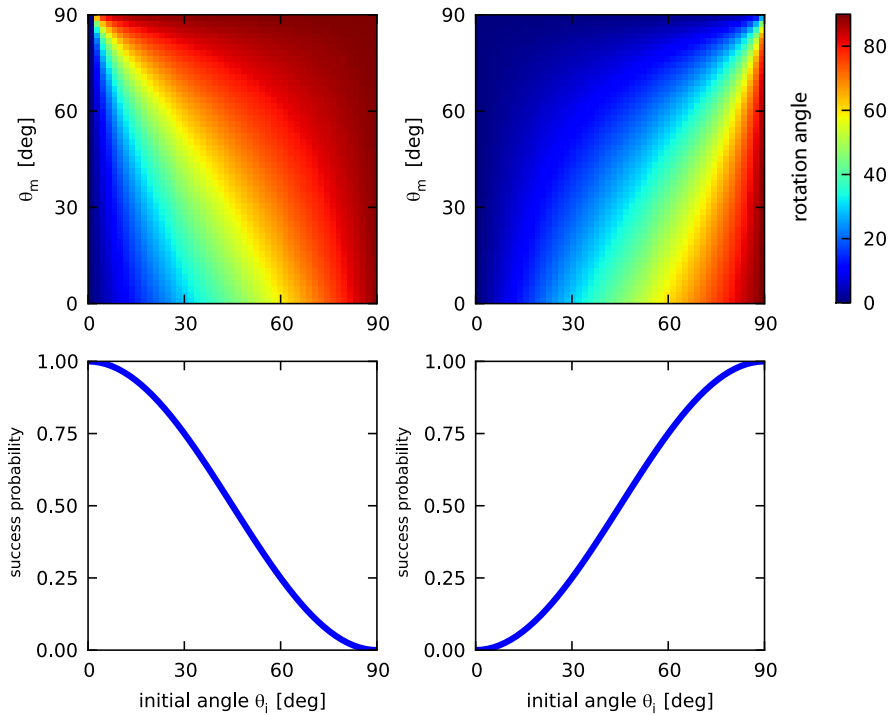


Figure 3.14 |A partial measurement is equivalent to a probabilistic rotation. Given a an initial superposition with angle θ_i ($|\psi_{init}\rangle = \cos \theta_i |\downarrow\rangle + \sin \theta_i |\uparrow\rangle$) and a partial measurement with strength θ_m , one gets the rotation angle plotted on the upper left subplot in case the electron spin is measured to be in $|0\rangle$ (probability $\cos^2 \theta_i$, plot on the bottom left) or the rotation angle plotted on the upper right in case the electron spin is measured to be in $|1\rangle$ (probability $\sin^2 \theta_i$, plot on the bottom right)

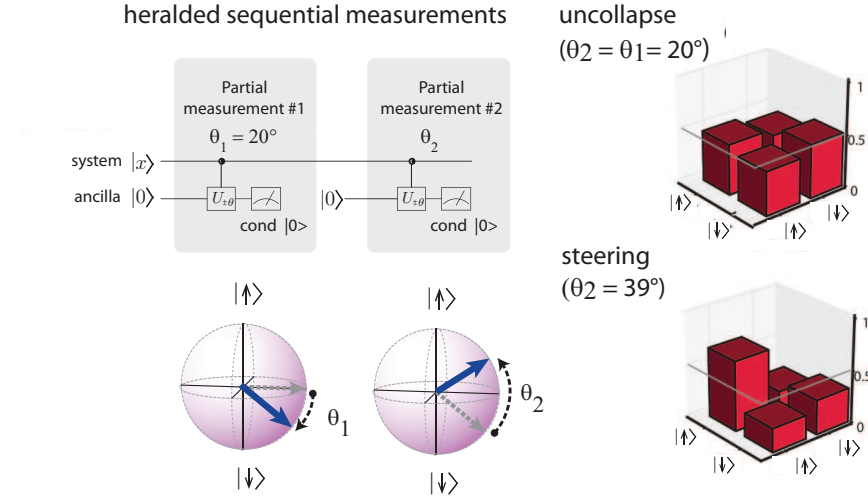


Figure 3.15 | Two sequential heralded partial measurements, both post-selected on the case of photon detection. The density matrices are the result of state tomography, performed after the two partial measurements. For the uncollapse (upper density matrix), first a measurement with strength $C = 0.34$ ($\theta_1 = 20$ degrees) is performed, after which the initial state is restored by a second measurement with $\theta_2 = -20$ degrees. For the lower density matrix, the second measurement is set to $\theta_2 = 39$ degrees, such that the system, that was projected towards $|\downarrow\rangle$ after the first measurements, is steered towards $|\uparrow\rangle$ through the backaction of the second measurement.

In general, a partial quantum measurement is equivalent to a probabilistic rotation. For $\theta_1 = \theta_2 = +20$ degrees, two successive measurements result in a combined rotation of 39 degrees, with success probability 0.16. In our case, heralding on photon detection, this can be done quite effectively (fidelity 0.78).

3.7 State steering by real-time adaptive measurements

3.7.1 Ideal protocol

We start in the state $|\psi_0\rangle = |x\rangle = (1/\sqrt{2})(|\downarrow\rangle + |\uparrow\rangle)$, with the goal to reach a target state $|\psi_T\rangle = \cos\theta_T|\downarrow\rangle + \sin\theta_T|\uparrow\rangle$.

First, we do a measurement with strength $\theta_1 = \pi/2 - 2\theta_T$. With probability 0.5 the system reaches the target state, while in the rest of the cases it is shifted in the opposite direction, to the state:

$$|\psi_1\rangle = \cos\left(\frac{\pi}{4} - \frac{\theta_1}{2}\right)|\downarrow\rangle + \cos\left(\frac{\pi}{4} + \frac{\theta_1}{2}\right)|\uparrow\rangle \quad (3.25)$$

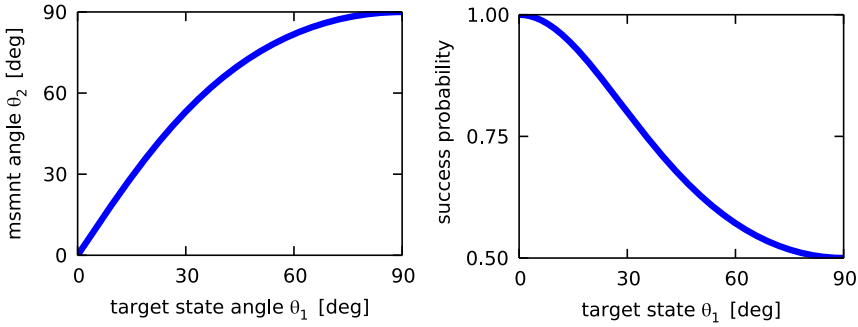


Figure 3.16 |On the left, strength of the second measurement, as a function of the desired target state. On the right, success probability of the two-step algorithm.

In order to try to steer it back, we perform a second measurement, with strength θ_2 . In case of success, we get the state:

$$|\psi_{10}\rangle = \frac{1}{\mathcal{N}} \left[\cos\left(\frac{\pi}{4} - \frac{\theta_1}{2}\right) \cos\left(\frac{\pi}{4} + \frac{\theta_2}{2}\right) |\downarrow\rangle + \cos\left(\frac{\pi}{4} + \frac{\theta_1}{2}\right) \cos\left(\frac{\pi}{4} - \frac{\theta_2}{2}\right) |\uparrow\rangle \right] \quad (3.26)$$

where $\mathcal{N} = [\cos^2\left(\frac{\pi}{4} - \frac{\theta_1}{2}\right) \cos^2\left(\frac{\pi}{4} + \frac{\theta_2}{2}\right) + \cos^2\left(\frac{\pi}{4} + \frac{\theta_1}{2}\right) \cos^2\left(\frac{\pi}{4} - \frac{\theta_2}{2}\right)]^{1/2}$. The system can be steered to target state, by setting:

$$\frac{1}{\mathcal{N}} \cos\left(\frac{\pi}{4} - \frac{\theta_1}{2}\right) \cos\left(\frac{\pi}{4} + \frac{\theta_2}{2}\right) = \cos\left(\frac{\pi}{4} + \frac{\theta_1}{2}\right) \quad (3.27)$$

After simplification, this leads to the equation:

$$(1 + \sin \theta_1)(1 - \sin \theta_2) = (1 - \sin \theta_1)(1 - \sin \theta_1 \sin \theta_2) \quad (3.28)$$

Solving for θ_2 , we find that the strength of the second measurement can be tuned as:

$$\theta_2 = \sin^{-1} \left[2 \frac{\sin \theta_1}{1 + \sin^2 \theta_1} \right] \quad (3.29)$$

The probability to steer the state to the desired target, after two measurements, is:

$$p_{\text{success}} = \frac{1 + \cos \theta_1}{2} \quad (3.30)$$

3.7.2 Error analysis

The protocol described in the last Section assumes ideal measurements. In practice, however, we are subject to several non-ideal conditions¹⁵:

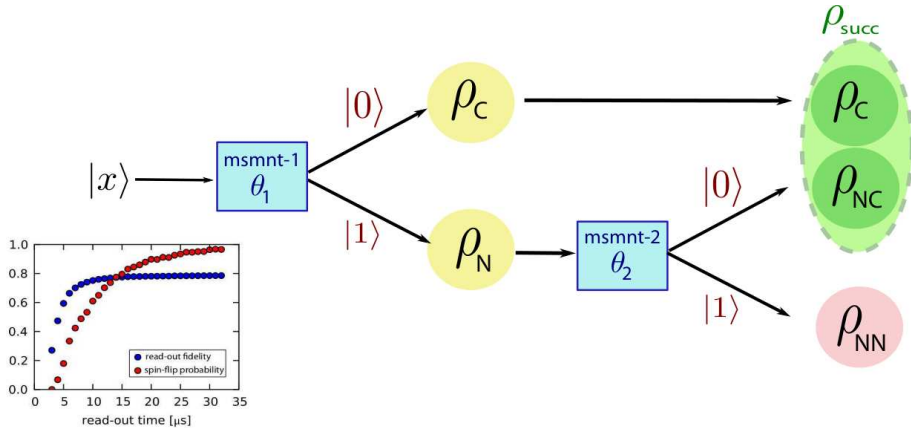


Figure 3.17 |Description of the adaptive scheme. Ancilla readout $|0\rangle$ corresponds to the detection of a photon when optically exciting the E_y transition, while no photon detection corresponds to ancilla projection to $|1\rangle$. Inset: experimental data for electron spin read-out fidelity F_0 and spin-flip probability q as a function of read-out time.

- the electron-spin read-out is not perfect. Given that the electron is in $m_s = 0$, if we excite the E_y transition, we are supposed to detect photons. However, such photons are detected with a finite efficiency (due to losses in the diamond, the collection optics and the finite efficiency of the detector). This results in a read-out fidelity $F_0 < 1$. In the first measurement, this leads us to make the wrong decision and apply a correction although we had already reached the target state.
- due to dark counts, we detect photon clicks even in the absence of photons. This probability is quite small, so we neglect it in the following analysis
- during electron read-out, there is a probability (q) that the electron spin flips. This results in dephasing of the nuclear spin. Moreover, with a small probability it results also in a nuclear spin-flip (we measured the probability to get a nuclear spin-flip as a result of an electron spin-flip to be around 0.02). We neglect the nuclear spin flip and just consider the effect of dephasing.

The read-out efficiency and spin-flip probability are not independent: the longer the read-out, the higher the detection efficiency, but, at the same time, the electron spin-flip probability is also increased. The read-out fidelity F_0 and the electron spin-flip probability q , as a function of read-out time, are shown in the inset of Fig. 3.17. The best trade-off is for a read-out time $T \sim 5\mu\text{s}$, where $F_0 \sim 0.6$ and $q \sim 0.2$.

3.8 Bibliography

- [1] C. Guerlin *et al.* Progressive field-state collapse and quantum non-demolition photon counting. *Nature* **448**, 889 (2007).
- [2] M. Hatridge *et al.* Quantum Back-Action of an Individual Variable-Strength Measurement. *Science* **339**, 178 (2013).
- [3] K. W. Murch, S. J. Weber, C. Macklin and I. Siddiqi. Observing single quantum trajectories of a superconducting quantum bit. *Nature* **502**, 211 (2013).
- [4] S. Ashhab and F. Nori. Control-free control: Manipulating a quantum system using only a limited set of measurements. *Physical Review A* **82**, 062103 (2010).
- [5] H. Wiseman. Quantum control: Squinting at quantum systems. *Nature* **470**, 178 (2011).
- [6] T. Brun, L. Diósi and W. Strunz. Test of weak measurement on a two- or three-qubit computer. *Physical Review A* **77**, 032101 (2008).
- [7] J. Groen *et al.* Partial-Measurement Backaction and Nonclassical Weak Values in a Superconducting Circuit. *Physical Review Letters* **111**, 090506 (2013).
- [8] Y. Aharonov, D. Z. Albert and L. Vaidman. How the result of a measurement of a component of the spin of a spin-1/2 particle can turn out to be 100. *Physical Review Letters* **60**, 1351 (1988).
- [9] G. Pryde, J. O'Brien, A. White, T. Ralph and H. Wiseman. Measurement of Quantum Weak Values of Photon Polarization. *Physical Review Letters* **94**, 220405 (2005).
- [10] J. Dressel, M. Malik, F. M. Miatto, A. N. Jordan and R. W. Boyd. Understanding Quantum Weak Values: Basics and Applications. Preprint at <http://arxiv.org/abs/1305.7154> (2013).
- [11] P. Cappellaro. Spin-bath narrowing with adaptive parameter estimation. *Physical Review A* **030301(R)**–5 (2012).
- [12] B. L. Higgins, D. W. Berry, S. D. Bartlett, H. M. Wiseman and G. J. Pryde. Entanglement-free Heisenberg-limited phase estimation. *Nature* **450**, 393 (2007).
- [13] R. Raussendorf and H. Briegel. A one-way quantum computer. *Physical Review Letters* **86**, 5188 (2001).
- [14] R. Prevedel *et al.* High-speed linear optics quantum computing using active feed-forward. *Nature* **445**, 65 (2007).
- [15] L. Robledo *et al.* High-fidelity projective read-out of a solid-state spin quantum register. *Nature* **477**, 574 (2011).

- [16] D. Ristè, J. G. van Leeuwen, H.-S. Ku, K. W. Lehnert and L. DiCarlo. Initialization by measurement of a superconducting quantum bit circuit. *Physical Review Letters* **109**, 050507 (2012).
- [17] C. W. Chou *et al.* Measurement-induced entanglement for excitation stored in remote atomic ensembles. *Nature* **438**, 828 (2005).
- [18] D. L. Moehring *et al.* Entanglement of single-atom quantum bits at a distance. *Nature* **449**, 68 (2007).
- [19] W. Pfaff *et al.* Demonstration of entanglement-by-measurement of solid-state qubits. *Nature Physics* 29–33 (2012).
- [20] D. Ristè *et al.* Deterministic entanglement of superconducting qubits by parity measurement and feedback. *Nature* **502**, 350 (2013).
- [21] J. Chiaverini *et al.* Realization of quantum error correction. *Nature* **432**, 602 (2004).
- [22] G. G. Gillett *et al.* Experimental Feedback Control of Quantum Systems Using Weak Measurements. *Physical Review Letters* **104**, 080503 (2010).
- [23] C. Sayrin *et al.* Real-time quantum feedback prepares and stabilizes photon number states. *Nature* **477**, 73 (2011).
- [24] R. Vijay *et al.* Stabilizing Rabi oscillations in a superconducting qubit using quantum feedback. *Nature* **490**, 77 (2012).
- [25] J. Dressel, S. Agarwal and A. N. Jordan. Contextual values of observables in quantum measurements. *Physical Review Letters* **104**, 240401 (2010).
- [26] N. S. Williams and A. N. Jordan. Weak values and the Leggett-Garg inequality in solid-state qubits. *Physical Review Letters* **100**, 026804 (2008).
- [27] L. Jiang *et al.* Coherence of an Optically Illuminated Single Nuclear Spin Qubit. *Physical Review Letters* **100**, 073001 (2008).
- [28] N. Zhao *et al.* Sensing single remote nuclear spins. *Nature nanotechnology* **7**, 657 (2012).
- [29] T. Taminiau *et al.* Detection and Control of Individual Nuclear Spins Using a Weakly Coupled Electron Spin. *Physical Review Letters* **109**, 137602 (2012).
- [30] S. Kolkowitz, Q. P. Unterreithmeier, S. D. Bennett and M. D. Lukin. Sensing distant nuclear spins with a single electron spin. *Physical Review Letters* **109**, 137601 (2012).
- [31] A. N. Jordan and A. N. Korotkov. Qubit feedback and control with kicked quantum nondemolition measurements: A Bayesian approach. *Phys. Rev. B* **74**, 085307 (2006).
- [32] H. Bernien *et al.* Heralded entanglement between solid-state qubits separated by three metres. *Nature* **497**, 86 (2013).

- [33] F. Dolde *et al.* Room-temperature entanglement between single defect spins in diamond. *Nature Physics* **139**–143 (2013).
- [34] C. P. Slichter. *Principles of Magnetic Resonance*. Springer Science & Business Media (1996).
- [35] H. K. Cummins, G. Llewellyn and J. A. Jones. Tackling systematic errors in quantum logic gates with composite rotations. *Phys. Rev. A* **67**, 42308 (2003).
- [36] M. A. Nielsen and I. L. Chuang. *Quantum Computation and Quantum Information*. Cambridge University Press (2000).
- [37] I. Bongioanni, L. Sansoni, F. Sciarrino, G. Vallone and P. Mataloni. Experimental quantum process tomography of non-trace-preserving maps. *Phys. Rev. A* **82**, 042307 (2010).
- [38] A. G. Kofman, S. Ashhab and F. Nori. Nonperturbative theory of weak pre- and post-selected measurements. *Physics Reports* **520**, 43 (2012).
- [39] J. Dressel, S. Agarwal and A. N. Jordan. Contextual values of observables in quantum measurements. *Phys. Rev. Lett.* **104**, 240401 (2010).
- [40] M. Koashi and M. Ueda. Reversing measurement and probabilistic quantum error correction. *Phys. Rev. Lett.* **82**, 2598 (1999).
- [41] A. N. Korotkov and A. N. Jordan. Undoing a weak quantum measurement of a solid-state qubit. *Phys. Rev. Lett.* **97**, 166805 (2006).
- [42] N. Katz *et al.* Reversal of the weak measurement of a quantum state in a superconducting phase qubit. *Phys. Rev. Lett.* **101**, 200401 (2008).

CHAPTER 4

OPTIMIZED QUANTUM SENSING WITH A SINGLE ELECTRON SPIN USING REAL-TIME ADAPTIVE MEASUREMENTS

C. Bonato*, M.S. Blok*, H.T. Dinani, D.W. Berry, M.L. Markham, D.J. Twitchen and
R. Hanson

Quantum sensors based on single solid-state spins promise a unique combination of sensitivity and spatial resolution^{1–20}. The key challenge in sensing is to achieve minimum estimation uncertainty within a given time and with a high dynamic range. Adaptive strategies have been proposed to achieve optimal performance but their implementation in solid-state systems has been hindered by the demanding experimental requirements. Here we realize adaptive d.c. sensing by combining single-shot readout of an electron spin in diamond with fast feedback. By adapting the spin readout basis in real time based on previous outcomes we demonstrate a sensitivity in Ramsey interferometry surpassing the standard measurement limit. Furthermore, we find by simulations and experiments that adaptive protocols offer a distinctive advantage over the best-known non-adaptive protocols when overhead and limited estimation time are taken into account. Using an optimized adaptive protocol we achieve a magnetic field sensitivity of $6.1 \pm 1.7 \text{ nT Hz}^{-\frac{1}{2}}$ over a wide range of 1.78 mT. These results open up a new class of experiments for solid-state sensors in which real-time knowledge of the measurement history is exploited to obtain optimal performance.

This chapter has been submitted to *Nature Nanotechnology* (2015).

* these authors contributed equally to this work

4.1 Introduction

Quantum sensors have the potential to achieve unprecedented sensitivity by exploiting control over individual quantum systems^{1,2}. As a prominent example, sensors based on single electron spins associated with Nitrogen-Vacancy (NV) centers in diamond capitalize on the spin's quantum coherence and the high spatial resolution resulting from the atomic-like electronic wave function^{3,4}. Pioneering experiments have already demonstrated single-spin sensing of magnetic fields^{5–7}, electric fields⁸, temperatures^{9,10} and strain¹¹. NV sensors may therefore have a revolutionary impact on biology^{12–15}, nanotechnology^{16–18} and material science^{19,20}.

4.2 D.C. Magnetometry

A spin-based magnetometer can sense a d.c. magnetic field B through the Zeeman shift $E_z = \hbar\gamma B = \hbar 2\pi f_B$ (γ is the gyromagnetic ratio and f_B the Larmor frequency) between two spin levels $|0\rangle$ and $|1\rangle$. In a Ramsey interferometry experiment, a superposition state $\frac{1}{\sqrt{2}}(|0\rangle + |1\rangle)$, prepared by a $\pi/2$ pulse, will evolve to $\frac{1}{\sqrt{2}}(|0\rangle + e^{i\varphi} |1\rangle)$ over a sensing time t . The phase $\varphi = 2\pi f_B t$ can be measured by reading out the spin in a suitable basis, by adjusting the phase ϑ of a second $\pi/2$ pulse.

For a Ramsey experiment that is repeated with constant sensing time t the uncertainty σ_{f_B} decreases with the total sensing time T as $1/(2\pi\sqrt{tT})$ (standard measurement sensitivity, SMS). However, the field range also decreases with t because the signal is periodic, creating ambiguity whenever $|2\pi f_B t| > \pi$. This results in a dynamic range bounded as $f_{B,max}/\sigma_{f_B} \leq \pi\sqrt{T/t}$. Recently, it was discovered that the use of multiple sensing times within an estimation sequence can yield a scaling of σ_{f_B} as $1/T$, resulting in a vastly improved dynamic range: $f_{B,max}/\sigma_{f_B} \leq \pi T/\tau_{min}$, where τ_{min} is the shortest sensing time used. A major open question is whether adaptive protocols, in which the readout basis is optimized in real time based on previous outcomes, can outperform non-adaptive protocols. While scaling beating the standard measurement limit has been reported with non-adaptive protocols^{21,22}, feedback techniques have only recently been demonstrated for solid-state quantum systems^{23–25} and adaptive sensing protocols have so far remained out of reach.

Here we implement adaptive d.c. sensing with a single-electron spin magnetometer in diamond by exploiting high-fidelity single-shot readout and fast feedback electronics (Fig. 4.1). We demonstrate a sensitivity beyond the standard measurement limit over a large field range. Furthermore, we investigate through experiments and simulations the performance of different adaptive protocols and compare these to the best known non-adaptive protocol. Although the non-adaptive protocol improves on the standard measurement limit for sequences with many detections we find that the adaptive protocols perform better when overhead time for initialization and readout is taken into account. In particular, the adaptive protocols require shorter sequences to reach the same sensitivity, thus allowing for sensing of signals that fluctuate on shorter timescales.

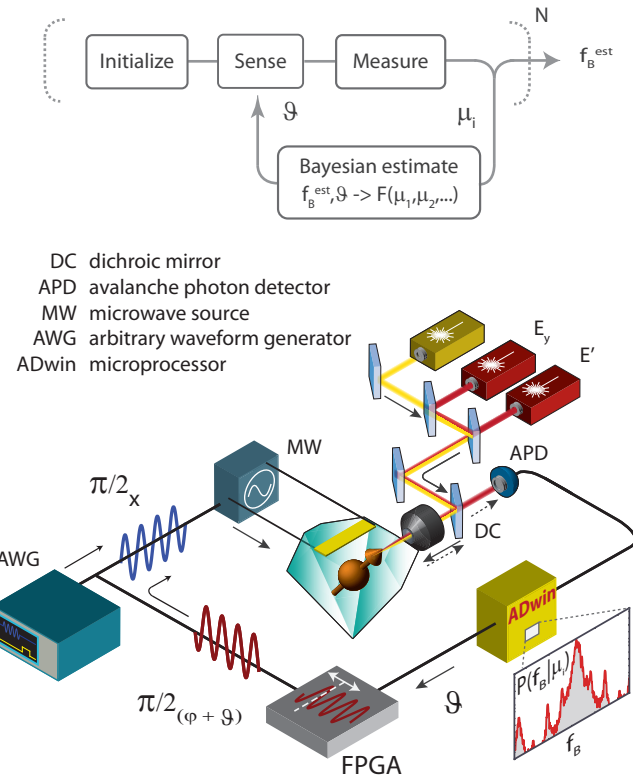


Figure 4.1 | Experiment concept and apparatus. The adaptive frequency estimation protocol consists of a sequence of initialization, sensing, measurement operations. After each measurement run, the outcome μ is used to update the estimate of the frequency f_B , which is then used to optimize the sensing parameters for the following run. Experimentally, the frequency estimation and adaptive calculation of the phase are performed in real-time by a microprocessor.

4. Optimized quantum sensing using real-time adaptive measurements

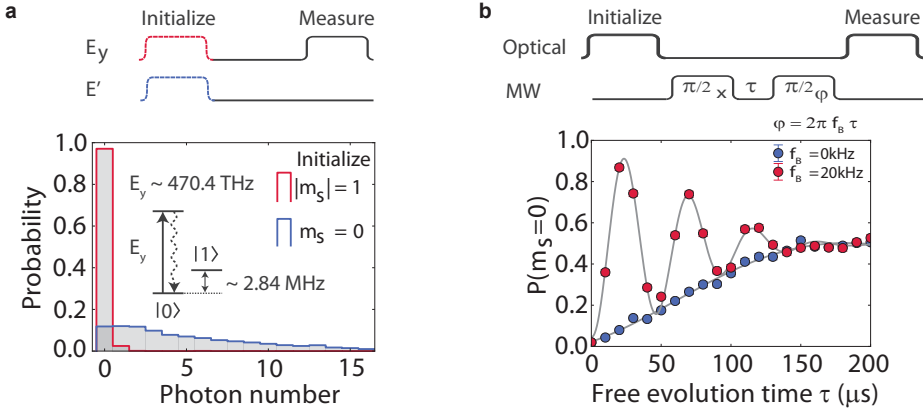


Figure 4.2 | Single shot readout and Ramsey. (a) The experiment is performed using the states $|0\rangle = |m_s = 0\rangle, |1\rangle = |m_s = -1\rangle$ of the electronic spin of a NV centre in diamond. The electronic spin is readout by resonant optical excitation and photon counting²⁶: detection of luminescence photons corresponds to detection of the $|0\rangle$ state. We plot the probability of detecting a photon after initializing either in $|0\rangle$ or $|1\rangle$. The readout fidelities for the states $|0\rangle$ (outcome 0) and $|1\rangle$ (outcome 1) are $F_0 = 0.88 \pm 0.02$, $F_1 = 0.98 \pm 0.02$, respectively. (b) Each measurement run consists of a Ramsey experiment, in which the phase accumulated over time by a spin superposition during free evolution is measured. The measurement basis rotation is controlled by the phase ϑ of the final $\pi/2$ -pulse. From the measured phase, we can extract the frequency f_B , corresponding to an energy shift between the levels $|0\rangle$ and $|1\rangle$ given by an external field (magnetic field, temperature, strain...). Here, to test the performance of different protocols, we set f_B as an artificial detuning, set by the microprocessor by adding $\varphi = 2\pi f_B t$ to the phase ϑ (see methods).

Our magnetometer employs two spin levels of a single NV center electron in isotopically purified diamond (0.01 % ^{13}C). We exploit resonant spin-selective optical excitation, at a temperature of 8 K, for high-fidelity initialization and single-shot readout²⁶ (Fig. 4.2a). Microwave pulses, applied via an on-chip stripline, coherently control the electron spin state. From Ramsey experiments, we measure a spin dephasing time of $T_2^* = (96 \pm 2)\mu\text{s}$ (Fig. 4.2b). In order to characterize the performance of different sensing protocols in a controlled setting, the effect of the external field is implemented as an artificial frequency detuning, by adding $\varphi = 2\pi f_B t$ to the phase ϑ of the final $\pi/2$ -pulse. To achieve high sensitivity in a wide field range we use an estimation sequence consisting of N different sensing times^{21,22,27,28}, varying as $\tau_n = 2^{(N-n)}\tau_{\min}$ ($n = 1..N$). The value of τ_{\min} sets the range; we take $\tau_{\min} = 20 \text{ ns}$, corresponding to a range $|f_B| < 25 \text{ MHz}$, equivalent to $|B| < 0.89 \text{ mT}$ for $\gamma = 2\pi \times 28 \text{ MHz mT}^{-1}$.

4.3 Adaptive frequency estimation protocol

The key idea of adaptive magnetometry is that for each Ramsey experiment the measurement basis is chosen based on the previous measurement outcomes such that the uncertainty in the frequency estimation is minimized (Fig. 4.1). After every Ramsey experiment, the outcome is used to update a frequency probability distribution $P(f_B)$ according to Bayes' rule, taking measured values for detection fidelity and coherence time into account (Methods). The current estimate of $P(f_B)$ is then used to calculate the phase ϑ of the final $\pi/2$ -pulse which allows for best discrimination between different possible magnetic field values in the next Ramsey experiment²⁸. In our experiment, this process is realized by a microprocessor, which receives the measurement outcome, performs the Bayesian estimate, calculates the phase ϑ and subsequently sends a digital signal to a field-programmable gate array (FPGA) to adjust the phase of the final $\pi/2$ -pulse accordingly (Fig. 4.1).

To reduce the undesired effects of quantum projection noise and imperfect readout fidelity we perform M_n Ramsey experiments²⁷ for each sensing time τ_n , with $M_n = G + F(n - 1)$. Here G and F can be chosen to optimize the performance of the protocol. For the short sensing times (large n), corresponding to the measurements that make the largest distinction in frequency (and where an error is therefore most detrimental), we perform the most Ramsey experiments. We will compare several protocols that differ in the strategy of adaptive phase choice. As a first example, we consider a protocol where the phase ϑ is adjusted each time the sensing time is changed; we name this “limited-adaptive” protocol.

An example of the working principles of the limited-adaptive protocol is illustrated in Fig. 4.3, for an estimation sequence comprising $N = 3$ sensing times and one measurement per sensing time ($G = 1, F = 0$). We start with no information over f_B , corresponding to a uniform probability density $P(f_B)$ (solid black line). For the first Ramsey experiment, the sensing time is set to $4\tau_{min}$. $P(f_B)$ is updated depending on the measurement outcome. For example, the outcome 1 indicates maximum probability for the values $f_B = \pm 6.25, \pm 18.75$ MHz, and minimum probability for $f_B = 0, \pm 12.5, \pm 25$ MHz. This indeterminacy in the estimation originates from the fact that, for this sensing time, the acquired phase spans the range $[-4\pi, 4\pi]$, wrapping multiple times around the $[-\pi, \pi]$ interval. The sensing time is then decreased to $2\tau_{min}$. Given the current $P(f_B)$ for outcome 1 (black curve), the filter functions that would be applied to $P(f_B)$ after the Bayesian update for detection outcomes 0 and 1 are represented, respectively, by the light red and blue areas. For $\vartheta = -/\pi/2$, maximum distinguishability is ensured: outcome 0 would select the peaks around $f_B = -6.25, +18.75$ MHz, while outcome 1 would select the peaks around $f_B = -18.75, +6.25$ MHz. The same process is then repeated, decreasing the sensing time to τ_{min} . The remaining uncertainty, corresponding to the width of the resulting peak in $P(f_B)$, is set by the longest sensing time $4\tau_{min}$.

Figure 4.4b shows the probability density yielded by experimental runs of the limited-adaptive protocol with different numbers of sensing times $N = 1, 3, 5, 7, 9$. Here, $f_B = 2$ MHz, and each estimation sequence is repeated 101 times, with $G = 5, F = 7$. For increasing N , the

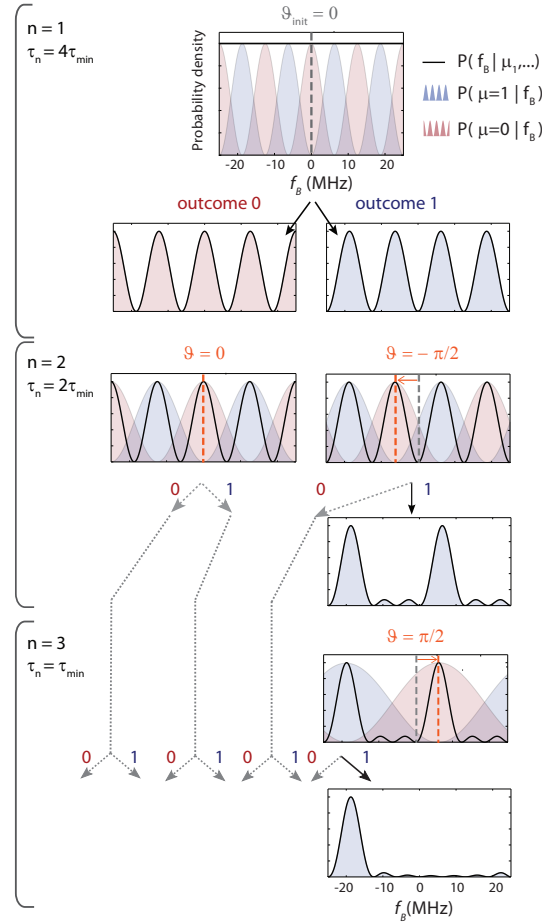


Figure 4.3 | High dynamic-range adaptive magnetometry. Limited-adaptive protocol, in the case of one Ramsey experiment per sensing time ($G = 1, F = 0$). In each step, the current frequency probability distribution $P(f_B)$ is plotted (solid black line), together with conditional probabilities $P(\mu|f_B)$ for the measurement outcomes $\mu = 0$ (red shaded area) and $\mu=1$ (blue shaded area). After each measurement, $P(f_B)$ is updated according to Bayes' rule. The detection phase ϑ of the Ramsey experiment is set to the angle which attains the best distinguishability between peaks in the current frequency probability distribution $P(f_B)$. Ultimately, the protocol converges to a single peak in the probability distribution, which delivers the frequency estimate.

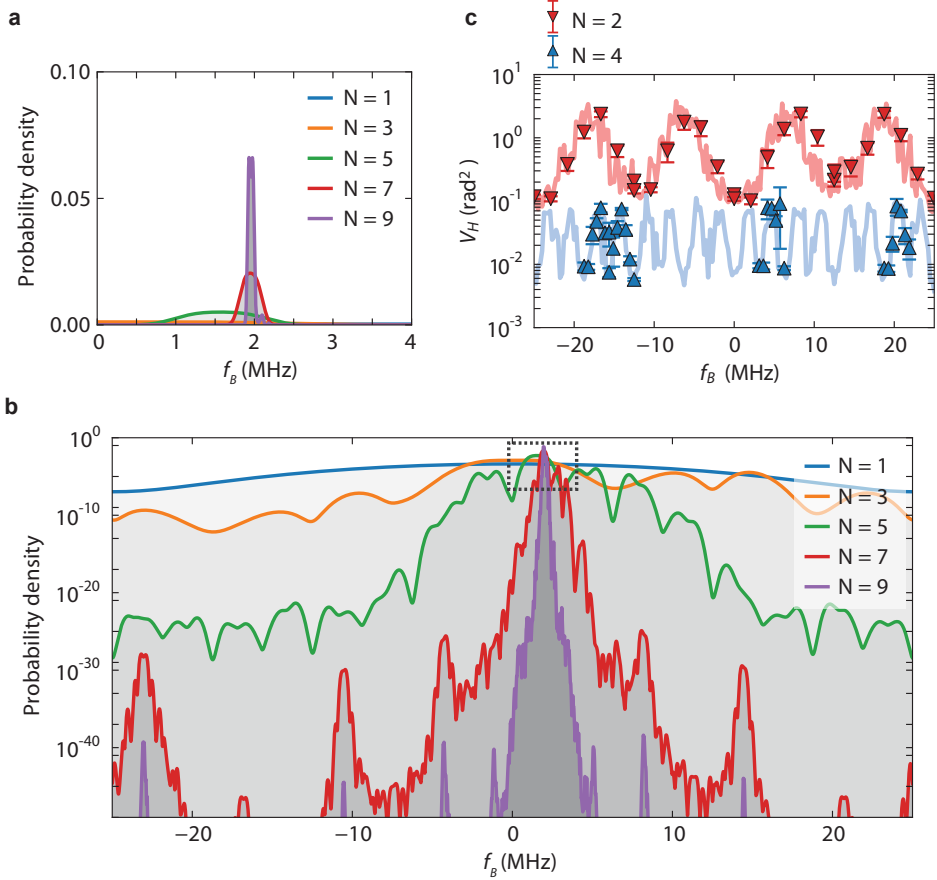


Figure 4.4 | Frequency dependence of uncertainty. (a)-(b) Frequency estimate example, for ($G = 5$, $F = 7$). We set a fixed artificial detuning $f_B = 2$ MHz and run different instances of the limited-adaptive frequency estimation protocol, with increasing N . The resulting probability density $P(f_B)$ is averaged over 101 repetitions. (c) Holevo variance as a function of the frequency f_B for $N = 2, 4$ (limited-adaptive protocol, $G = 5$, $F = 7$). We vary f_B by adjusting the phase of the final $\pi/2$ -pulse. Solid lines correspond to numerical simulations, performed with 101 repetitions per frequency point and experimental parameters for fidelity and dephasing. Experimental points (triangular shape), were acquired with 101 repetitions each. Error bars (one standard deviation) are calculated by bootstrap analysis.

width of the distribution becomes more narrowly peaked around the expected value of 2 MHz, while the wings of distribution are strongly suppressed.

To verify that the protocol works over a large dynamic range, we measure the uncertainty as a function of detuning f_B . To account for the periodic nature of phase we use the Holevo variance $V_H = (| \langle e^{i2\pi f_B^{\text{est}} \tau_{\min}} \rangle |)^2 - 1$ as a measure of the uncertainty. We estimate f_B^{est} by taking the mean of the probability density $P(f_B)$ resulting from a single run of the protocol. A fixed initial phase ($\vartheta = 0$ in our experiments) results in a specific dependence of the variance on the magnetic field. For example, for $N = 2$, only four measurement outcomes are possible { 00, 01, 10, 11 }, corresponding to $f_B = 0, -25, -12.5, +12.5$ MHz, respectively. These specific detunings can be measured with the highest accuracy since they correspond to measurements of an eigenstate of our quantum sensor at the end of the Ramsey experiment, while for other frequencies larger statistical fluctuations will be found due to spin projection noise. Figure 4.4c shows V_H as a function of detuning for the parameters $G = 5, F = 7$. Both the experimental data (dots) and the numerical simulation (solid lines) confirm the expected periodic behavior.

4.4 Comparison between adaptive and non-adaptive protocols

We now use our adaptive sensing toolbox to compare different sensing protocols by investigating the scaling of $\eta^2 = V_H T$, averaged over different detunings, as a function of the total sensing time T . First, we will ignore the overhead time due to spin initialization and readout.

We compare the limited-adaptive protocol to the best known non-adaptive protocol and to an optimized adaptive protocol. In the non-adaptive protocol^{21,22,27}, the readout phase for the m^{th} Ramsey experiment is always set to $\vartheta_{n,m} = \frac{m\pi}{M_n}$ ($m = 1..M_n$). In the optimized adaptive protocol^{29,30}, the phase ϑ is updated before each Ramsey and, additionally, a phase $\vartheta_{n,m}^{\text{incr}}$ that depends only on the current values of n, m and the last measurement outcome $\mu_{n,m}$, is added. This additional $\vartheta_{n,m}^{\text{incr}}$ is determined by a numerical minimization of the Holevo variance, via swarm-optimization techniques, taking experimental parameters into account. A detailed description of all protocols is reported in the methods.

We plot experimental data for the sensitivity scaling for the three protocols in Fig. 4.5a alongside simulations using known experimental parameters. In these graph, the SMS limit corresponds to a constant $V_H T$; any scaling behavior with a negative slope thus improves beyond the SMS.

We observe that, for the setting ($G = 5, F = 2$), the non-adaptive protocol reaches only the SMS limit, while both adaptive protocols yield $V_H T$ scaling close to $1/T$. When the number of measurements per interaction time is increased to ($G = 5, F = 7$) the non-adaptive protocol also shows sub-SMS scaling (Fig. 4.5a, blue line). We find this behavior to be quite general: both adaptive and non-adaptive protocols can reach $1/T$ scaling, but the adaptive protocols require fewer measurements (see methods). By comparing the best non-adaptive and the best adaptive protocol, we find that they reach the same sensitivity of $(6.1 \pm 1.7) \text{ nT Hz}^{-\frac{1}{2}}$

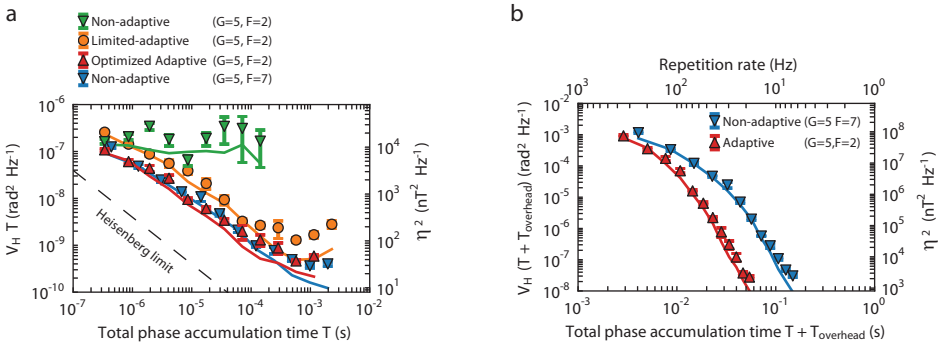


Figure 4.5 | Scaling of sensitivity as a function of total time. (a) The three protocols are compared by plotting $\eta^2 - V_H T$ as a function of the total sensing time T (not including spin initialization and readout). For $(G = 5, F = 2)$ the non-adaptive protocol (green triangles) is bound to the SMS limit, while for both the limited-adaptive (orange circles) and the optimized adaptive (red triangles) protocols η^2 scales close to $1/T$. The sensitivity of the limited-adaptive protocol is, however, worse than the optimized-adaptive one. When increasing the number of Ramsey experiments per sensing time to $(G = 5, F = 7)$, the non-adaptive protocol (blue triangles) reaches Heisenberg-like scaling, with a sensitivity comparable to the optimized adaptive protocol for $(G=5, F=2)$. (b) By including spin initialization and readout durations, the superiority of the optimized adaptive protocol (red triangles), which requires less Ramsey runs per sensing time (smaller F, G) to reach $1/T$ scaling, is evidenced. The optimized adaptive protocol can estimate magnetic fields with a repetition rate of 20 Hz, with a sensitivity more than one order of magnitude better than the non-adaptive protocol. All data are taken with 700 repetitions per data-point. In both plots, error bars corresponding to one standard deviation of the results are obtained using the bootstrap method.

when the longest sensing time reaches T_2^* . The non-adaptive protocol however, requires significantly more measurements (611) than the adaptive protocol (221).

The advantage of adaptive measurements becomes clear when the initialization and readout times (overhead) are taken into account (Fig 4.5b). Since the time required to compute the controlled phase is similar to the initialization time, the two operations can be performed simultaneously, with no additional overhead required by the adaptive protocol (Methods). While the two best protocols still achieve similar minimum sensitivities, the optimized adaptive protocol requires significantly less measurement time. At any fixed measurement time, the adaptive protocol estimates the magnetic field more accurately, allowing a higher repetition rate for the estimation sequences. This is advantageous in the realistic situation that the magnetic field to be estimated is not static: in this case, the estimation time is required to be shorter than the timescale of the fluctuations. Our data shows that at an estimation repetition rate of 20 Hz, the non-adaptive protocol can estimate

4. Optimized quantum sensing using real-time adaptive measurements

a magnetic field with an sensitivity $\eta = (749 \pm 35) \text{ nT Hz}^{-\frac{1}{2}}$, while the optimized-adaptive protocol yields $\eta = (47 \pm 2) \text{ nT Hz}^{-\frac{1}{2}}$.

While the record sensitivity reported here is enabled by single-shot spin readout at low temperature, adaptive techniques can prove valuable also in experiments at room temperature²² where spin-dependent luminescence intensity under off-resonant excitation is typically used to measure the electronic spin. By averaging the signal over multiple repetitions an arbitrarily high readout fidelity can be achieved ($F = 0.99$ for 50,000 repetitions²²). Interestingly, we find that the benefits given by adaptive techniques persist also in case of lower readout fidelities and that the combination of adaptive techniques and optimization of the number of readout repetitions yields a significant improvement (see methods).

In conclusion, by combining high-fidelity single-shot readout at low temperature with a single electron spin sensor and fast electronics, we achieve an unprecedented d.c. sensitivity of $(6.1 \pm 1.7) \text{ nT Hz}^{-\frac{1}{2}}$ with a repetition rate of 20 Hz. Another relevant figure of merit for sensors is the ratio between the range and the sensitivity; the best value found in this work ($B_{max}/\eta \sim 1.5 \cdot 10^5 \text{ Hz}^{\frac{1}{2}}$) improves on previous experiments by two orders of magnitude^{21,22}. Furthermore, we found that the best known adaptive protocol outperforms the best known non-adaptive protocol when overhead is taken into account. These insights can be extended to other quantum sensors and to the detection of different physical quantities such as temperature and electric fields. A remaining open question is whether this adaptive protocol is optimal; perhaps further improvements are possible by taking into account the full measurement history. In a more general picture, the adaptive sensing toolbox demonstrated in this work will enable exploration of the ultimate limits of quantum metrology and may lead to practical sensing devices combining high spatial resolution, sensitivity, dynamic range and repetition rate.

4.5 Methods

4.5.1 Sample and experimental setup

We use an isotopically-purified diamond sample, grown by Element Six Ltd., with 0.01 % ¹³C content. Experiments are performed in a flow cryostat, at the temperature of 8 K. A magnetic field of 12 Gauss is applied to split the energies of the $m_s = \pm 1$ spin states, in order to provide selective spin control by resonant microwave driving. A solid immersion lens is fabricated on top of the NV center by focused ion beam, and covered with an anti-reflective layer, to increase photon collection efficiency. The experiment is controlled by an Adwin Gold microprocessor, with 1 MHz clock cycle. The microprocessor updates the frequency estimate based on the measurement outcomes and calculates the controlled phase. The phase is then converted to an 8-bit number, sent to the FPGA. The FPGA outputs an IQ modulated, 30 MHz sinusoidal pulse, with the specified controlled phase, which drives a vector microwave source.

4.5.2 Adaptive algorithm

For the ℓ -th Ramsey experiment, with outcome μ_ℓ (0 or 1), the estimate of the magnetic field is updated according to Bayes rule: $P(f_B|\mu_1 \dots \mu_\ell) \sim P(f_B|\mu_1 \dots \mu_{(\ell-1)})P(\mu_\ell|f_B)$, with a normalizing proportionality factor. $P(\mu_\ell|f_B)$ is the conditional probability of outcome μ_ℓ (0 or 1) given a frequency f_B :

$$\begin{aligned} P(\mu = 0|f_B) &= \frac{(1 + F_0 - F_1)}{2} + \frac{(F_0 + F_1 - 1)}{2} e^{-(\frac{t}{T_2^*})^2} \cos[2\pi f_B t + \vartheta] \\ P(\mu = 1|f_B) &= 1 - P(\mu = 0|f_B) \end{aligned}$$

where $t = 2^{N-n}\tau_{min}$. Due to its periodicity, it is convenient to express $P(\mu|f_B)$ in a Fourier series, resulting in the following update rule:

$$\begin{aligned} p_k^\ell &= \frac{1 + (-1)^{\mu_\ell}(F_0 - F_1)}{2} p_k^{(\ell-1)} \\ &\quad + e^{-(\frac{t}{T_2^*})^2} \frac{(F_0 + F_1) - 1}{4} \left[e^{i(\mu_\ell \pi + \vartheta_\ell)} p_{k-2^{N-n}}^{(\ell-1)} + e^{-i(\mu_\ell \pi + \vartheta_\ell)} p_{k+2^{N-n}}^{(\ell-1)} \right] \end{aligned}$$

The Bayesian update is performed using the experimental values $F_0 = 0.88$, $F_1 = 0.98$ and $T_2^* = 96 \mu s$. The Holevo variance after each detection, expressed as $V_H = (2\pi|p_{2^{N-n+1}}^{(\ell-1)}|)^{-2} - 1$, can be minimized by choosing, at each step, the following controlled phase for the second $\pi/2$ -pulse²⁸:

$$\vartheta^{ctrl} = \frac{1}{2} \arg\{p_{2^{N-n+1}}^{(\ell-1)}\} \quad (4.1)$$

In the limited-adaptive protocol, this phase is recalculated every time the sensing time is changed. For the optimized-adaptive protocol, the controlled phase is recalculated before every Ramsey experiment and the phase of the second $\pi/2$ -pulse is set to $\vartheta = \vartheta_{\ell,m}^{ctrl} + \vartheta_{n,m}^{incr}$, where $\vartheta_{n,m}^{incr}$ is a phase increment that depends on the last measurement outcome³⁰. To avoid exceeding the memory bounds of the microprocessor, and to optimize speed, we need to minimize the number of coefficients to be tracked and stored. This can be done by determining which coefficients are non-zero and contribute to $p_{2^{N-n+1}}^{\ell-1}$ and neglecting the rest. Moreover, since the probability distribution is real, $(p_k^\ell)^* = p_{-k}^\ell$; therefore we only store and process coefficients p_k^ℓ with $k > 0$. For each Ramsey run, in the case ($G = 5$, $F = 2$), the time taken by the microprocessor to perform the Bayesian update ranges between $80 \mu s$ and $190 \mu s$. This time is comparable to the spin initialization duration, so both operations can be performed simultaneously, with no additional overhead (see methods).

-Here (part of) the SOM of the manuscript submitted to *Nature Nanotechnology* will be added –

4.6 Bibliography

- [1] V. Giovannetti, S. Lloyd and L. Maccone. Advances in quantum metrology. *Nature Photonics* **5**, 222 (2011).
- [2] B. L. Higgins, D. W. Berry, S. D. Bartlett, H. M. Wiseman and G. J. Pryde. Entanglement-free heisenberg-limited phase estimation. *Nature* **450**, 393 (2007).
- [3] C. L. Degen. Scanning magnetic field microscope with a diamond single-spin sensor. *Applied Physics Letters* **92**, 243111 (2008).
- [4] J. M. Taylor *et al.* High-sensitivity diamond magnetometer with nanoscale resolution. *Nature Physics* **4**, 810 (2008).
- [5] J. R. Maze *et al.* Nanoscale magnetic sensing with an individual electronic spin in diamond. *Nature* **455**, 644 (2008).
- [6] G. Balasubramanian *et al.* Nanoscale imaging magnetometry with diamond spins under ambient conditions. *Nature* **455**, 648 (2008).
- [7] G. Balasubramanian *et al.* Ultralong spin coherence time in isotopically engineered diamond. *Nature Materials* **8**, 383 (2009).
- [8] F. Dolde *et al.* Electric-field sensing using single diamond spins. *Nature Physics* **7**, 459 (2011).
- [9] V. M. Acosta *et al.* Temperature dependence of the nitrogen-vacancy magnetic resonance in diamond. *Physical Review Letters* **104**, 070801 (2010).
- [10] D. M. Toyli, C. F. d. l. Casas, D. J. Christle, V. V. Dobrovitski and D. D. Awschalom. Fluorescence thermometry enhanced by the quantum coherence of single spins in diamond. *Proceedings of the National Academy of Sciences* **110**, 8417 (2013).
- [11] P. Ovartchaiyapong, K. W. Lee, B. A. Myers and A. C. B. Jayich. Dynamic strain-mediated coupling of a single diamond spin to a mechanical resonator. *Nature Communications* **5** (2014).
- [12] D. Le Sage *et al.* Optical magnetic imaging of living cells. *Nature* **496**, 486 (2013).
- [13] S. Kaufmann *et al.* Detection of atomic spin labels in a lipid bilayer using a single-spin nanodiamond probe (2013).
- [14] G. Kucsko *et al.* Nanometre-scale thermometry in a living cell. *Nature* **500**, 54 (2013).
- [15] F. Shi *et al.* Single-protein spin resonance spectroscopy under ambient conditions. *Science* **347**, 1135 (2015).

- [16] P. Maletinsky *et al.* A robust scanning diamond sensor for nanoscale imaging with single nitrogen-vacancy centres. *Nature Nanotechnology* **7**, 320 (2012).
- [17] T. Staudacher *et al.* Nuclear magnetic resonance spectroscopy on a (5-nanometer)³ sample volume. *Science* **339**, 561 (2013).
- [18] H. J. Mamin *et al.* Nanoscale nuclear magnetic resonance with a nitrogen-vacancy spin sensor. *Science* **339**, 557 (2013).
- [19] J.-P. Tetienne *et al.* Nanoscale imaging and control of domain-wall hopping with a nitrogen-vacancy center microscope. *Science* **344**, 1366 (2014).
- [20] S. Kolkowitz *et al.* Probing johnson noise and ballistic transport in normal metals with a single-spin qubit. *Science* **347**, 1129 (2015).
- [21] G. Waldherr *et al.* High-dynamic-range magnetometry with a single nuclear spin in diamond. *Nature Nanotechnology* **7**, 105 (2012).
- [22] N. M. Nusran, M. U. Momeen and M. V. G. Dutt. High-dynamic-range magnetometry with a single electronic spin in diamond. *Nature Nanotechnology* **7**, 109 (2012).
- [23] R. Vijay *et al.* Stabilizing rabi oscillations in a superconducting qubit using quantum feedback. *Nature* **490**, 77 (2012).
- [24] M. S. Blok *et al.* Manipulating a qubit through the backaction of sequential partial measurements and real-time feedback. *Nature Physics* **10**, 189 (2014).
- [25] M. D. Shulman *et al.* Suppressing qubit dephasing using real-time hamiltonian estimation. *Nature Communications* **5** (2014).
- [26] L. Robledo *et al.* High-fidelity projective read-out of a solid-state spin quantum register. *Nature* **477**, 574 (2011).
- [27] R. S. Said, D. W. Berry and J. Twamley. Nanoscale magnetometry using a single-spin system in diamond. *Physical Review B* **83**, 125410 (2011).
- [28] P. Cappellaro. Spin-bath narrowing with adaptive parameter estimation. *Physical Review A* **85**, 030301 (2012).
- [29] A. Hentschel and B. C. Sanders. Machine learning for precise quantum measurement. *Physical Review Letters* **104**, 063603 (2010).
- [30] A. J. F. Hayes and D. W. Berry. Swarm optimization for adaptive phase measurements with low visibility. *Physical Review A* **89**, 013838 (2014).

CHAPTER 5

HERALDED ENTANGLEMENT AND UNCONDITIONAL TELEPORTATION BETWEEN SOLID-STATE QUBITS SEPARATED BY THREE METRES

H. Bernien, W. Pfaff, B. Hensen, M.S. Blok, T.H. Taminiau, S.B. van Dam, G. Koolstra, L. Robledo, M.J. Tiggelman, R.N. Schouten, M. Markham, D.J. Twitchen, L. Childress, and R. Hanson

Quantum entanglement between spatially separated objects is a unique resource for quantum information processing and communication. Entangled qubits can be used to establish private information or implement quantum logical gates^{1,2}. Such capabilities are particularly useful when the entangled qubits are spatially separated^{3–5}, opening the opportunity to create highly connected quantum networks⁶ or extend quantum cryptography to long distances^{7,8}. Here we present two key experiments towards the realisation of long-distance quantum networks with solid-state quantum registers. Firstly, we have entangled two electron spin qubits in diamond that are separated by a three-metre distance. Our robust entangling protocol is based on local creation of spin-photon entanglement and a subsequent joint measurement of the photons to herald spin-spin entanglement. The resulting shared Bell-pair between the two nodes then enables the unconditional teleportation of a single nuclear spin state by combining a deterministic Bell-state measurement with real-time feed-forward. These results establish diamond spin qubits as a prime candidate for the realization of quantum networks for quantum communication and network-based quantum computing

The results in this chapter have been published in *Nature* **497**, 86 (2013) and *Science* **345**, 532 (2014).

5.1 Introduction

A quantum network can be constructed by using entanglement to connect local processing nodes, each containing a register of well-controlled and long-lived qubits⁶. Solids are an attractive platform for such registers, as the use of nano-fabrication and material design may enable well-controlled and scalable qubit systems⁹. The potential impact of quantum networks on science and technology has recently spurred research efforts towards generating entangled states of distant solid-state qubits^{10–16}.

A prime candidate for a solid-state quantum register is the nitrogen-vacancy (NV) defect centre in diamond. The NV centre combines a long-lived electronic spin ($S=1$) with a robust optical interface, enabling measurement and high-fidelity control of the spin qubit^{10,17–19}. Furthermore, the NV electron spin can be used to access and manipulate nearby nuclear spins^{20–24}, thereby forming a multi-qubit register. To use such registers in a quantum network requires a mechanism to coherently connect remote NV centres.

Here we demonstrate the generation of entanglement between NV centre spin qubits in distant setups. We achieve this by combining recently established spin initialisation and single-shot readout techniques²⁰ with efficient resonant optical detection and feedback-based control over the optical transitions, all in a single experiment and executed with high fidelity. These results put solid-state qubits on par with trapped atomic qubits^{3–5} as highly promising candidates for implementing quantum networks.

Our experiment makes use of two NV spin qubits located in independent low-temperature setups separated by 3 metres (Fig. 5.1). We encode the qubit basis states $|\uparrow\rangle$ and $|\downarrow\rangle$ in the NV spin sub-levels $m_s = 0$ and $m_s = -1$, respectively. Each qubit can be independently read out by detecting spin-dependent fluorescence in the NV phonon side band (non-resonant detection)²⁰. The qubits are individually controlled with microwave pulses applied to on-chip strip-lines¹⁸. Quantum states encoded in the qubits are extremely long-lived: using dynamical decoupling techniques¹⁸ we obtain a coherence time exceeding 10 ms (Fig. ??), the longest coherence time measured to date for a single electron spin in a solid.

5.2 Heralded entanglement

We generate and herald entanglement between these distant qubits by detecting the resonance fluorescence of the NV centres. The specific entanglement protocol we employ is based on the proposal of S. Barrett and P. Kok²⁵, and is schematically drawn in figure 5.2. Both centres NV A and NV B are initially prepared in a superposition $1/\sqrt{2}(|\uparrow\rangle + |\downarrow\rangle)$. Next, each NV centre is excited by a short laser pulse that is resonant with the $|\uparrow\rangle$ to $|e\rangle$ transition, where $|e\rangle$ is an optically excited state with the same spin projection as $|\uparrow\rangle$. Spontaneous emission locally entangles the qubit and photon number, leaving each setup in the state $1/\sqrt{2}(|\uparrow 1\rangle + |\downarrow 0\rangle)$, where 1 (0) denotes the presence (absence) of an emitted photon; the joint qubit-photon state of both setups is then described by $1/2(|\uparrow_A \uparrow_B\rangle |1_A 1_B\rangle + |\downarrow_A \downarrow_B\rangle |0_A 0_B\rangle + |\uparrow_A \downarrow_B\rangle |1_A 0_B\rangle + |\downarrow_A \uparrow_B\rangle |0_A 1_B\rangle)$. The two photon modes, A and B, are directed to the input

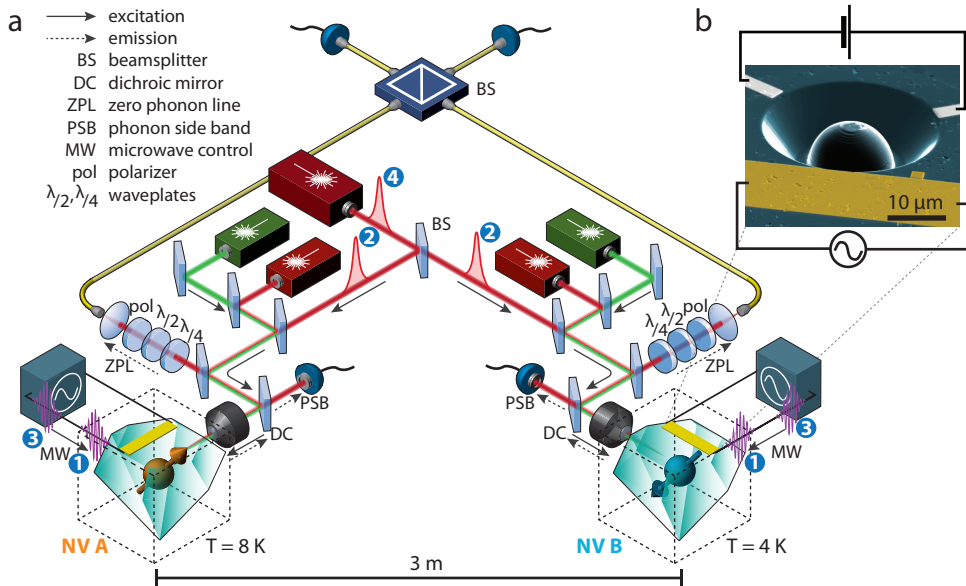


Figure 5.1 | Experimental setup. a Each nitrogen vacancy (NV) centre resides in a synthetic ultra-pure diamond oriented in the $\langle 111 \rangle$ direction. The two diamonds are located in two independent low-temperature confocal microscope setups separated by 3 metres. The NV centres can be individually excited resonantly by a red laser and off-resonantly by a green laser. The emission (dashed arrows) is spectrally separated into an off-resonant part (phonon side band, PSB) and a resonant part (zero-phonon line, ZPL). The PSB emission is used for independent single-shot readout of the spin qubits²⁰. The ZPL photons from the two NV centres are overlapped on a fiber-coupled beamsplitter. Microwave pulses for spin control are applied via on-chip microwave strip-lines. An applied magnetic field of 17.5 G splits the $m_s = \pm 1$ levels in energy. The optical frequencies of NV B are tuned by a d.c. electric field applied to the gate electrodes ((b) scanning electron microscope image of a similar device). To enhance the collection efficiency, solid immersion lenses have been milled around the two NV centres²⁰.

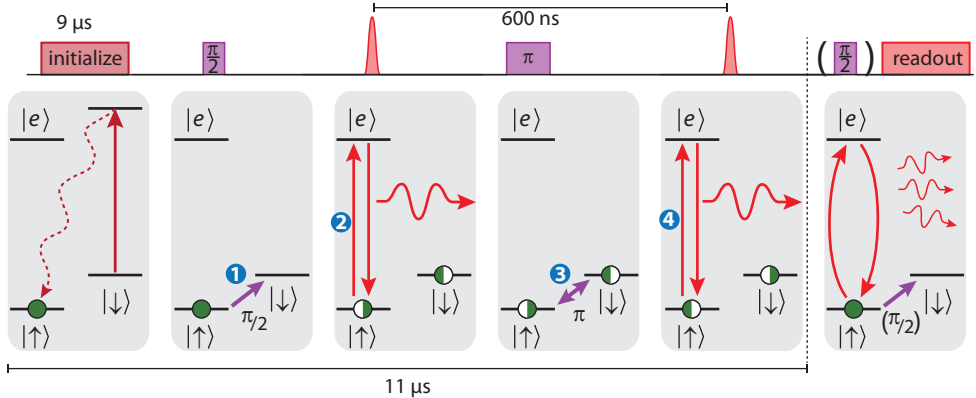


Figure 5.2 | Protocol. Entanglement protocol (details in main text), illustrating the pulse sequence applied simultaneously to both NV centres. Both NV centres are initially prepared in a superposition $1/\sqrt{2}(|\uparrow\rangle + |\downarrow\rangle)$. A short 2 ns spin-selective resonant laser pulse creates spin-photon entanglement $1/\sqrt{2}(|\uparrow 1\rangle + |\downarrow 0\rangle)$. The photons are overlapped on the beamsplitter and detected in the two output ports. Both spins are then flipped, and the NV centres are excited a second time. The detection of one photon in each excitation round heralds the entanglement and triggers individual spin readout.

ports of a beamsplitter (see Fig. 5.1a), so that fluorescence observed in an output port could have originated from either NV centre. If the photons emitted by the two NV centres are indistinguishable, detection of precisely one photon on an output port would correspond to measuring the photon state $|1_A 0_B\rangle \pm e^{-i\varphi} |0_A 1_B\rangle$ (where φ is a phase that depends on the optical path length). Such a detection event would thereby project the qubits onto a maximally entangled state $|\psi\rangle = 1/\sqrt{2}(|\uparrow_A \downarrow_B\rangle \pm e^{-i\varphi} |\downarrow_A \uparrow_B\rangle)$.

Any realistic experiment, however, suffers from photon loss and imperfect detector efficiency; detection of a single photon is thus also consistent with creation of the state $|\uparrow\uparrow\rangle$. To eliminate this possibility, both qubits are flipped and optically excited for a second time. Since $|\uparrow\uparrow\rangle$ is flipped to $|\downarrow\downarrow\rangle$, no photons are emitted in the second round for this state. In contrast, the states $|\psi\rangle$ will again yield a single photon. Detection of a photon in both rounds thus heralds the generation of an entangled state. The second round not only renders the protocol robust against photon loss, but it also changes φ into a global phase, making the protocol insensitive to the optical path length difference²⁶ (see Supporting Material). Furthermore, flipping the qubits provides a refocusing mechanism that counteracts spin dephasing during entanglement generation. The final state is one of two Bell states $|\psi^\pm\rangle = 1/\sqrt{2}(|\uparrow_A \downarrow_B\rangle \pm |\downarrow_A \uparrow_B\rangle)$, with the sign depending on whether the same detector (+), or different detectors (-) clicked in the two rounds.

5.2.1 Implementation

A key challenge for generating remote entanglement with solid-state qubits is obtaining a large flux of indistinguishable photons, in part because local strain in the host lattice can induce large variations in photon frequency. The optical excitation spectra of the NV centres (Fig. 5.3a) display sharp spin-selective transitions. Here we use the E_y transition (spin projection $m_s = 0$) in the entangling protocol and for qubit readout; we use the A_1 transition for fast optical pumping into $|\uparrow\rangle$ ²⁰. Due to different strain in the two diamonds, the frequencies of the E_y transitions differ by 3.5 GHz, more than 100 line-widths. By applying a voltage to an on-chip electrode (Fig. 5.1b) we tune the optical transition frequencies of one centre (NV B) through the d.c. Stark effect^{13,27} and bring the E_y transitions of the two NV centres into resonance (Fig. 5.3a bottom).

Charge fluctuations near the NV centre also affect the optical frequencies. To counteract photo-ionisation we need to regularly apply a green laser pulse to re-pump the NV centre into the desired charge state. This re-pump pulse changes the local electrostatic environment, leading to jumps of several line-widths in the optical transition frequencies²⁸. To overcome these effects, we only initiate an experiment if the number of photons collected during a two-laser probe stage (Fig. 5.3b) exceeds a threshold, thereby ensuring that the NV centre optical transitions are on resonance with the lasers (see chapter ??). The preparation procedure markedly improves the observed optical coherence: as the probe threshold is increased, optical Rabi oscillations persist for longer times (see Fig. 5.3b). For high thresholds, the optical damping time saturates around the value expected for a lifetime-limited line-width²⁸, indicating that the effect of spectral jumps induced by the re-pump laser is strongly mitigated.

Besides photon indistinguishability, successful execution of the protocol also requires that the detection probability of resonantly emitted photons exceeds that of scattered laser photons and of detector dark counts. This is particularly demanding for NV centres since only about 3% of their emission is in the zero-phonon line and useful for the protocol. To minimise detection of laser photons, we use both a cross-polarised excitation-detection scheme (Fig. 5.3c inset) and a detection time filter that exploits the difference between the length of the laser pulse (2 ns) and the NV centre's excited state lifetime (12 ns) (Fig. 5.3c). For a typical detection window used, this reduces the contribution of scattered laser photons to about 1%. Combined with micro-fabricated solid-immersion lenses for enhanced collection efficiency (Fig. 5.1b) and spectral filtering for suppressing non-resonant NV emission, we obtain a detection probability of a resonant NV photon of about 4×10^{-4} per pulse – about 70 times higher than the sum of background contributions.

The degree of photon indistinguishability and background suppression can be obtained directly from the second-order autocorrelation function $g^{(2)}$, which we extract from our entanglement experiment (see Supporting Material). For fully distinguishable photons, the value of $g^{(2)}$ would reach 0.5 at zero arrival time difference. A strong deviation from this behaviour is observed (Fig. 5.3d) due to two-photon quantum interference²⁹ that, for perfectly indistinguishable photons, would make the central peak fully vanish. The remaining

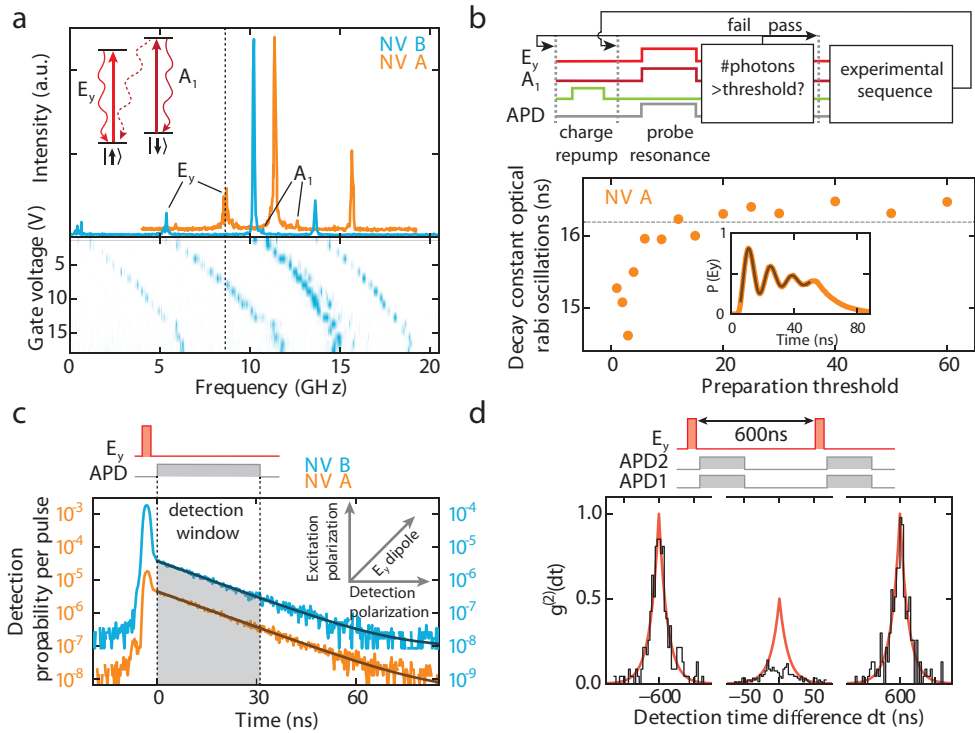


Figure 5.3 | Generating and detecting indistinguishable photons. **a**, Excitation spectra; frequency relative to 470.4515 THz. By applying a voltage to the gates of NV B the E_y transitions are tuned into resonance. **b**, Dynamical preparation of charge and optical resonance. Top: Preparation protocol. A 10 μ s green laser pulse pumps the NV into its negative charge state²⁰. The transition frequencies are probed by exciting the E_y and A_1 transitions for 60 μ s. Conditional on surpassing a certain number of photons detected the experiment is started (pass) or preparation is repeated (fail). APD, avalanche photodiode. Bottom: Line-narrowing effect of the preparation shown by the dependence of the decay time of optical Rabi oscillations on preparation threshold. Dashed line indicates lifetime-limited damping²⁸. **c**, Resonant optical excitation and detection. The polarisation axis of the detection path is aligned perpendicular to the excitation axis. The dipole axis of the E_y transition is oriented in between these two axes (inset). Remaining laser light reflection is time-filtered by defining a photon detection window that starts after the laser pulse. **d**, Two-photon quantum interference using resonant excitation and detection. The $g^{(2)}$ correlation function is obtained from all coincidence detection events of APD 1 and APD 2 during the entanglement experiment (see Supporting Material). The side-peaks are fit to an exponential decay; from the fit values, we obtain the expected central peak shape $g_{\perp}^{(2)}$ (red line) for non-interfering photons. The visibility of the interference is given by $(g_{\perp}^{(2)} - g^{(2)})/g_{\perp}^{(2)}$.

coincidences are likely caused by (temperature-dependent) phonon-induced transitions between optically excited states³⁰ in NV A. The visibility of the two-photon interference observed here – $(80 \pm 5)\%$ for $|dt| < 2.56$ ns – is a significant improvement over previously measured values^{13,14} and key to the success of the entangling scheme.

To experimentally generate and detect remote entanglement, we run the following sequence: First, both NV centres are independently prepared into the correct charge state and brought into optical resonance according to the scheme in figure 5.3b. Then we apply the entangling protocol shown in figure 5.2 using a 600 ns delay between the two optical excitation rounds. We repeat the protocol 300 times before we return to the resonance preparation step; this number is a compromise between maximising the attempt rate and minimising the probability of NV centre ionisation. A fast logic circuit monitors the photon counts in real time and triggers single-shot qubit readout on each setup whenever entanglement is heralded, i.e. whenever a single photon is detected in each round of the protocol. The readout projects each qubit onto the $\{|\uparrow\rangle, |\downarrow\rangle\}$ states (Z-basis), or on the $\{|\uparrow\rangle \pm |\downarrow\rangle, |\uparrow\rangle \mp |\downarrow\rangle\}$ states (X or $-X$ basis). The latter two are achieved by first rotating the qubit by $\pi/2$ using a microwave pulse before readout. By correlating the resulting single-qubit readout outcomes we can verify the generation of the desired entangled states. To obtain reliable estimates of the two-qubit state probabilities, we correct the raw data with a maximum-likelihood method for local readout infidelities. These readout errors are known accurately from regular calibrations performed during the experiment (see Supporting Material).

5.2.2 Demonstration of remote entanglement

Figure 5.4 shows the obtained correlations. When both qubits are measured along Z (readout basis $\{Z, Z\}$), the states ψ^+ and ψ^- (as identified by their different photon signatures) display strongly anti-correlated readout results (odd parity). The coherence of the joint qubit state is revealed by measurements performed in rotated bases ($\{X, X\}$, $\{-X, X\}$), which also exhibit significant correlations. Furthermore, these measurements allow us to distinguish between states ψ^+ and ψ^- . For ψ^+ the $\{X, X\}$ ($\{-X, X\}$) outcomes exhibit even (odd) parity, whereas the ψ^- state displays the opposite behaviour, as expected. The observed parities demonstrate that the experiment yields the two desired entangled states.

We calculate a strict lower bound on the state fidelity by combining the measurement results from different bases (see Supporting Material):

$$F = \langle \psi^\pm | \rho | \psi^\pm \rangle \geq 1/2(P_{\uparrow\downarrow} + P_{\downarrow\uparrow} + C) - \sqrt{P_{\uparrow\uparrow}P_{\downarrow\downarrow}}, \quad (5.1)$$

where P_{ij} is the probability for the measurement outcome ij in the $\{Z, Z\}$ basis (i.e. the diagonal elements of the density matrix ρ) and C is the contrast between odd and even outcomes in the rotated bases. We find a lower bound of $(69 \pm 5)\%$ for ψ^- and $(58 \pm 6)\%$ for ψ^+ , and probabilities of 99.98% and 91.8%, respectively, that the state fidelity is above the classical limit of 0.5. These values firmly establish that we have created remote entanglement.

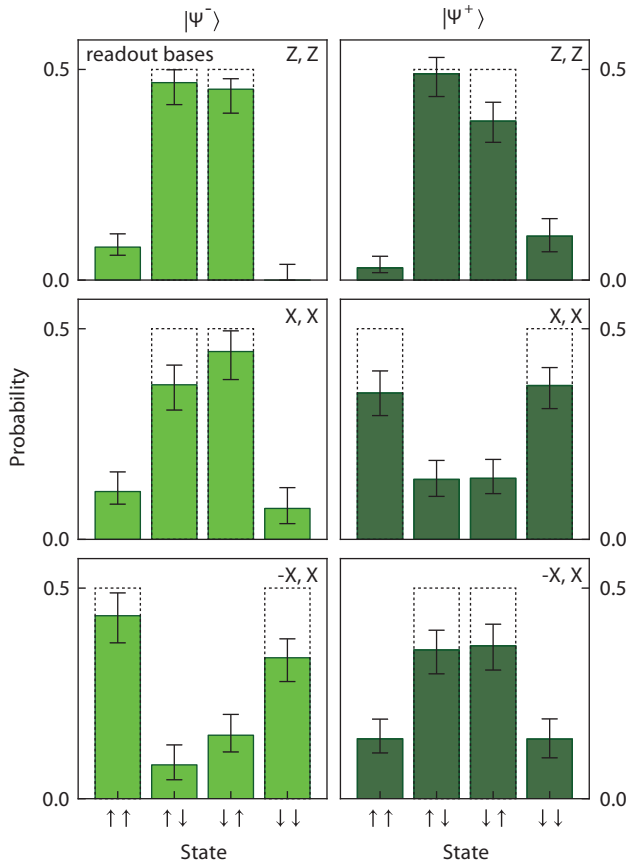


Figure 5.4 | Verification of entanglement by spin-spin correlations. Each time that entanglement is heralded the spin qubits are individually read out and their results correlated. The readout bases for NV A and NV B can be rotated by individual microwave control (see text). The state probabilities are obtained by a maximum-likelihood estimation on the raw readout results (see Supporting Material). Error bars depict 68% confidence intervals; dashed lines indicate expected results for perfect state fidelity. Data is obtained from 739 heralding events. For ψ^- , the detection window in each round is set to 38.4 ns, and the maximum absolute detection time difference $|\delta\tau|$ between the two photons relative to their laser pulses is restricted to 25.6 ns. $\delta\tau = \tau_2 - \tau_1$, where τ_1 is the arrival time of the first photon relative to the first laser pulse and τ_2 the arrival time of the second photon relative to the second laser pulse. For ψ^+ the second detection window is set to 19.2 ns with $|\delta\tau| < 12.8$ ns, in order to reduce the effect of photo-detector after-pulsing.

The lower bound on the state fidelity given above takes into account the possible presence of coherence within the even-parity subspace $\{|\uparrow\uparrow\rangle, |\downarrow\downarrow\rangle\}$. However, the protocol selects out states with odd parity and therefore this coherence is expected to be absent. To compare the results to the expected value and to account for sources of error, we set the related (square-root) term in Eq. 1 to zero and obtain for the data in figure 5.4 as best estimate $F = (73 \pm 4)\%$ for ψ^- and $F = (64 \pm 5)\%$ for ψ^+ .

Several known error sources contribute to the observed fidelity. Most importantly, imperfect photon indistinguishability reduces the coherence of the state. The fidelity is further decreased by errors in the microwave pulses (estimated at 3.5%), spin initialisation (2%), spin decoherence (< 1%) and spin flips during the optical excitation (1%) (see Supporting Material). Moreover, ψ^+ is affected by after-pulsing, whereby detection of a photon in the first round triggers a fake detector click in the second round. Such after-pulsing leads to a distortion of the correlations (see for example the increased probability for $|\downarrow\downarrow\rangle$ in figure 5.4) and thereby a reduction in fidelity for ψ^+ (see Supporting Material). Besides these errors that reduce the actual state fidelity, the measured value is also slightly lowered by a conservative estimation for readout infidelities and by errors in the final microwave $\pi/2$ pulse used for reading out in a rotated basis.

The success probability of the protocol is given by $P_\psi = 1/2\eta_A\eta_B$. η_i is the overall detection efficiency of resonant photons from NV i and the factor 1/2 takes into account cases where the two spins are projected into $|\downarrow\downarrow\rangle$ or $|\uparrow\uparrow\rangle$, which are filtered out by their different photon signature. In the current experiment we estimate $P_\psi \approx 1.610^{-7}$. The entanglement attempt rate is about 20 kHz, yielding one entanglement event per 10 minutes. This is in good agreement with the 739 entanglement events obtained over a time of 158 hours.

Creation of entanglement between distant spin qubits in diamond, as reported here, opens the door to extending the remarkable properties of NV-based quantum registers towards applications in quantum information science. A natural path forward is the incorporation of auxiliary nuclear spin qubits at the local nodes. In the following we discuss a second experiment where the nitrogen spin initialization and decoherence protected gates (as described in chapter 3) are combined with an improved entanglement protocol to realize a deterministic Bell-state measurement which enables teleportation between a single nuclear spin and a distant electron spin.

5.3 Teleportation

Teleportation allows quantum information to be faithfully transmitted over arbitrary distances provided the two parties (“Alice” and “Bob”) have previously established a shared entangled state and can communicate classically. In the teleportation protocol (Fig. 5.5) Alice is initially in possession of the state to be teleported (qubit 1) which is most generally given by $|\psi\rangle = \alpha|0\rangle + \beta|1\rangle$. Alice and Bob each have one qubit of an entangled pair (qubits 2 and 3) in the joint state $|\Psi^-\rangle_{23} = (|01\rangle_{23} - |10\rangle_{23})/\sqrt{2}$. The combined state of all three

qubits can be rewritten as

$$\begin{aligned} |\psi\rangle_1 \otimes |\Psi^-\rangle_{23} = & \frac{1}{2} (|\Phi^+\rangle_{12} \otimes (\alpha|1\rangle_3 - \beta|0\rangle_3) \\ & + |\Phi^-\rangle_{12} \otimes (\alpha|1\rangle_3 + \beta|0\rangle_3) \\ & + |\Psi^+\rangle_{12} \otimes (-\alpha|0\rangle_3 + \beta|1\rangle_3) \\ & - |\Psi^-\rangle_{12} \otimes (\alpha|0\rangle_3 + \beta|1\rangle_3)), \end{aligned} \quad (5.2)$$

where $|\Phi^\pm\rangle = (|00\rangle \pm |11\rangle)/\sqrt{2}$ and $|\Psi^\pm\rangle = (|01\rangle \pm |10\rangle)/\sqrt{2}$ are the four Bell states. To teleport the quantum state Alice performs a joint measurement on her qubits (qubits 1 and 2) in the Bell basis, projecting Bob's qubit into a state that is equal to $|\psi\rangle$ up to a unitary operation that depends on the outcome of Alice's measurement. Alice sends the outcome via a classical communication channel to Bob, who can then recover the original state by applying the corresponding local transformation.

Because the source qubit state always disappears on Alice's side, it is irrevocably lost whenever the protocol fails. Therefore, to ensure that each qubit state inserted into the teleporter unconditionally re-appears on Bob's side, Alice must be able to distinguish between all four Bell states in a single shot and Bob has to preserve the coherence of the target qubit during the communication of the outcome and the final conditional transformation. Several pioneering experiments have explored teleportation between remote nodes^{31–33} but unconditional teleportation between long-lived qubits^{34–36} has so far only been demonstrated within a local qubit register^{25,37,38}.

We demonstrate unconditional teleportation between diamond spin qubits residing in independent setups separated by 3 meters. This result is achieved by fully separating the generation of remote entanglement (the preparation of the teleporter) as from the two-qubit Bell-state measurement and feed-forward (the actual teleportation action). In particular, a photonic channel is used to generate heralded remote entanglement between two nitrogen-vacancy (NV) center electronic spins, while the teleportation protocol solely exploits matter qubits that – unlike photonic qubits – allow for a deterministic Bell-state measurement with current technology. The source state is encoded in a nuclear spin close to one of the NV electron spins after preparation of the teleporter. We preserve the target qubit's coherence by dynamical decoupling while the measurement outcome is forwarded and the final correction pulse is applied. This protocol ensures that the source state is successfully teleported in each of the experimental runs.

Alice and Bob each operate an independent low-temperature confocal microscope setup that addresses a single NV center. The two NV electronic spins (labeled as qubits 2 and 3) are initialized in the non-local entangled state $|\Psi^-\rangle_{23} = (|01\rangle_{23} - |10\rangle_{23})/\sqrt{2}$ according to the protocol described in 5.2, with the following improvements: We have further enhanced the efficiency of photon collection from our device through optimization of the SIL fabrication and by adding an anti-reflection coating. Also, we have significantly improved both the spectral stability of the NV center's optical transition and the charge state initialization by

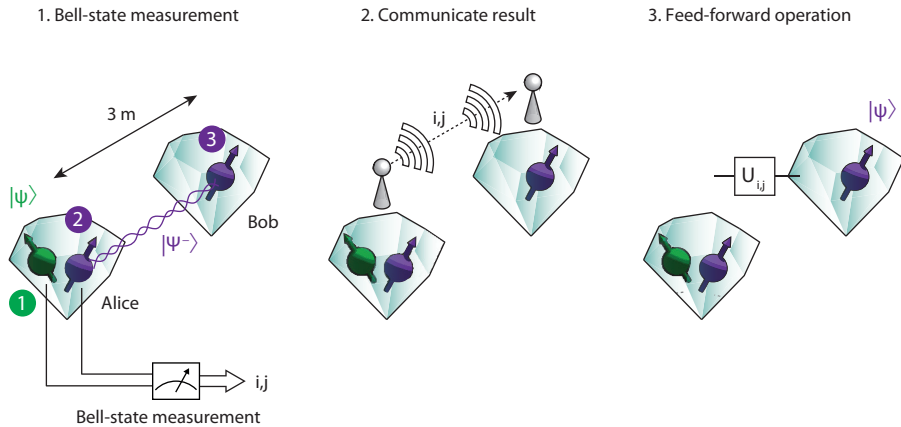


Figure 5.5 | Teleportation scheme. General scheme for teleportation. In our experiment Alice and Bob each control a single NV center in a single-crystal CVD-grown diamond by operating an independent cryogenic confocal microscope setup ($T = 8\text{ K}$ for Alice and $T = 4\text{ K}$ for Bob).

resonant re-pumping on the neutral-charge state zero-phonon line³⁹. As a result we were able to increase the generation rate of the entangled state $|\Psi^-\rangle_{23}$ fivefold to $1/250\text{ s}^{-1}$ and improve the entangled state fidelity from 0.73 to an estimated 0.87.

The additional qubit in Alice's node – essential for making the teleportation unconditional – is provided by the nitrogen-14 nuclear spin of Alice's NV (qubit 1). Before establishing the entanglement link, this nuclear spin is initialized into state $|1\rangle$ by a projective measurement via the electron spin²⁰. We reinitialize the nuclear spin after each 250 entanglement attempts in order to preserve its purity (Figs. 5.6a,b). We prepare the source state after establishing remote entanglement, thus avoiding possible dephasing of the source state by repeated optical excitation of the nearby electron^{40,41} during entanglement generation. We employ a decoherence-protected gate¹⁹ on Alice's side to set the nuclear spin to the source state $|\psi\rangle = \alpha|0\rangle + \beta|1\rangle$. This gate combines two nuclear spin rotations with a refocusing pulse on the electron spin such that the entangled state is efficiently preserved for the duration of the gate (Figs. 5.7a). This operation concludes the preparation of the teleporter and the insertion of the source qubit, with the three-qubit system left in the state $|\psi\rangle_1 \otimes |\Psi^-\rangle_{23} = (\alpha|0\rangle_1 + \beta|1\rangle_1) \otimes (|01\rangle_{23} - |10\rangle_{23})/\sqrt{2}$.

At the heart of unconditional qubit teleportation is a deterministic Bell-state measurement (BSM) by Alice on qubits 1 and 2 that generally involves two steps. First, the four Bell states are mapped onto the four different qubit eigenstates $|i\rangle_1 |j\rangle_2$ by quantum gate operations. In the second step each of the two qubits is read out in a single shot and the two measurement outcomes are sent to Bob. Our implementation of this scheme is shown in Figs. 5.7a. We

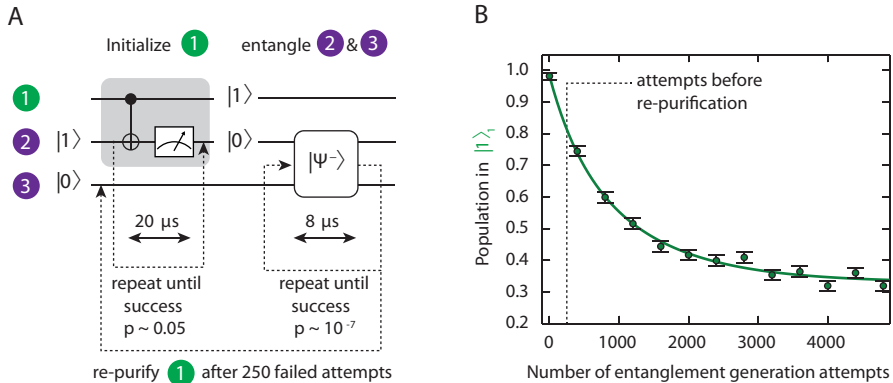


Figure 5.6 | Preparation of the teleporter. (a) Circuit diagram for the periodic measurement-based re-initialization of the nuclear spin (qubit 1) in between remote entanglement generation attempts. Both the probability for success per attempt and the time duration of a single attempt are indicated for the initialization by measurement of qubit 1 and the generation of entanglement between qubits 2 and 3. (b) Measured probability $P(|1\rangle)$ to preserve the initialized nuclear spin state $|1\rangle$ as a function of number of entanglement generation attempts N_{ent} . A fit (solid line) to a rate-equation model yields a probability of $(0.85 \pm 0.05) \times 10^{-3}$ per entanglement generation attempt that the nuclear spin flips. The dashed line marks the maximum number of attempts before the nuclear spin is re-initialized ($N_{\text{ent}} = 250$).

implement the Bell-state mapping by applying a two-qubit controlled-NOT gate (CNOT) followed by a $\pi/2$ rotation on the nuclear spin using another decoherence-protected gate. Then we read out the electron spin in a single shot (average fidelity 0.963 ± 0.005). Finally we read out the nuclear spin by mapping its state onto the electron spin followed by electron spin readout. The two single-shot readout results give the outcome of the BSM.

We benchmark the BSM by preparing each of the four Bell states as input states in Alice's register (Fig. 5.7b). This procedure yields an uncorrected mean fidelity, given by the probability to obtain the measurement result corresponding to the prepared Bell state, of 0.89 ± 0.02 . To gain more insight into the sources of imperfections we compare the data with numerical simulations that use the independently determined infidelities of the nuclear spin initialization, CNOT gate, and electron single-shot readout as input. These simulations predict an average fidelity of 0.9 (Fig. 5.7b), in excellent agreement with the data. Taking known errors in the preparation of the input states into account, we infer a BSM fidelity of 0.93 ± 0.02 .

The final challenge for successful unconditional teleportation is to maintain the coherence of Bob's target qubit (qubit 3) during the BSM and feed-forward. In our experiment, Bob's

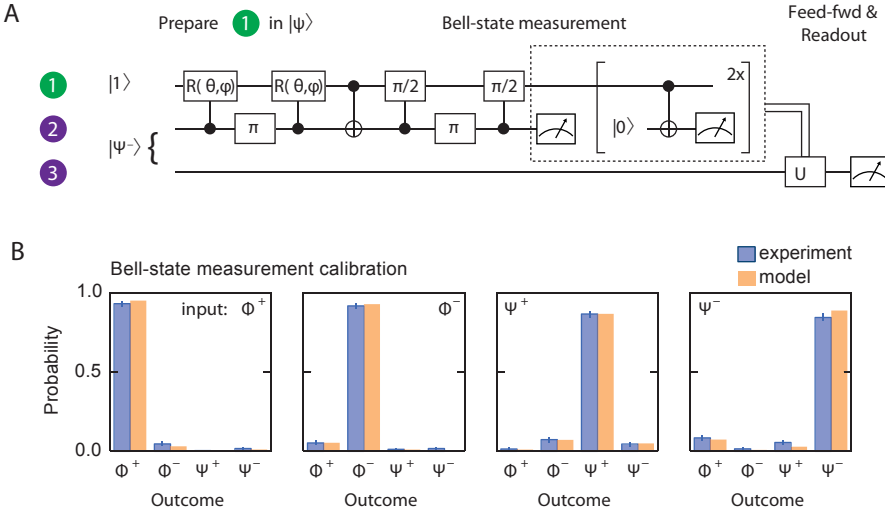


Figure 5.7 | Deterministic Bell-state measurement (BSM) and real-time feed-forward. (a) Circuit diagram of our implementation. The label ‘e’ (‘N’) indicates operations acting on the electron spin (nitrogen nuclear spin). To enhance the readout fidelity for the nuclear spin, we perform the mapping to the electron spin via a CNOT and the subsequent electron readout twice. While Alice is performing her BSM Bob applies an XY4 decoupling sequence on his electron qubit. After receiving the BSM outcome from Alice, Bob applies the feed-forward operation U and reads out his qubit. $\pi_{x,y}$ denote rotations around the x -axis and y -axis, respectively. (b) Calibration of the BSM by inserting the four different Bell states on Alice’s side and determining the probability with which the ideal outcome is observed (blue bars). Data is not corrected for imperfect preparation of the input states. Expectations based on independently determined experimental imperfections are shown in orange. Error bars are two statistical s.d.

qubit is mostly affected by interactions with the surrounding nuclear spin bath. We counteract this decoherence by applying an XY4 dynamical decoupling sequence¹⁸. The time between entanglement generation and the triggering of the feed-forward operation based on the BSM outcome is $300\ \mu\text{s}$. For this duration the decoupling protocol preserves the qubit state with an average fidelity of 0.96 ± 0.02 .

We first verify that the teleporter is calibrated correctly by applying it to the nominal input state $|Y\rangle = (|0\rangle + i|1\rangle)/\sqrt{2}$ and performing tomography on the state that appears on Bob’s side. The reconstructed density matrix (Fig. 5.8B) shows that the target state vector is aligned well with Y and therefore that the reference frames of Alice and Bob are correctly set.

To prove that our quantum teleporter outperforms any classical communication strategy,

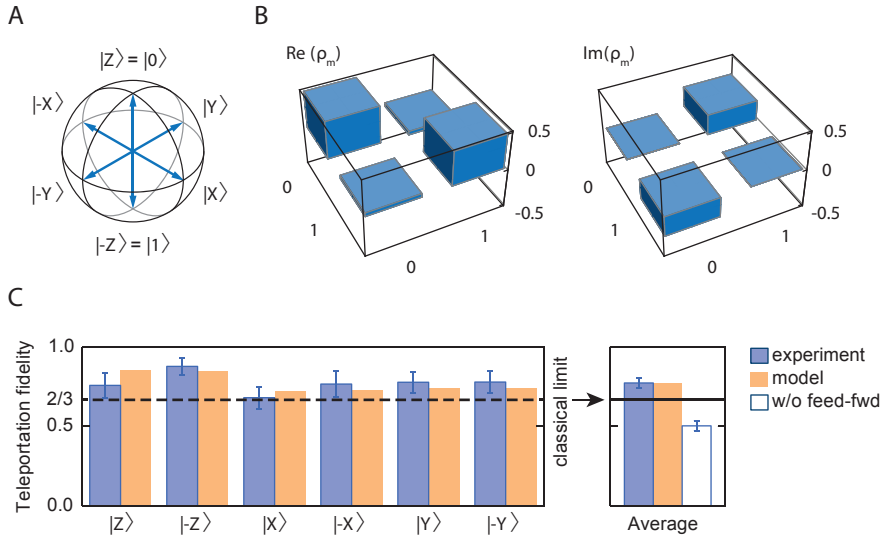


Figure 5.8 | Demonstration of unconditional quantum teleportation between remote qubits. (a) Bloch sphere with the six mutually unbiased basis states that we teleport. $|\pm X\rangle = (|0\rangle \pm |1\rangle)/\sqrt{2}$, $|\pm Y\rangle = (|0\rangle \pm i|1\rangle)/\sqrt{2}$. (b) State tomography after teleportation of the input state $|Y\rangle$. We determine the density matrix ρ_m by measuring the expectation values of the Pauli spin operators, $\langle \sigma_x \rangle$, $\langle \sigma_y \rangle$, $\langle \sigma_z \rangle$, where the required qubit rotations before readout are performed conditional on the BSM outcome. The measured (ideal) entries of the density matrix are $\rho_{00} = 1 - \rho_{11} = 0.52 \pm 0.08$ (0.5) and $\rho_{01} = \rho_{10}^* = 0.05 \pm 0.08 - i0.28 \pm i0.07$ ($-i0.5$), respectively. (c) Average teleportation fidelity from the measured fidelities of the six states (blue bars). Sample sizes are (left to right) 54, 89, 73, 49, 52, and 47. Predictions from simulations are shown in orange. Without feed-forward, the target state is completely mixed (white bar). The horizontal line marks the classical limit of $2/3$. Data is not corrected for source state initialization errors. Uncertainties are one statistical s.d.

we teleport an unbiased set of six basis states $|\psi\rangle$ (Fig. 5.8A) and determine the fidelity of the teleported state on Bob's side with respect to the ideal input state. In these experiments we use a feed-forward operation that maps the ideal state of qubit 3 onto a qubit eigenstate such that the readout directly yields the teleportation fidelity. Since the feed-forward operation is conditional on the BSM outcome, ignoring the BSM outcome yields a completely mixed state and random outcomes ensuring that no information is transmitted. Without feed-forward we indeed observe an average teleportation fidelity of $\langle F \rangle = 0.50 \pm 0.03$ (Fig. 5.8C). In contrast, including the feed-forward loop we find $\langle F \rangle = 0.77 \pm 0.03$. This value exceeds the classical limit of $2/3$ by more than 3 standard deviations, thus proving the quantum nature of our teleporter. We note that this fidelity presents a lower bound on the actual teleportation fidelity because it does not take into account initialization errors of the source state. Importantly, this result is obtained without any post-selection: each teleportation attempt is included in the data presented here.

We also simulate the outcomes by using independently determined infidelities in the protocol. The only unknown parameter is the fidelity of the entangled state shared by Alice and Bob. We find that our data is well reproduced by the simulations if we assume a fidelity to the ideal Bell state $|\Psi^-\rangle_{23}$ of 0.87 (Fig. 5.8C). The simulations also enable us to quantify the effect of imperfect initialization of the source qubit on the measured fidelities. In this way we estimate the teleportation fidelity to be ~ 0.86 .

The ability to generate remote entanglement and to control and read out multiple qubits per node as shown in the present teleportation experiment makes NV centers a leading candidate for realizing a quantum network. Our teleportation scheme is both unconditional and scalable to large distances as it can mitigate photon loss by heralding and purification of the distributed entangled state⁴². In future experiments we aim to supplement our current capabilities with quantum memories that are robust against optical excitation of the electrons, enabling remote entanglement purification and the connection of multiple nodes into the network. A promising route is the use of weakly coupled nuclear spins^{43–45} on which multi-qubit quantum control has very recently been demonstrated⁴⁶. For such nuclear spins, coherence times of over 1 second under optical excitation have been reported²³, while the incorporation of NV centers into optical cavities may enable remote entanglement generation on millisecond timescales⁴⁷. Furthermore, the entanglement and readout fidelities reported here are sufficient for a violation of a Bell inequality with the detection loophole closed, making NV centers a promising system for realizing a loophole-free Bell test and device-independent quantum key distribution⁴⁸.

5.4 Methods

– Here (part of) the SOM of *Nature* **497**, 86 (2013) and *Science* **345**, 532 (2014) will be added –

5.5 Bibliography

- [1] M. A. Nielsen and I. L. Chuang. *Quantum Computation and Quantum Information*. Cambridge University Press (2000).
- [2] R. Raussendorf and H. J. Briegel. A one-way quantum computer. *Physical Review Letters* **86**, 5188 (2001).
- [3] D. L. Moehring *et al.* Entanglement of single-atom quantum bits at a distance. *Nature* **449**, 68 (2007).
- [4] S. Ritter *et al.* An elementary quantum network of single atoms in optical cavities. *Nature* **484**, 195 (2012).
- [5] J. Hofmann *et al.* Heralded entanglement between widely separated atoms. *Science* **337**, 72 (2012).
- [6] H. J. Kimble. The quantum internet. *Nature* **453**, 1023 (2008).
- [7] L.-M. Duan, M. D. Lukin, J. I. Cirac and P. Zoller. Long-distance quantum communication with atomic ensembles and linear optics. *Nature* **414**, 413 (2001).
- [8] L. Childress, J. M. Taylor, A. S. Sørensen and M. D. Lukin. Fault-tolerant quantum communication based on solid-state photon emitters. *Physical Review Letters* **96**, 070504 (2006).
- [9] T. D. Ladd *et al.* Quantum computers. *Nature* **464**, 45 (2010).
- [10] E. Togan *et al.* Quantum entanglement between an optical photon and a solid-state spin qubit. *Nature* **466**, 730 (2010).
- [11] W. B. Gao, P. Fallahi, E. Togan, J. Miguel-Sánchez and A. Imamoglu. Observation of entanglement between a quantum dot spin and a single photon. *Nature* **491**, 426 (2012).
- [12] K. De Greve *et al.* Quantum-dot spin-photon entanglement via frequency downconversion to telecom wavelength. *Nature* **491**, 421 (2012).
- [13] H. Bernien *et al.* Two-photon quantum interference from separate nitrogen vacancy centers in diamond. *Physical Review Letters* **108**, 043604 (2012).
- [14] A. Sipahigil *et al.* Quantum interference of single photons from remote nitrogen-vacancy centers in diamond. *Physical Review Letters* **108**, 143601 (2012).
- [15] R. B. Patel *et al.* Two-photon interference of the emission from electrically tunable remote quantum dots. *Nature Photonics* **4**, 632 (2010).
- [16] E. B. Flagg *et al.* Interference of single photons from two separate semiconductor quantum dots. *Physical Review Letters* **104**, 137401 (2010).

- [17] G. D. Fuchs, V. V. Dobrovitski, D. M. Toyli, F. J. Heremans and D. D. Awschalom. Gigahertz dynamics of a strongly driven single quantum spin. *Science* **326**, 1520 (2009).
- [18] G. d. Lange, Z. H. Wang, D. Ristè, V. V. Dobrovitski and R. Hanson. Universal dynamical decoupling of a single solid-state spin from a spin bath. *Science* **330**, 60 (2010).
- [19] T. van der Sar *et al.* Decoherence-protected quantum gates for a hybrid solid-state spin register. *Nature* **484**, 82 (2012).
- [20] L. Robledo *et al.* High-fidelity projective read-out of a solid-state spin quantum register. *Nature* **477**, 574 (2011).
- [21] P. Neumann *et al.* Single-shot readout of a single nuclear spin. *Science* **329**, 542 (2010).
- [22] P. Neumann *et al.* Multipartite entanglement among single spins in diamond. *Science* **320**, 1326 (2008).
- [23] P. C. Maurer *et al.* Room-temperature quantum bit memory exceeding one second. *Science* **336**, 1283 (2012).
- [24] W. Pfaff *et al.* Demonstration of entanglement-by-measurement of solid-state qubits. *Nature Physics* **9**, 29 (2013).
- [25] M. D. Barrett *et al.* Deterministic quantum teleportation of atomic qubits. *Nature* **429**, 737 (2004).
- [26] S. D. Barrett and P. Kok. Efficient high-fidelity quantum computation using matter qubits and linear optics. *Physical Review A* **71**, 060310 (2005).
- [27] L. C. Bassett, F. J. Heremans, C. G. Yale, B. B. Buckley and D. D. Awschalom. Electrical tuning of single nitrogen-vacancy center optical transitions enhanced by photoinduced fields. *Physical Review Letters* **107**, 266403 (2011).
- [28] L. Robledo, H. Bernien, I. van Weperen and R. Hanson. Control and coherence of the optical transition of single nitrogen vacancy centers in diamond. *Physical Review Letters* **105**, 177403 (2010).
- [29] C. K. Hong, Z. Y. Ou and L. Mandel. Measurement of subpicosecond time intervals between two photons by interference. *Physical Review Letters* **59**, 2044 (1987).
- [30] K.-M. C. Fu *et al.* Observation of the dynamic jahn-teller effect in the excited states of nitrogen-vacancy centers in diamond. *Physical Review Letters* **103**, 256404 (2009).
- [31] S. Olmschenk *et al.* Quantum teleportation between distant matter qubits. *Science* **323**, 486 (2009).
- [32] C. Nölleke *et al.* Efficient teleportation between remote single-atom quantum memories. *Physical Review Letters* **110**, 140403 (2013).

- [33] H. Krauter *et al.* Deterministic quantum teleportation between distant atomic objects. *Nature Physics* **9**, 400 (2013).
- [34] D. D. Awschalom, L. C. Bassett, A. S. Dzurak, E. L. Hu and J. R. Petta. Quantum spintronics: Engineering and manipulating atom-like spins in semiconductors. *Science* **339**, 1174 (2013).
- [35] M. H. Devoret and R. J. Schoelkopf. Superconducting circuits for quantum information: An outlook. *Science* **339**, 1169 (2013).
- [36] C. Monroe and J. Kim. Scaling the ion trap quantum processor. *Science* **339**, 1164 (2013).
- [37] M. Riebe *et al.* Deterministic quantum teleportation with atoms. *Nature* **429**, 734 (2004).
- [38] L. Steffen *et al.* Deterministic quantum teleportation with feed-forward in a solid state system. *Nature* **500**, 319 (2013).
- [39] P. Siyushev *et al.* Optically controlled switching of the charge state of a single nitrogen-vacancy center in diamond at cryogenic temperatures. *Physical Review Letters* **110**, 167402 (2013).
- [40] L. Jiang *et al.* Coherence of an optically illuminated single nuclear spin qubit. *Physical Review Letters* **100**, 073001 (2008).
- [41] M. S. Blok *et al.* Manipulating a qubit through the backaction of sequential partial measurements and real-time feedback. *Nature Physics* **10**, 189 (2014).
- [42] H.-J. Briegel, W. Dür, J. I. Cirac and P. Zoller. Quantum repeaters: The role of imperfect local operations in quantum communication. *Physical Review Letters* **81**, 5932 (1998).
- [43] T. H. Taminiau *et al.* Detection and control of individual nuclear spins using a weakly coupled electron spin. *Physical Review Letters* **109**, 137602 (2012).
- [44] S. Kolkowitz, Q. P. Unterreithmeier, S. D. Bennett and M. D. Lukin. Sensing distant nuclear spins with a single electron spin. *Physical Review Letters* **109**, 137601 (2012).
- [45] N. Zhao *et al.* Sensing single remote nuclear spins. *Nature Nanotechnology* **7**, 657 (2012).
- [46] T. H. Taminiau, J. Cramer, T. v. d. Sar, V. V. Dobrovitski and R. Hanson. Universal control and error correction in multi-qubit spin registers in diamond. *Nature Nanotechnology* **9**, 171 (2014).
- [47] M. Lončar and A. Faraon. Quantum photonic networks in diamond. *MRS Bulletin* **38**, 144 (2013).
- [48] N. Brunner, D. Cavalcanti, S. Pironio, V. Scarani and S. Wehner. Bell nonlocality. *Reviews of Modern Physics* **86**, 419 (2014).

CHAPTER 6

ANALYSIS OF A QUANTUM MEMORY WITH OPTICAL INTERFACE IN DIAMOND

M.S. Blok*, N. Kalb*, A. Reiserer, T.H. Taminiau and R. Hanson

Single defect centers in diamond have emerged as a powerful platform for quantum optics experiments and quantum information processing tasks¹. Connecting spatially separated nodes via optical photons² into a quantum network will enable distributed quantum computing and long-range quantum communication. Initial experiments on trapped atoms and ions as well as defects in diamond have demonstrated entanglement between two nodes over several meters^{3–6}. To realize multi-node networks, additional quantum bit systems that store quantum states while new entanglement links are established are highly desirable. Such memories allow for entanglement distillation, purification and quantum repeater protocols that extend the size, speed and distance of the network^{7–10}. However, to be effective the memory must be robust against the entanglement generation protocol, which typically must be repeated many times. Here we evaluate the prospects of using carbon nuclear spins in diamond as quantum memories that are compatible with quantum networks based on single nitrogen vacancy (NV) defects in diamond. We present a theoretical framework to describe the dephasing of the nuclear spins under repeated generation of NV spin-photon entanglement and show that quantum states can be stored during hundreds of repetitions using typical experimental coupling parameters. This result demonstrates that nuclear spins with weak hyperfine couplings are promising quantum memories for quantum networks.

This chapter has been accepted for publication in *Faraday Discussions* (2015).

* these authors contributed equally to this work

6.1 Introduction

Spins associated with the nitrogen-vacancy (NV) center, an atomic defect in diamond, have recently emerged as a promising platform for quantum networks^{1,11}. The NV-center's long-lived electron spin state ($S = 1$) can be controlled by magnetic resonance and can be initialized and read out optically. At cryogenic temperatures (< 10 K), coherent optical transitions allow for the generation of spin-photon entanglement¹² and of entanglement between spatially separated NV center electron spins^{6,13}.

In addition, the electron spin couples to nuclear spins in the environment through the hyperfine interaction. Control over the host nitrogen spin and over multiple nearby ^{13}C spins has been demonstrated^{14–20}. As these nuclear spins can be well isolated from their environments, coherence times of more than one second have been demonstrated²¹, making them interesting candidates for quantum network memories.

A major challenge for realizing quantum memories based on nuclear spins is to overcome the dephasing that is introduced while using the electron spin as an optical interface to generate spin-photon entanglement. Consider the general case of an entanglement protocol that is inherently probabilistic due to lossy optical channels. The protocol therefore must be repeated many times in order to establish an entanglement link between adjacent network nodes. Whenever the entanglement attempt fails, the electron spin is projected in a random state. A fast and practical solution is to re-initialize the spin by optical pumping after each repetition. Because the exact time at which the electron spin is reset is uncertain (optical pumping is a stochastic process) and the electron-nuclear interaction is always present, the electron reset can cause nuclear spin dephasing (Fig. 6.1). A promising route to overcome this dephasing of the quantum memory is to use relatively distant ^{13}C spins with weak hyperfine couplings, which are less sensitive to fluctuations of the electron spin.

In this manuscript we explore the storage of quantum states in ^{13}C spins during the repeated generation of NV spin-photon entanglement. We first demonstrate a method to directly measure the frequency difference df for the electron-state-dependent nuclear spin precessions, which governs the nuclear dephasing (Fig. 6.1)²². We then analyze the spin-photon entanglement protocol, develop a model to describe the dephasing of nuclear spins, and calculate the fidelity of nuclear spin quantum memories with realistic coupling parameters under many repetitions of the entanglement protocol.

6.2 Control and Characterization of nuclear spins in diamond

We start by discussing the experimental methods to control the NV center and nearby ^{13}C nuclear spins. We then introduce a Ramsey-spectroscopy method to directly determine the frequency df and characterize four candidate ^{13}C spins near a single NV-center. These experimental results highlight the universal presence of controllable nuclear spin memories and provide a realistic set of input parameters for the theoretical calculations.

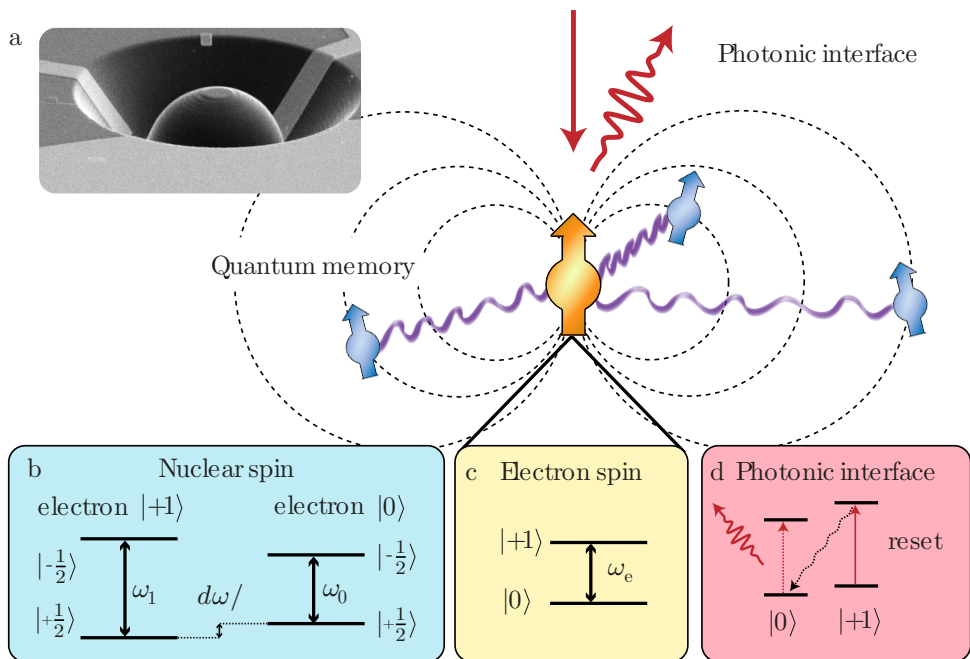


Figure 6.1 | The NV-center as a network node including a quantum memory A single electron spin (orange) is coupled (purple curly arrows) to individual carbon spins (blue) via the magnetic dipole field (black dashed lines) associated with the electron spin. A laser beam (red straight arrow) is used to prepare and read-out the spin state by collecting the fluorescence (red curly arrow). (a) Scanning electron microscope image of the sample. A solid-immersion lens is fabricated with a focused ion beam in single-crystalline diamond for high collection efficiency. An on-chip gold stripline (bottom) enables microwave-control. (b) Level scheme for the quantum memory (^{13}C -spin, $I = 1/2$). The hyperfine coupling introduces energy level splittings (ω_0 and ω_1) that depend on the state of the electron spin, where $\omega_0 = (2\pi) \gamma_C B$ with γ_C the gyromagnetic ratio of the carbon spin and B the magnetic field and ω_1 depends on the hyperfine coupling, which is set by the distance to the electron spin. (c) Relevant ground-state energy levels of the electron spin ($S = 1$). The degeneracy of the $m_s = \pm 1$ states is lifted by applying a magnetic field along the quantization axis of the NV-center. We define the electron spin qubit in the $|0\rangle = m_s = 0, |1\rangle = m_s = +1$ manifold. Here $B_z = (303 \pm 1)$ G leading to an energy level splitting $\omega_e \sim (2\pi) 3.73$ GHz. (d) Diagram of the electron spin including the relevant ground-, and excited-state levels. At low temperature the zero phonon line (~ 637 nm) exhibits spin-preserving optical transitions that can be addressed selectively. In the experiment, two lasers with different frequency are used to address the E' transition for electron spin initialization (dashed red) and the E_y transition for readout (fidelity = 0.93(5)) and generating spin-photon entanglement (solid red).

At the heart of the experiment is a single Nitrogen-Vacancy (NV) center in high purity (Type IIa) single-crystal diamond grown by chemical-vapor-deposition. The diamond is held at a temperature of $T = 4.2$ K in a Helium bath cryostat. The diamond has a natural abundance (1.1%) of ^{13}C spins ($I = 1/2$) in an otherwise ^{12}C spin-free lattice. The NV electronic spin is polarized and measured optically by spin-selective resonant excitation^{12,23,24}. To obtain high single-shot readout fidelities, a solid-immersion lens was fabricated on top of the NV center and a single-layer aluminum-oxide anti-reflective coating was deposited¹³ (Fig 6.1a). The electronic spin is controlled by microwaves applied through an on-chip line (Rabi frequency: 3.3 MHz).

We detect and control multiple ^{13}C nuclear spins in the spin bath surrounding the NV center using recently developed methods that coherently exploit the electron-nuclear interaction by periodically switching the electron state at well-defined times^{20,25–27}. We apply sequences of the form $(\tau - \pi - 2\tau - \pi - \tau)^{M/2}$, where π denotes a microwave pulse that rotates the electron by 180 degrees, 2τ is the interpulse delay and M the total number of π -pulses. For τ precisely resonant with the electron-nuclear dynamics, this sequence imprints a phase on the electron spin conditional on the nuclear spin state.

Because the hyperfine interaction is determined by the specific position of each nuclear spin relative to the NV center, the resonance condition for τ is different for each nuclear spin. We can thus characterize the nuclear spin environment²⁰ by preparing the electron in a superposition state and measuring the phase that is acquired when sweeping τ . Here we select four individual ^{13}C spins to study in more detail, and design controlled gates following Taminiua et al.²⁷.

The nuclear spin dynamics are characterized by the nuclear spin precession frequencies ω_0 and ω_1 corresponding to the electron spin being in $m_s = 0$ and $m_s = 1$, respectively (see also Methods). To directly determine the frequencies ω_0 , ω_1 and $df = (\omega_1 - \omega_0)/2\pi$ for each of the four nuclear spins we perform the experimental sequence²² shown in Fig. 6.2a. The electron is prepared in state $\rho_{0,e} = |0\rangle\langle 0|$, whereas the nuclear spin state is un-polarized (mixed state $\rho_{m,C} = (|0\rangle\langle 0| + |1\rangle\langle 1|)/2$). The first set of gates correlates the electron state with the X-projection of the nuclear spin state, so that the state is $\rho_{0,e} \otimes \rho_{x,C} + \rho_{1,e} \otimes \rho_{-x,C}$, with $\rho_{\pm x,C} = |\pm X\rangle\langle \pm X|$ and $|\pm X\rangle = (|0\rangle_C \pm |1\rangle_C)/\sqrt{2}$. The controlled nuclear spin rotations are realized by the pulse sequences described above, with τ resonant for that specific spin. Second, the nuclear spin evolves freely, either with ω_0 or with ω_1 , depending on the electron state. Finally the phase accumulation of the nuclear spin is measured by correlating it to the electron spin before reading out the electron spin.

The beating observed in the signal directly yields the frequency difference df and therefore the additional phase picked up due to the time the electron spent in $m_s = +1$. For the four spins we find $df = (29.6 \pm 0.6)$, (-32.2 ± 0.3) , (38.6 ± 0.2) and (45.6 ± 0.6) kHz respectively. These values show that several nuclear spins with coupling strengths between approximately 20-50 kHz are readily available in diamond samples with a natural abundance of ^{13}C .

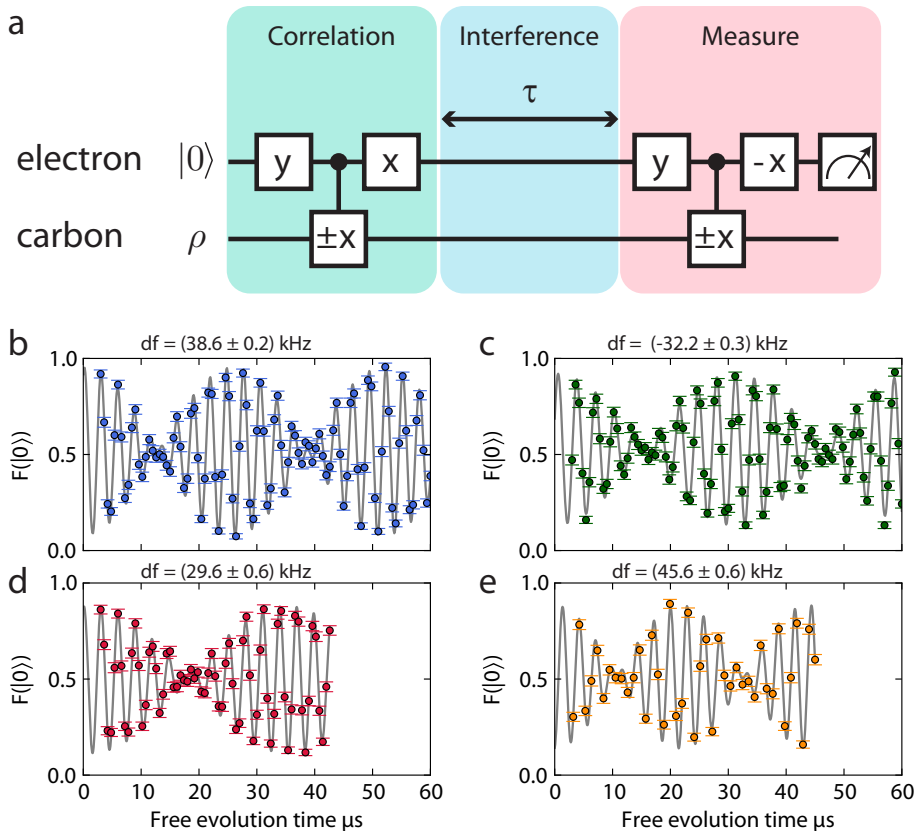


Figure 6.2 | Characterization of single ^{13}C spins. (a) Circuit diagram to determine ω_0 and ω_1 of individual ^{13}C spins via the electron spin. The conditional gates on the carbon spin are implemented using resonant dynamical decoupling techniques as explained in the main text. Because the evolution of the carbon spin is correlated with an eigenstate of the electron spin during the interference, a coherent signal can be observed even for $\tau \gg T_{2,\text{electron}}^* = (4.18 \pm 0.01) \mu\text{s}$ (b)-(e) The resulting interference signal measured for four individual ^{13}C spins near a single NV-center. Grey lines are fits to the data with function $F = \frac{A}{2} \cos(\omega_0 \tau + \phi_0) + \frac{B}{2} \cos(\omega_1 \tau + \phi_1)$. We find $\omega_0 / 2\pi = (326.0 \pm 0.2)$, (325.9 ± 0.2) , (325.1 ± 0.5) , (325.9 ± 0.4) kHz (b-e), consistent with the gyromagnetic ratio of a ^{13}C spin in a field of (303 ± 1) G. For the second frequency component we find $\omega_1 / 2\pi = (364.6 \pm 0.1)$, (293.7 ± 0.2) , (354.7 ± 0.5) , (371.5 ± 0.4) kHz. The data is taken with 500 repetitions per data point and the error bars correspond to one standard deviation.

6.3 Modeling the dephasing of a carbon spin during entanglement generation

We analyze the performance of ^{13}C spins as quantum memory in the context of the heralded entanglement protocol proposed by Barrett and Kok²⁸, which was implemented by Bernien et al.⁶. The protocol is based on the creation of spin-photon entanglement at both nodes, followed by two-photon interference and measurement of these photons. The protocol is probabilistic since it is susceptible to photon loss. Importantly, successful generation of entanglement is heralded by the detection of the two photons and thus the sequence can be repeated until successful.

Spin-photon entanglement is created using the following sequence (Fig. 6.3a). The electron spin is prepared in state $|0\rangle_e$ by optical pumping (Fig. 6.1d). Using microwaves the electron spin is then brought in a coherent superposition. Next, the NV center is optically excited with a short laser pulse that is only resonant if the spin is in state $|0\rangle_e$. Spontaneous emission generates a photon that is entangled with the state of the spin: $|\Psi\rangle = (|0\rangle_e |1\rangle_p + |1\rangle_e |0\rangle_p)/\sqrt{2}$ where $|1\rangle_p$ ($|0\rangle_p$) denotes the presence (absence) of a photon. The goal is that the nuclear spin memory reliably stores quantum states during many repetitions of this sequence.

The performance of a quantum memory can be characterized by its ability to store an unknown quantum state $|\psi\rangle = \alpha|0\rangle_C + \beta e^{i\phi}|1\rangle_C$. During the spin-photon entanglement sequences the phase ϕ of the nuclear spin state is affected in two ways. First, when the emitted photon is lost (heralding fails), the electron spin state is randomly projected into either $|0\rangle_e$ or $|1\rangle_e$ resulting in nuclear spin evolutions with ω_0 or ω_1 , respectively. Second, before the next repetition, the electron spin is reset by optical pumping, a stochastic process that introduces a distribution of spin flip times. These two effects are now analyzed separately.

After a single round of optical excitation that generates spin-photon entanglement, the electron spin is projected into an unknown eigenstate if the photon is lost. The carbon spin acquires a phase $d\omega t$ if the electron is projected in $|1\rangle_e$, where $d\omega = 2\pi df$ and t the time at which the reset is applied. When this process is repeated N times, the number of times k that the electron is projected in $|1\rangle_e$ is given by a binomial distribution and the final state fidelity F of the carbon spin state is given by:

$$F = \frac{1}{2} + \frac{1}{2^{N+1}} \sum_{k=0}^N \binom{N}{k} \cos[kd\omega t] \quad (6.1)$$

where the electron spin reset is taken to be instantaneous and we only consider the initial memory state is $|\psi\rangle = (|0\rangle_C + |1\rangle_C)/\sqrt{2}$, which is most sensitive to dephasing. Fig. 6.3b shows the calculated fidelity as a function of the time t , for two carbon spins that were identified in Fig. 6.2. For each carbon spin there is a unique condition at $t = 2\pi/d\omega$, for which the phase is independent on the electron state resulting in $F = 1$. Note that in the full

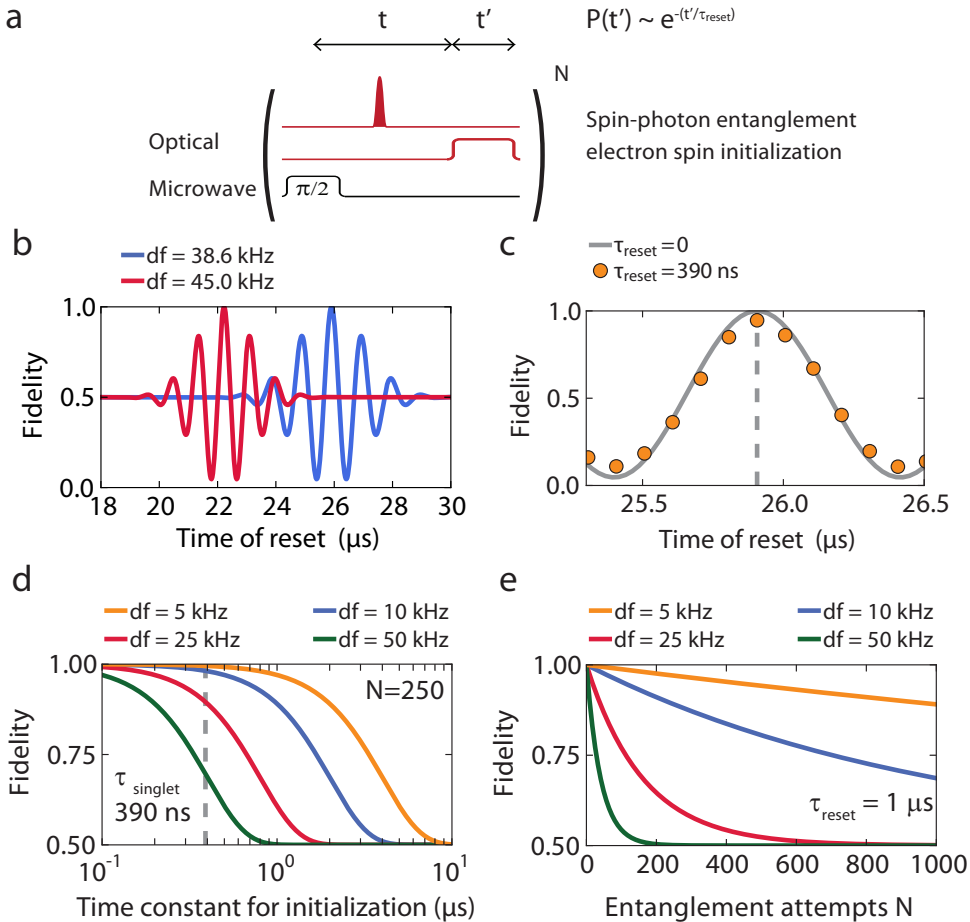


Figure 6.3 | Simulations of the dephasing of a ^{13}C spin quantum memory while generating entanglement. (a) Diagram for the protocol to create spin-photon entanglement. (b) Simulations of the fidelity for different ^{13}C spins after $N = 50$ repetitions of the protocol, assuming that the reset is instantaneous ($t' = 0$, formula 6.1 of main text). The initial state of a carbon spin can be perfectly preserved by choosing the time between the $\pi/2$ -pulse and the reset to $t = 2\pi / d\omega$. (c) The effect of the spin pumping process on the fidelity of the memory after $N = 50$ repetitions. Orange dots are a Monte-Carlo simulation where for every electron spin reset, a time t' is drawn from an exponential probability distribution with $\tau_{\text{reset}} = 390 \text{ ns}$. Grey line is a comparison with an ideal reset. $d\omega = (2\pi) 38.6 \text{ kHz}$. (d) Dependence of the memory fidelity on the characteristic reset time τ_{reset} using formula 6.2. (e) Dephasing of the memory as a function of entanglement attempts for different coupling strengths, fixing $\tau_{\text{reset}} = 1 \mu\text{s}$.

entanglement protocol^{6,28} an electron π -pulse is applied between rounds of excitation, so that this phase difference can be cancelled for all t .

In reality the reset of the electron spin by spin pumping is a stochastic process involving multiple transitions to the optically excited state as well as mixing between multiple excited states. Here we model the dynamics of this process as an exponential distribution $e^{-\frac{t'}{\tau_{reset}}}$ with a characteristic time τ_{reset} . In Fig. 6.3c we compare the results of a monte-carlo simulation that includes the probabilistic reset time t' for $\tau_{reset} = 390$ ns with the curve of equation 6.1. As expected the same behavior is observed, but the maximum fidelity is reduced since the stochastic reset leads to dephasing of the carbon spin.

To analyze the effect of the electron spin reset on the nuclear spin in detail we now assume that $t = 2\pi d\omega$ which allows us to derive an analytical expression for the fidelity of the carbon spin (see methods for the derivation of this result):

$$F = \frac{1}{2} + \frac{1}{2^{N+1}} \left(1 + e^{-\frac{1}{2} \tau_{reset}^2 d\omega^2} \right)^N. \quad (6.2)$$

In Fig. 6.3d we plot the resulting memory fidelity after 250 entanglement repetitions versus the reset constant τ_{reset} , for different values of df . Although for an instantaneous reset ($\tau_{reset} \rightarrow 0$) the state can be perfectly preserved, a finite uncertainty in the reset time constant reduces the fidelity, with the effect being stronger for higher coupling strengths df . A natural lower limit to the reset time τ_{reset} is the slowest decay rate involved in the spin pumping process. For the NV center this is expected to be the singlet lifetime $\tau_{singlet} \approx 390$ ns²⁹. For this value, Fig. 6.3d predicts that for coupling strengths of $df < 10$ kHz the state can be preserved with a fidelity of > 98 % even after 250 entanglement attempts.

The reset constants currently reported in the literature are approximately 1 μ s⁶. In Fig. 6.3e we plot the fidelity as a function of number of entanglement attempts for $\tau_{reset} = 1 \mu$ s. These calculations predict that 25 repetitions of the entanglement protocol will yield a fidelity of 90.3 % for the lowest coupling strength found in Fig. 6.2, which would already provide significant speed advantages in establishing entanglement links⁸. For coupling strengths $df < 10$ kHz, hundreds of repetitions become feasible. Such lower coupling strengths are available in isotopically purified diamonds²¹.

We emphasize that the model presented here does not include the detailed excited state dynamics of the spin pumping process. We expect that averaging over rapid spin flips and time spent in states with zero spin projection during these dynamics will further reduce actual dephasing. We therefore expect that our analysis sets a lower bound for the number of possible repetitions.

We have modelled the dephasing of nuclear spins quantum memories coupled to an NV electron spin that is repeatedly used to establish spin-photon entanglement. We find that nuclear spins with weak hyperfine couplings (20-50 kHz) are readily available in natural abundance diamonds. Our analysis shows that these spins can be used to store quantum

states during 25 entanglement attempts with a fidelity of 90.3 %, while nuclear spins in isotopically purified samples with coupling strengths below 10 kHz can even enable hundreds of repetitions. These results demonstrate that nuclear spins with weak hyperfine coupling strengths are promising quantum memories for quantum networks providing a route towards entanglement distillation and quantum repeaters.

6.4 Methods

We take the limit of $\gamma_C B \gg A_{\perp}$ (with A_{\perp} the hyperfine component perpendicular to the static magnetic field) such that the eigenstates of the ^{13}C -spin are independent of the electron and the only net effect of the electron-carbon coupling is that the carbon acquires a phase depending on the state of the electron. Choosing the rotating frame of the carbon resonant with the energy splitting for the electron in $|0\rangle_e$, the carbon state will acquire a phase $e^{id\omega t}$ for the electron in $|1\rangle_e$ (with $d\omega = 2\pi df$) and does not evolve otherwise.

We derive an expression for the maximally achievable memory fidelity. The scheme of Fig 3a is repeated N times. Phase errors occur if the electron spin has to be reinitialized by pumping it to another spin state. During every execution of the protocol, the electron spin is projected into $|0\rangle_e$ or $|1\rangle_e$ with equal probability. The probability for k repumping events is then given by a binomial distribution

$$P_{ek} = \frac{1}{2^N} \binom{N}{k} \quad (6.3)$$

Every time the electron is reset from $|1\rangle_e$ into $|0\rangle_e$ the memory spin will pick up a random phase $\delta\theta = d\omega(t' - \tau_{reset})$ which is given by the difference between energy levels of the carbon spin conditional on the electron spin $d\omega$ and the deviation $(t' - \tau_{reset})$ from the mean repumping time. The overall acquired phase for k repumping events is then the sum of the individual random phases. The fidelity with the initial memory state after N repetitions is thus given by

$$F_k = \frac{1}{2} \left(1 + \cos \left[\sum_{k=0}^N \delta\theta_k \right] \right) \quad (6.4)$$

Under the assumption that the distributions for all repumping events are independent the problem can be seen as a random walk in accumulated repumping time. Each step of this random walk is then exponentially distributed around the mean repumping time τ_{reset} . The probability distribution of the summed repumping time is given by³⁰

$$P(t') = \frac{t'^{k-1}}{\tau_{reset}^k (k-1)!} e^{-t'/\tau_{reset}} \approx \frac{1}{\sqrt{2\pi\sigma}} e^{-\frac{(t'-\mu)^2}{2\sigma^2}} \quad (6.5)$$

where we use the central limit theorem to approximate this distribution by a normal distribution with width $\sigma = \tau_{reset}\sqrt{k}$ and mean $\mu = \tau_{reset}k$, as we are interested in solutions for a large number of repumping events. The expected fidelity after N experimental runs is calculated by summing over the probability distributions for the electronic state and the corresponding accumulated repumping time

$$\begin{aligned}
 F_N &= \sum_{k=0}^N P_{ek} \int F_k P(t') dt' \\
 &= \frac{1}{2} + \frac{1}{2} \sum_{k=0}^N P_{ek} e^{-\frac{1}{2}k\tau_{reset}^2 d\omega^2} \\
 &= \frac{1}{2} + \frac{1}{2^{N+1}} \left(1 + e^{-\frac{1}{2}\tau_{reset}^2 d\omega^2} \right)^N.
 \end{aligned} \tag{6.6}$$

6.5 Bibliography

- [1] W. B. Gao, A. Imamoglu, H. Bernien and R. Hanson. Coherent manipulation, measurement and entanglement of individual solid-state spins using optical fields. *Nature Photonics* **9**, 363 (2015).
- [2] H. J. Kimble. The quantum internet. *Nature* **453**, 1023 (2008).
- [3] D. L. Moehring *et al.* Entanglement of single-atom quantum bits at a distance. *Nature* **449**, 68 (2007).
- [4] S. Ritter *et al.* An elementary quantum network of single atoms in optical cavities. *Nature* **484**, 195 (2012).
- [5] J. Hofmann *et al.* Heralded entanglement between widely separated atoms. *Science* **337**, 72 (2012).
- [6] H. Bernien *et al.* Heralded entanglement between solid-state qubits separated by three metres. *Nature* **497**, 86 (2013).
- [7] C. H. Bennett *et al.* Purification of noisy entanglement and faithful teleportation via noisy channels. *Physical Review Letters* **76**, 722 (1996).
- [8] E. T. Campbell and S. C. Benjamin. Measurement-based entanglement under conditions of extreme photon loss. *Physical Review Letters* **101**, 130502 (2008).
- [9] H.-J. Briegel, W. Dür, J. I. Cirac and P. Zoller. Quantum repeaters: The role of imperfect local operations in quantum communication. *Physical Review Letters* **81**, 5932 (1998).
- [10] L. Childress, J. M. Taylor, A. S. Sørensen and M. D. Lukin. Fault-tolerant quantum communication based on solid-state photon emitters. *Physical Review Letters* **96**, 070504 (2006).
- [11] L. Childress and R. Hanson. Diamond NV centers for quantum computing and quantum networks. *MRS Bulletin* **38**, 134 (2013).
- [12] E. Togan *et al.* Quantum entanglement between an optical photon and a solid-state spin qubit. *Nature* **466**, 730 (2010).
- [13] W. Pfaff *et al.* Unconditional quantum teleportation between distant solid-state quantum bits. *Science* **345**, 532 (2014).
- [14] F. Jelezko *et al.* Observation of coherent oscillation of a single nuclear spin and realization of a two-qubit conditional quantum gate. *Physical Review Letters* **93**, 130501 (2004).
- [15] M. V. G. Dutt *et al.* Quantum register based on individual electronic and nuclear spin qubits in diamond. *Science* **316**, 1312 (2007).

- [16] P. Neumann *et al.* Multipartite entanglement among single spins in diamond. *Science* **320**, 1326 (2008).
- [17] B. Smeltzer, J. McIntyre and L. Childress. Robust control of individual nuclear spins in diamond. *Physical Review A* **80**, 050302 (2009).
- [18] G. D. Fuchs, G. Burkard, P. V. Klimov and D. D. Awschalom. A quantum memory intrinsic to single nitrogen-vacancy centres in diamond. *Nature Physics* **7**, 789 (2011).
- [19] T. van der Sar *et al.* Decoherence-protected quantum gates for a hybrid solid-state spin register. *Nature* **484**, 82 (2012).
- [20] T. H. Taminiau *et al.* Detection and control of individual nuclear spins using a weakly coupled electron spin. *Physical Review Letters* **109**, 137602 (2012).
- [21] P. C. Maurer *et al.* Room-temperature quantum bit memory exceeding one second. *Science* **336**, 1283 (2012).
- [22] A. Laraoui *et al.* High-resolution correlation spectroscopy of ¹³C spins near a nitrogen-vacancy centre in diamond. *Nat Commun* **4**, 1651 (2013).
- [23] P. Tamarat *et al.* Spin-flip and spin-conserving optical transitions of the nitrogen-vacancy centre in diamond. *New Journal of Physics* **10**, 045004 (2008).
- [24] L. Robledo *et al.* High-fidelity projective read-out of a solid-state spin quantum register. *Nature* **477**, 574 (2011).
- [25] S. Kolkowitz, Q. P. Unterreithmeier, S. D. Bennett and M. D. Lukin. Sensing distant nuclear spins with a single electron spin. *Physical Review Letters* **109**, 137601 (2012).
- [26] N. Zhao *et al.* Sensing single remote nuclear spins. *Nature Nanotechnology* **7**, 657 (2012).
- [27] T. H. Taminiau, J. Cramer, T. v. d. Sar, V. V. Dobrovitski and R. Hanson. Universal control and error correction in multi-qubit spin registers in diamond. *Nature Nanotechnology* **9**, 171 (2014).
- [28] S. D. Barrett and P. Kok. Efficient high-fidelity quantum computation using matter qubits and linear optics. *Physical Review A* **71**, 060310 (2005).
- [29] M. W. Doherty *et al.* The nitrogen-vacancy colour centre in diamond. *Physics Reports* **528**, 1 (2013).
- [30] M. Akkouchi. On the convolution of exponential distributions. *Journal of the Chungcheong mathematical society* **21**, 4 (2008).

CHAPTER 7

STORING A QUANTUM STATE DURING OPTICAL EXCITATION OF A QUANTUM NETWORK NODE

M.S. Blok, K. van Bemmelen, N. Kalb, A. Reiserer, T.H. Taminiau and R. Hanson

The ability to locally store a quantum state in a quantum network node while establishing entanglement with a distant node is a crucial prerequisite for implementing entanglement distillation, purification and quantum repeater protocols^{???}. For quantum network nodes based on NV centers in diamond, nearby ¹³C-spins are a prime candidate for such a quantum memory. The challenge is that these nuclear spins have a constant coupling to the optically active electron spin, resulting in possible dephasing of the stored state when the electron is reset multiple times as required for generating remote entanglement. In chapter 6 we discussed an analytical model to describe this process and found that nodes with low electron-nuclear coupling strength and fast electron reset are expected to provide the best performance. Here we present preliminary experimental results to test our model in an isotopically purified sample where ¹³C-spins with coupling strengths of < 1 kHz can be located and controlled. We find that multiple resets of the electron spin indeed induce dephasing of the nuclear-spin quantum memory and that this process can be suppressed by reducing the electron reset time. While the data qualitatively agrees with our model, the observed decoherence rate is faster than predicted indicating that we are limited by an additional dephasing process. Nonetheless our results show that a ¹³C-spin allows for the storage of a quantum state during 200 repetitions with very little loss of fidelity (99% fidelity with initial state).

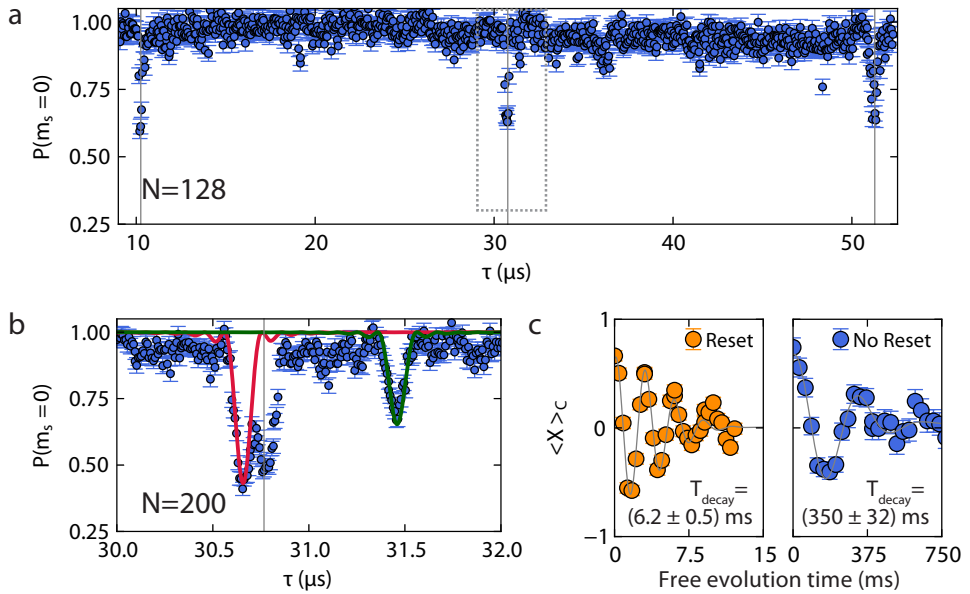


Figure 7.1 | (a)Dynamical Decoupling spectroscopy of the ^{13}C -spin bath. Grey lines are the expected collapses of the signal due to interaction with the ^{13}C -spin bath. (b) Two ^{13}C -Spins can be identified, red (green) line is a simulation of the resulting signal for the interaction with a single spin with hyperfine constants of $A_{\text{par}} = \dots$ and A_{perp} ($A_{\text{par}} = \dots$ and A_{perp}) (c) Free induction decay of a single carbon spin with and without repetitive reset

7.1 Introduction

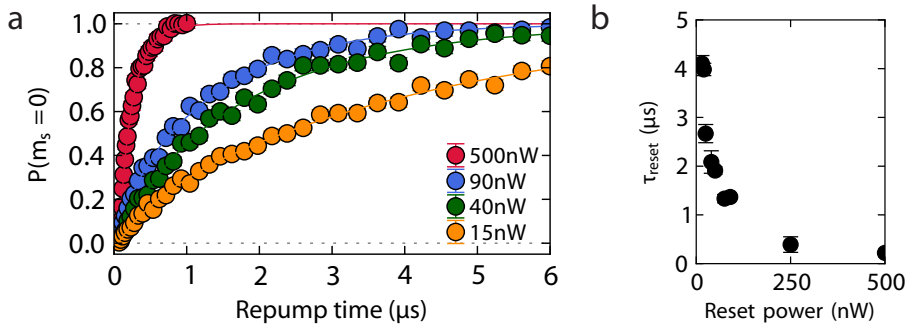


Figure 7.2 | Reset of the electron spin (a) Measurement of the timescale of the reset process. Plotted is the probability of preparing $m_s = 0$ after preparing $m_s = \pm 1$ as a function of repump time and power (b) Fitted time constant of the reset process as a function of reset power.

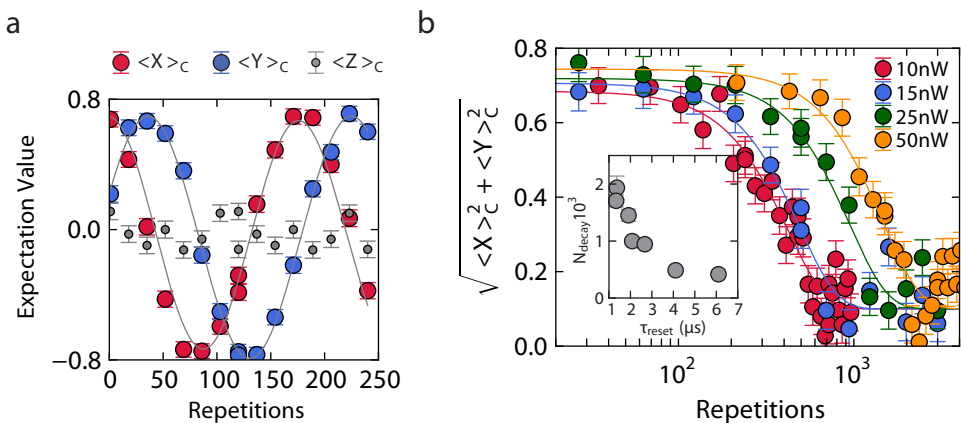


Figure 7.3 | (a) Result of tomography (measuring X,Y and Z) for varying number of resets. (b)

7.2 Bibliography

